

Multiscale Modelling of Single Crystal Superalloys for Gas Turbine Blades

PROEFSCHRIFT

ter verkrijging van de graad van doctor aan de
Technische Universiteit Eindhoven, op gezag van de
Rector Magnificus, prof.dr.ir. C.J. van Duijn, voor een
commissie aangewezen door het College voor
Promoties in het openbaar te verdedigen
op donderdag 7 mei 2009 om 16.00 uur

door

Tiedo Tinga

geboren te Lemmer

Dit proefschrift is goedgekeurd door de promotor:

prof.dr.ir. M.G.D. Geers

Copromotor:

dr.ir. W.A.M. Brekelmans

Multiscale Modelling of Single Crystal Superalloys for Gas Turbine Blades / by Tiedo
Tinga. – Eindhoven: Technische Universiteit Eindhoven, 2009

A catalogue record is available from the Eindhoven University of Technology Library
ISBN 978-90-386-1721-3

Copyright ©2009 by T. Tinga. All rights reserved.

Omslag ontwerp: P.J. de Vries, Bureau Multimedia NLDA

Druk: Giethoorn ten Brink B.V.

Contents

Summary	iii
1. Introduction	1
1.1 Background and motivation	1
1.2 Objective and outline	4
2. Multiscale framework	5
2.1 Introduction	5
2.2 Multiscale model description	9
2.3 Constitutive behaviour	16
2.4 Internal stresses	22
2.5 Application	28
2.6 Conclusions	40
3. Cube slip and precipitate phase constitutive model	41
3.1 Introduction	41
3.2 Multiscale framework	46
3.3 Cube slip	49
3.4 Precipitate phase constitutive model	55
3.5 Model parameter determination	65
3.6 Results	70
3.7 Conclusions	76
4. Damage model	79
4.1 Introduction	79
4.2 Micro level damage mechanisms	85
4.3 Proposed damage model	89
4.4 Creep – fatigue interaction	91
4.5 Implementation	94
4.6 Results	97
4.7 Conclusion	99

5.	Microstructure degradation	101
5.1	Introduction	101
5.2	Kinetics of microstructure degradation	108
5.3	Effect on the deformation	117
5.4	Effect on the damage accumulation	120
5.5	Application	121
5.6	Summary and conclusions	128
6.	Application to gas turbine parts	131
6.1	Introduction	131
6.2	Finite Element model	131
6.3	Rafting simulation	133
6.4	Effect of degradation on creep deformation	136
6.5	Effect of degradation on the damage accumulation	139
6.6	Discussion and conclusions	141
7.	Conclusions & recommendations	145
A.	Finite Element implementation	149
A.1	Introduction	149
A.2	Flow diagram	149
A.3	Multiscale model implementation in MSC.Marc	151
A.4	Solution procedures for non-linear systems	153
B.	Overview of model parameters	157
B.1	Introduction	157
B.2	Parameter values	158
	Bibliography	161
	Samenvatting	169
	Dankwoord	171
	Curriculum Vitae	173

Summary

Multiscale Modelling of Single Crystal Superalloys for Gas Turbine Blades

Gas turbines are extensively used for power generation and for the propulsion of aircraft and vessels. Their most severely loaded parts, the turbine rotor blades, are manufactured from single crystal nickel-base superalloys. The superior high temperature behaviour of these materials is attributed to the two-phase composite microstructure consisting of a γ -matrix (Ni) containing a large volume fraction of γ' -particles (Ni_3Al). During service, the initially cuboidal precipitates evolve to elongated plates through a diffusion-based process called rafting.

In this work, a micro-mechanical constitutive framework is developed that specifically accounts for the microstructural morphology and its evolution. In the proposed multiscale approach, the macroscopic length scale characterizes the engineering level on which a finite element (FE) calculation is typically applied. The mesoscopic length scale represents the level of the microstructure attributed to a macroscopic material point. At this length scale, the material is considered as a compound of two different phases, which compose a dedicatedly designed unit cell. The microscopic length scale reflects the crystallographic level of the individual material phases. The constitutive behaviour of these phases is defined at this level.

The proposed unit cell contains special interface regions, in which plastic strain gradients are assumed to be concentrated. In these interface regions, strain gradient induced back stresses develop as well as stresses originating from the lattice misfit between the two phases. The limited size of the unit cell and the micromechanical simplifications make the framework particularly efficient in a multiscale approach. The unit cell response is determined numerically at a material point level within a macroscopic FE code, which is computationally much more efficient than a detailed FE based unit cell discretization.

The matrix phase constitutive behaviour is simulated by using a non-local strain gradient crystal plasticity model. In this model, non-uniform distributions of geometrically necessary dislocations (GNDs), induced by strain gradients in the interface regions, affect the hardening behaviour. Further, specifically for the two-phase material at interest, the hardening law contains a threshold term related to the Orowan stress. For the precipitate phase, the mechanisms of precipitate shearing and recovery

climb are incorporated in the model. Additionally, the typical anomalous yield behaviour of Ni₃Al-intermetallics and other non-Schmid effects are implemented and their impact on the superalloy mechanical response is demonstrated.

Next, a damage model is proposed that integrates time-dependent and cyclic damage into a generally applicable time-incremental damage rule. A criterion based on the Orowan stress is introduced to detect slip reversal on the microscopic level and the cyclic damage accumulation is quantified using the dislocation loop immobilization mechanism. Further, the interaction between cyclic and time-dependent damage accumulation is incorporated in the model. Simulations for a wide range of load conditions show adequate agreement with experimental results.

The rafting and coarsening processes are modelled by defining evolution equations for several of the microstructural dimensions. These equations are consistent with a reduction of the internal energy, which is often considered as the driving force for the degradation process. The mechanical response of the degraded material is simulated and adequate agreement is found with experimentally observed trends.

Finally, the multiscale capability is demonstrated by applying the model in a gas turbine blade finite element analysis. This shows that changes in microstructure considerably affect the mechanical response of the gas turbine components.

Chapter 1

Introduction

1.1 Background and motivation

Gas turbines are extensively used for power generation and for the propulsion of aircraft and vessels, see Figure 1-1. The efficiency of gas turbines is directly related to the firing temperature of the machine. For that reason the gas temperature in the turbine section has steadily increased from 800 °C in the 1950s to about 1600 °C in modern designs.



Figure 1-1 Typical applications of gas turbines for platform propulsion: F-16 fighter aircraft and multipurpose navy frigate.

These high temperatures cause a severe thermal load on the metal components inside the gas turbine. The rotating parts, with typical speeds of 12,000 revolutions per minute, additionally face a high mechanical load due to the centrifugal force acting on the parts.

The turbine blades, which are rotating parts located directly behind the combustion chamber, see Figure 1-2, are the most severely loaded components in a gas turbine. To ensure their structural integrity, the metal temperature of the blades must be limited and the mechanical quality of the applied materials must be sufficiently high. A reduction of the metal temperature is achieved by the application of efficient blade cooling techniques (e.g. internal cooling or film cooling), while the required

mechanical properties are obtained by selecting the proper alloy, possibly combined with the application of a suitable coating.

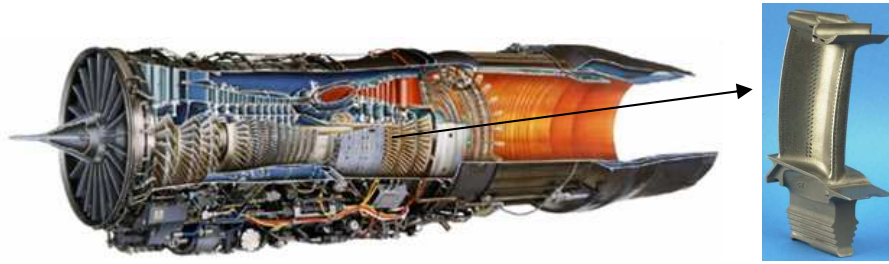


Figure 1-2 Illustration of a gas turbine (aero-engine) showing the location of the turbine blades and a detailed view of a first stage high pressure turbine blade.

Since a number of decades, single crystal nickel-base superalloys are widely used as gas turbine blade materials because of their superior resistance against high temperature inelastic deformation. Their remarkable high temperature behaviour is attributed to the two-phase composite microstructure consisting of a Ni matrix (γ -phase) containing a large volume fraction of Ni_3Al particles (γ' -phase), see Figure 1-3. Cube-like Ni_3Al precipitates are more or less regularly distributed in a Ni-matrix. The typical precipitate size is 500 nm and the matrix channel width is typically 60 nm. Since these very narrow matrix channels experience the majority of the plastic deformation, considerable plastic strain gradients develop in the material.

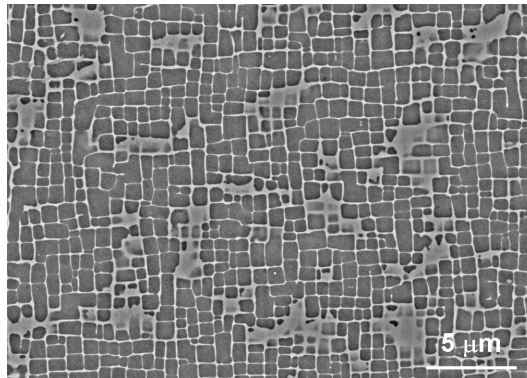


Figure 1-3 Micrograph of a superalloy microstructure showing cube-like γ' -precipitates in a γ -matrix [1].

As gas turbines are applied as jet engines in aeroplanes and for power generation, structural integrity of their parts is critically important, both for safety and economical

reasons. Therefore, a vast amount of research has been performed on the modelling of the mechanical behaviour of superalloys. Initially the material was treated as a homogeneous single phase material [2-12]. In all these approaches conventional crystal plasticity theories were used to describe the material response, which means that constitutive laws were defined on the slip system level. Since these solution methods address the macroscopic level, they can easily be used as a constitutive description in a finite element (FE) analysis, which is nowadays the common method used for component stress analysis and life time assessment.

However, during high temperature service, the microstructure gradually degrades by the so-called rafting process. In the presence of a stress, e.g. caused by the centrifugal load in a gas turbine blade, a severe directional coarsening of the initially cuboidal γ' -particles into a plate-like structure occurs, see Figure 1-4.

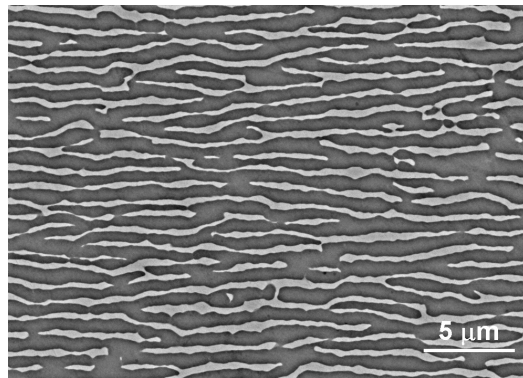


Figure 1-4 Micrograph of a degraded microstructure showing the elongated rafts [1].

To be able to quantify strain gradients in the material and to assess the effect of microstructure degradation on the macroscopic response, the two-phase nature of superalloys has to be modelled explicitly. In the resulting microstructural models the shape, dimensions and properties of both phases are considered as model parameters. However, the length scale of the microstructure, which is in the order of micrometers, is much smaller than the engineering length scale. Modelling a macroscopic component completely, i.e. taking into account all microstructural details is therefore not feasible in the engineering practice.

One way to bridge this gap in length scales is to use a multiscale approach in which an appropriate homogenization method is applied to connect the microscopic to

the macroscopic level. A large number of multiscale frameworks has been developed in the past decades, applied to different materials [13-23].

Another way to overcome the length scale problem is to use microstructural models that predict the material response in a closed-form set of equations at the level of a material point [24-30]. The microstructural results are then used to develop constitutive descriptions that fit in traditional methods at the macroscopic level. Clearly, the analyses on the microscopic and the macroscopic level are completely separated in this case.

However, the latter group of uncoupled models and all approaches using FE based unit cell models, are too detailed and hence usually too complex to be used efficiently in a multiscale analysis of structural components. Therefore, in this work a multiscale approach is pursued to develop a new framework particularly suitable to incorporate strain gradient effects, *and* to be computationally efficient, thus enabling application in a multiscale approach (FE analyses on real components).

1.2 Objective and outline

The objective of the present work is to develop a constitutive model for nickel-base superalloys enabling the simulation of the material deformation and damage behaviour in a computationally efficient way and for a broad range of load conditions. During the simulations, the evolution of the microstructure and its effect on the mechanical behaviour should be taken into account.

In chapter 2, the basic multiscale framework with an elastically deforming precipitate phase is presented. In chapter 3 the framework is extended with two aspects: precipitate plastic deformation and cube slip. Chapter 4 presents a newly developed time-incremental damage rule. In chapter 5, the degradation of the microstructure is treated. Both the effect of microstructure degradation on the mechanical behaviour and the kinetics of the degradation process are considered. Chapter 6 demonstrates the multiscale capabilities of the framework. The multiscale model is applied in finite element analyses on a real gas turbine component. Finally, chapter 7 provides some concluding remarks and a number of recommendations for further research.

Chapter 2

Multiscale framework¹

Abstract - An efficient multiscale constitutive framework for nickel-base superalloys is proposed that enables the incorporation of strain gradient effects. Special interface regions in the unit cell contain the plastic strain gradients that govern the development of internal stresses. The model is shown to accurately simulate the experimentally observed size effects in the commercial alloy CMSX-4. The limited complexity of the proposed unit cell and the micromechanical simplifications make the framework particularly efficient in a multiscale approach. This is demonstrated by applying the model in a gas turbine blade finite element analysis.

2.1 Introduction

Strain gradient effects are only quite recently recognized as an important factor in mechanical modelling at small length scales. At these length scales, the material strength is observed [31] to be size dependent, with an increase of strength at decreasing dimensions, i.e. smaller is stronger. The existence of a strain gradient dependent back stress and its relevance for crystal plasticity of small components undergoing inhomogeneous plastic flow has been reported in several papers. The work of Gurtin and co-workers [32-35] is here emphasized in particular.

Strain gradient effects are also relevant for single crystal nickel-base superalloys, which are widely used as gas turbine blade materials because of their high resistance against high temperature inelastic deformation. The superior high temperature behaviour is attributed to the two-phase composite microstructure consisting of a γ -matrix containing a large volume fraction of γ' -particles (see Figure 1-3). Cubic Ni_3Al (γ') precipitates are more or less regularly distributed in a Ni-matrix (γ -phase), where both phases have a face-centred cubic (fcc) lattice. The typical precipitate size is 0.5 μm and the matrix channel width is typically 60 nm. Since these very narrow

¹ This chapter is reproduced from: Tinga, T., Brekelmans, W. A. M. and Geers, M. G. D.; *Incorporating strain-gradient effects in a multi-scale constitutive framework for nickel-based superalloys*; Philosophical Magazine, 88 (2008), 3793-3825.

matrix channels bear the majority of the plastic deformation, considerable plastic strain gradients develop in the material.

Therefore, strain gradient effects should be included in superalloy constitutive models, as was done by Busso and co-workers [24,25] and Choi et al. [26]. They used a detailed unit cell FE model of an elastic γ' -precipitate embedded in an elasto-viscoplastic γ -matrix. Busso and co-workers [24,25] adopted a non-local gradient dependent crystal plasticity theory to describe the behaviour of the γ -matrix. The flow resistance and hardening of the matrix were based on the densities of statistically stored and geometrically necessary dislocations. This enabled the prediction of a precipitate size dependence of the flow stress and allowed to capture the effect of morphological changes of the precipitate.

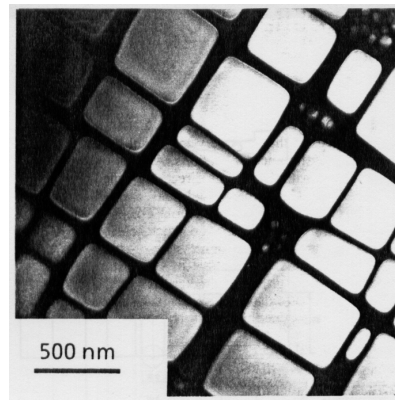


Figure 2-1 Micrograph of a superalloy microstructure showing the cube-like γ' -precipitates in a γ -matrix [36].

Choi et al. [26] extended this work using a more phenomenological crystal plasticity formulation with no direct relation to dislocation densities. However, a strain gradient dependence was incorporated in the model, which also resulted in the prediction of precipitate size effects and an influence of the microstructure morphology.

The ability to perform a reliable life time assessment is crucial for both gas turbine component design and maintenance. Therefore, a vast amount of work has been done on modelling the mechanical behaviour of superalloys. Initially the material was treated as a homogeneous single phase material [2-12]. In all these approaches conventional crystal plasticity theory was used to model the material response, which means that constitutive laws were defined on the slip system level. Since these solution methods address the macroscopic level, they can easily be used as a constitutive

description in a finite element (FE) analysis, which is nowadays the common method used for component stress analysis and life time assessment.

However, to be able to quantify strain gradients in the material and to assess their effect on the macroscopic response, the two-phase nature of superalloys has to be modelled explicitly. In the resulting microstructural models the shape, dimensions and properties of both phases are considered as model parameters. However, the length scale of the microstructure, which is in the order of micrometers, is much smaller than the engineering length scale. Modelling a macroscopic component completely, i.e. taking into account all microstructural details, is therefore not feasible in the engineering practice.

One way to bridge this gap in length scales is to use a multiscale approach in which an appropriate homogenization method is applied to connect the microscopic to the macroscopic level. A large number of multiscale frameworks has been developed in the past decades and applied to different materials. Examples are Eshelby-type homogenization methods [13] for materials with (elastic) inclusions, variational bounding methods [14,15] and asymptotic homogenization methods [16,17]. Some more recent examples applicable to the class of unit cell methods are the first order [18,19] and second order [20] computational homogenization methods and the crystal plasticity work by Evers [21] that considered the effect of multiple differently oriented grains in an FCC metal. Finally, Fedelich [22,23] used a Fourier series homogenization method to model the mechanical behaviour of Ni-base superalloys.

Another way to overcome the length scale problem is to use microstructural models that predict the material response in a closed-form set of equations on the level of the material point [24-30]. The microstructural results are then used to develop constitutive descriptions that fit in traditional methods at the macroscopic level. In this case, the coupling between the microscopic and the macroscopic level relies on rather simple averaging procedures. Svoboda and Lukas [28,30] developed an analytical unit cell model consisting of a γ' -precipitate and three γ -channels. The deformation in the distinct regions was assumed to be uniform and power law creep behaviour was used for the matrix material. The required compatibility at the γ/γ' -interfaces resulted in a relatively high overall stiffness. Kuttner and Wahi [29] used a FE method to model a unit cell representing the γ/γ' -microstructure. A modified Norton's creep law was assumed for both phases and threshold stresses for different deformation mechanisms were included. The latter models [28-30] as well as the model by Fedelich [22,23] adopted the Orowan stress as a threshold stress for plastic deformation. Since the Orowan stress is related to the spacing of the γ' -precipitates, a length scale dependence

was explicitly introduced into the constitutive description. However, apart from the models by Busso and co-workers [24,25] and Choi et al. [26], that were discussed before, none of these models includes strain gradient effects, whereas the FE based unit cell models are detailed but usually too complex to be used efficiently in a multiscale analysis of structural components. Therefore, in this chapter a new framework is proposed that is particularly developed to incorporate strain gradient effects, *and* to be computational efficient, thus enabling application in a multiscale approach (FE analyses on real components).

A new unit cell approach is forwarded, in which the role of the γ/γ' -interfaces is included. More specifically, each phase in the material is represented by a combination of a bulk material unit cell region and several interface regions. In the interface regions internal stresses will develop as a result of the lattice misfit between the two phases and the plastic strain gradients, represented by non-uniform distributions of geometrically necessary dislocations (GNDs). Conditions requiring stress continuity and strain compatibility across the γ/γ' -interfaces are specified in these regions. Continuous dislocation densities and slip gradients, as typically used in a continuum formulation, are approximated here by piece-wise constant fields.

The limited complexity of the adopted unit cell and the micromechanical simplifications, which render a composition of 10 piece-wise uniformly deforming regions, make the framework particularly efficient in a multiscale approach. The unit cell response is determined numerically on a material point level (integration point level) within a macroscopic FE code, which is computationally much more efficient than a fully detailed FE-based unit cell. The material response is predicted accurately by using an extended version of an existing non-local strain gradient crystal plasticity model [37,38] for the matrix material. The precipitate is treated as an elastic anisotropic solid.

Finally, to reduce the model complexity, the mechanisms of precipitate shearing and rafting are omitted, which limits the application range of the present model somewhat. In the majority of the industrial gas turbines single crystal Ni-base superalloy blades operate at temperatures well below 950 °C and are not allowed to deform by more than 1 to 2%. Since the matrix phase of the material is known to accommodate the majority of the deformation, it is justified, at these operating conditions, to assume that the γ' -precipitates remain elastic during deformation. This means that the mechanism of precipitate shearing by dislocations is not considered. Experimental work [11,30,39-47,] has shown that precipitate shearing becomes important at temperatures above 950 °C and at larger strains (later stages of steady-

state creep). At lower temperatures considerable stresses in the range of 500 to 600 MPa are required to initiate particle shearing. Moreover, the morphology of the microstructure is assumed to remain the same during deformation, which also neglects the mechanism of rafting. Again experimental work [48] has shown that precipitate coarsening is completed rapidly at temperatures above 950 °C and after proportionally longer times at lower temperatures. Consequently, the assumption of an elastic precipitate and a fixed morphology limits the application region of the present model to temperatures below 950 °C and strains smaller than about 5% and also to relatively short loading times. However, this limited application range is sufficient to demonstrate the importance of strain gradient effects in nickel-base superalloys. Moreover, future extension of the model with precipitate deformation mechanisms (chapter 3) and rafting kinetics (chapter 5) can remove the present limitations.

To summarize, the original aspect of the present model is the incorporation of strain gradient effects, which are not included in the majority of the existing models, in an efficient multiscale framework. Due to the micromechanical simplifications, the present model is computationally much more efficient than the strain gradient FE unit cell models.

In the next section the multiscale framework is outlined, providing definitions of the unit cell and the interaction laws. Then the strain gradient effects are implemented, both in the hardening law and through internal stresses: section 2.3 describes the constitutive models that are used, focusing mainly on the strain gradient crystal plasticity concepts, while section 2.4 considers the internal stresses, describing the formulation of misfit and strain gradient induced back stresses. In section 2.5, the model is applied to the Ni-base superalloy CMSX-4. Simulated stress-strain curves and size effects are compared to experimental results, showing that the present framework is able to describe the material response and size effects to a level of detail similar to complex FE unit cell models, while being computationally much more efficient. The computational efficiency is demonstrated by applying the model to a gas turbine blade finite element analysis. Finally, section 2.6 forwards some concluding remarks.

2.2 Multiscale model description

The strain gradient effects are incorporated in a newly developed multiscale model for the prediction of the superalloy mechanical behaviour. This model covers several length scales, which is shown schematically in Figure 2-2a. The *macroscopic* length scale characterises the engineering level on which a finite element (FE) model is commonly used to solve the governing equilibrium problem. The *mesoscopic* length scale

represents the level of the microstructure within a macroscopic material point. At this length scale the material is considered as a compound of two different phases: γ' -precipitates embedded in a γ -matrix. Finally, the *microscopic* length scale reflects the crystallographic response of the individual material phases. The constitutive behaviour is defined on this level using a strain gradient crystal plasticity framework.

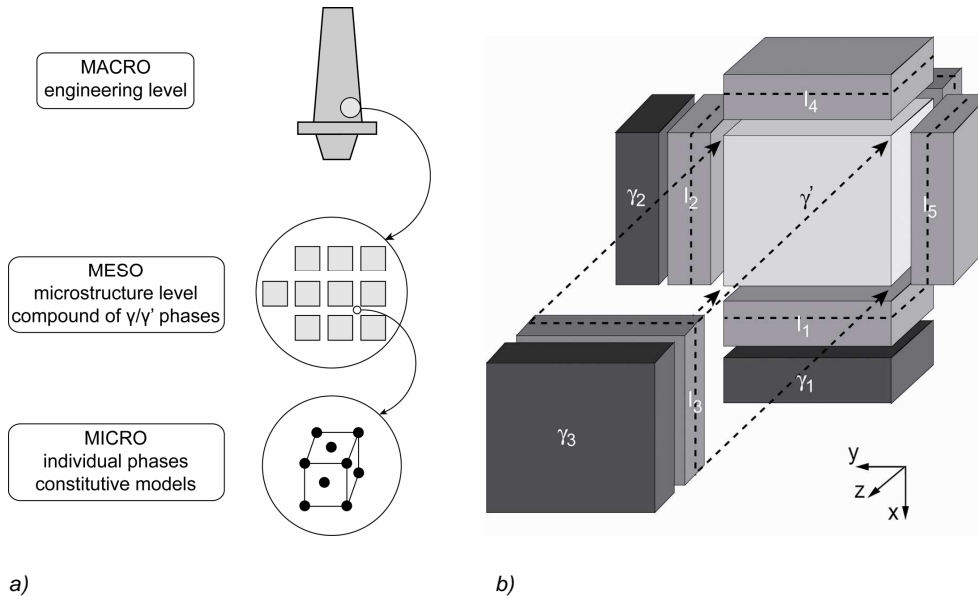


Figure 2-2 Schematic overview of the model, showing (a) the multiscale character and (b) the multi-phase unit cell, consisting of one precipitate (γ'), three matrix (γ_i) and six double interface (l_i) regions.

Considering the overall deformation level, a small strain approximation will be used in the model. The intended application of the model is the analysis of gas turbine components in which deformations are small. Consequently, the initial and deformed state are geometrically nearly identical. Instead of a large deformation strain tensor, the linear strain tensor ($\boldsymbol{\epsilon}$) will be used with the Cauchy stress tensor ($\boldsymbol{\sigma}$) as the appropriate stress measure.

In this section the different aspects of the material point model are described. Firstly the mesoscopic unit cell is defined, after which the scale transitions and interaction laws are described.

2.2.1 Unit cell definition

On the material point level the Ni-base superalloy microstructure, consisting of γ' -precipitates in a γ -matrix, is represented by a unit cell containing 16 regions (see Figure 2-2b):

- 1 γ' -precipitate region
- 3 γ -matrix channel regions (γ_j , $j = 1 \dots 3$) with different orientations (normal to the $[001]$, $[010]$ and $[100]$ directions, which are parallel in both phases)
- 12 interface regions (I_k^m and I_k^p , $k = 1 \dots 6$) containing the γ/γ' -interfaces. A matrix and a precipitate region together form a bi-crystal, see Figure 2-3, which is located on each face of the γ' -precipitate.

The interface between the two different phases plays an important role in the mechanical behaviour of the material, especially due to the large strain gradients that develop here. Therefore, special interface regions were included in the model to take into account the processes that take place at the γ/γ' -interfaces. Consequently, each phase in the two-phase material, either a precipitate or a matrix channel, is represented by two types of regions in the unit cell. The first type represents the bulk material behaviour and in the second type all short-range interface effects, including dislocation induced back stress and interaction with other phases, are incorporated. Inside each individual region quantities, like stresses and strains, are assumed to be uniform, which leads to a particularly efficient framework. The only relevant quantity that is not uniformly distributed inside a region is the GND density, as will be shown in section 2.4.2.

Thus, in the present framework the behaviour of a specific phase in the real material, e.g. a matrix channel, is given by the (weighted) average behaviour of the bulk unit cell region and the appropriate sides of the interface regions. This also means that the individual unit cell regions will not necessarily describe the real deformation behaviour on their own. Finally note that, throughout this thesis, the word *phase* refers to a specific component in the real material, either matrix or precipitate, and the word *region* refers to a specific part of the model unit cell.

The constitutive behaviour of the matrix and precipitate fractions of the interface is identical to the behaviour of the bulk matrix and precipitate phases, respectively. However, additional interface conditions (section 2.2.2) are specified and short-range internal stresses (back stress, see section 2.4) are included in these regions, which distinguishes them from the matrix and precipitate regions. Another internal stress, the lattice misfit stress, is a long-range stress field, which is consequently included in both bulk and interface regions.

The morphology of the microstructure is defined by the values of the geometrical parameters L , w and h , as shown in Figure 2-3. The precipitate (γ') size, including the γ' -interface region, is given by the value of L in three directions (L_1 , L_2 and L_3). These values also determine two of the three dimensions of the three matrix channel regions (γ_i) and the six interface regions (I_k). The total channel width, including one channel and two γ -interface regions, is given by the parameter h_i for γ -channel i . Finally, the width of the interface regions is related to the values of L and h . The width of the matrix phase layer in the interface (I_i^m) is defined as 30% of the matrix channel width ($w_i^m = 0.30 h_i$) and the width of the precipitate layer in the interface (I_i^p) as 5% of the precipitate size ($w_i^p = 0.05 L_i$). The selection of these values will be motivated in section 2.5. The CMSX-4 microstructure (Figure 1-3) is rather regular, so for the present model the precipitates are assumed to be cubic with $L_1 = L_2 = L_3 = 500$ nm. The matrix channel width is taken as $h_1 = h_2 = h_3 = 60$ nm. These values yield a γ' volume fraction of 72%.

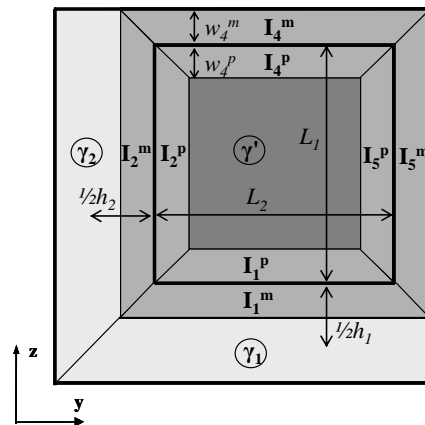


Figure 2-3 Definition of the unit cell dimensions in the y-z plane cross section.

As will be shown later, the interface regions at opposite sides of the precipitate (e.g. I_1^m and I_4^m) are assumed to behave identically in terms of deformation, internal stress development, etc. Therefore, to the benefit of computational efficiency, only half of the interface regions need to be included in the equations in the next subsections, thereby effectively reducing the number of regions from 16 to 10. The opposite regions are then incorporated in the volume averaging by doubling the respective volume fractions.

2.2.2 Scale transitions and interaction law

The relations between the different length scales of the model are shown schematically in Figure 2-4. Conventionally, a finite element method is used on the macroscopic level to solve the engineering problem with its boundary conditions. In the present multiscale approach the usual standard procedure to obtain the stress response for a given deformation (i.e. a local closed-form constitutive equation) is replaced by a mesoscopic calculation at the unit cell level as indicated in Figure 2-4.

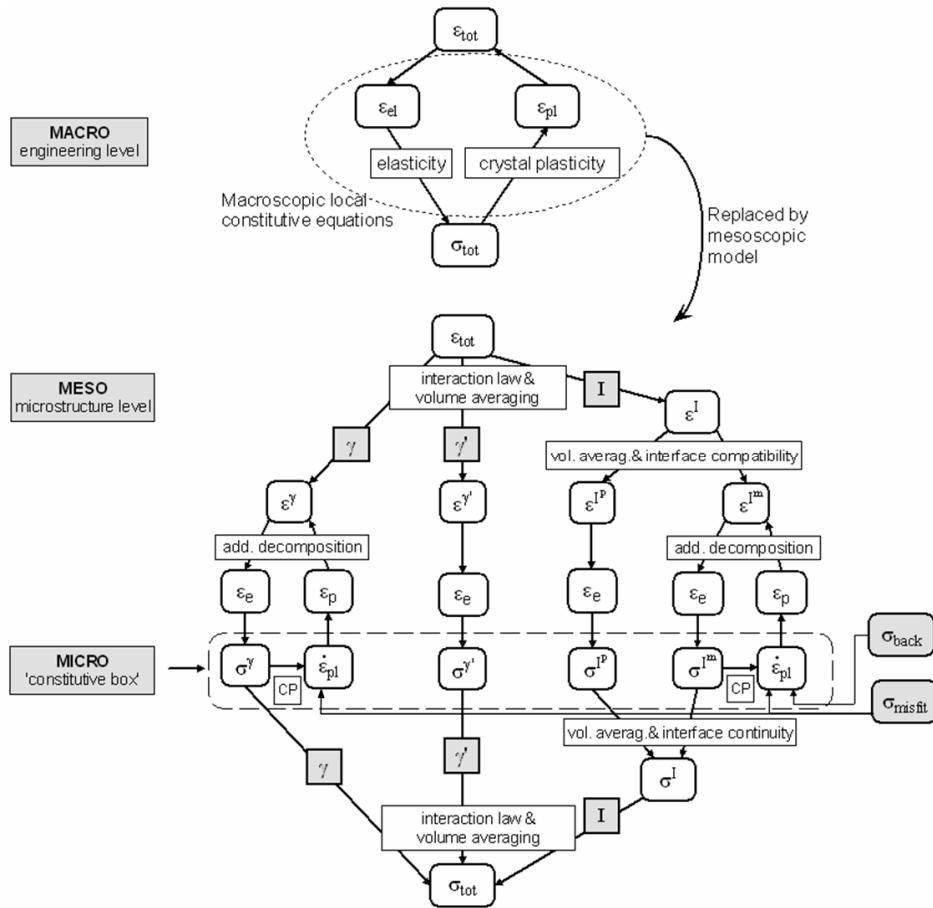


Figure 2-4 Overview of the interaction between the different levels of the multiscale model. In the macroscopic FE analysis, the usual standard procedure to obtain the stress response for a given deformation is replaced by a mesoscopic calculation at the unit cell level. A crystal plasticity (CP) model yields the relation between the local stress and plastic strain rate for the matrix regions.

The deformation (total strain) for a certain macroscopic material point during a time increment is provided by the macro scale and the stress response is returned after the computations at the mesoscopic level. The quantities used for this macro-meso scale transition are denoted as the mesoscopic average strain ($\boldsymbol{\varepsilon}_{tot}$) and the mesoscopic average stress ($\boldsymbol{\sigma}_{tot}$). The stress tensor $\boldsymbol{\sigma}_{tot}$ is determined from the strain tensor $\boldsymbol{\varepsilon}_{tot}$ based on the specified mesoscopic configuration and the local constitutive equations of the different phases at the micro level.

The mesoscopic strain is obtained by averaging the microstructural quantities in each of the regions, defined as

$$\sum_i f^i \boldsymbol{\varepsilon}_{tot}^i = \boldsymbol{\varepsilon}_{tot} \quad i = \gamma^1, \gamma_1, \gamma_2, \gamma_3, I_1^p, I_1^m, I_2^p, I_2^m, I_3^p, I_3^m \quad (2.1)$$

where f^i are the volume fractions and $\boldsymbol{\varepsilon}_{tot}^i$ the total strain tensors in the 10 different regions of the model.

The relation between the mesoscopic and microscopic level is provided by the constitutive models, which relate the stress tensors to the individual strain tensors for all 10 regions

$$\boldsymbol{\varepsilon}^i \rightarrow \text{constitutive box} \rightarrow \boldsymbol{\sigma}^i \quad i = \gamma^1, \gamma_1, \gamma_2, \gamma_3, I_1^p, I_1^m, I_2^p, I_2^m, I_3^p, I_3^m \quad (2.2)$$

The constitutive model at the micro level, for the matrix phase, is based on a strain gradient enhanced crystal plasticity theory and will be described in section 2.3. The precipitate phase is treated as an elastic medium. Also, only at this point the internal stresses (misfit and back stress, see section 2.4) play a role in the stress analysis. They are combined with the externally applied stress, as obtained from the equilibrium calculation, to form an effective stress that is used in the constitutive box. They are thus not part of the equilibrium calculation itself, as is also indicated in Figure 2-4. This separation of external and internal stress calculation is particularly possible in the context of the adopted Sachs approach (to be outlined in the following), as will be discussed in section 2.4.1.

Inside each of the different regions, both stress and deformation are assumed to be uniform. To specify the coupling between the regions an interaction law has to be defined. Two frequently adopted limit cases can be distinguished:

- Taylor interaction: deformation is uniform across the regions, stresses may vary;
- Sachs interaction: stresses are uniform across the regions, deformation may vary.

These two approaches form an upper and a lower bound for the stiffness, so the real mechanical behaviour intermediates between these cases. A Taylor-type interaction usually yields a response that is too stiff, thereby overestimating the resulting stresses for a given deformation, whereas a Sachs type interaction yields an overly weak

response. A Taylor interaction model is inappropriate for the present application, since the deformation is highly localized in the γ -matrix phase. A Sachs-type approach is actually a much better approximation, but it lacks the ability to incorporate kinematical compatibility conditions at the interface. Also, it would not correctly represent the stress redistribution between the two phases that occurs when the matrix starts to deform plastically. Therefore, a hybrid interaction law [49] or a modified Taylor / Sachs approach [21] is best suited here.

For the present model a modified Sachs approach is used, in which the requirement of a uniform stress state is relaxed for the interface regions. In the γ' - and γ -regions the stresses are required to be equal to the mesoscopic stress. In each pair of interface regions however, only the *average* stress is enforced to be equal to the mesoscopic stress. This results in the following equations:

- Sachs interaction between γ' - and γ -regions:

$$\boldsymbol{\sigma}^{\gamma'} = \boldsymbol{\sigma}^{\gamma_1} = \boldsymbol{\sigma}^{\gamma_2} = \boldsymbol{\sigma}^{\gamma_3} = \boldsymbol{\sigma}_{tot} \quad (2.3)$$

- Modified Sachs interaction for the bi-crystal interfaces:

$$f^{I_k^p} \boldsymbol{\sigma}^{I_k^p} + f^{I_k^m} \boldsymbol{\sigma}^{I_k^m} = (f^{I_k^p} + f^{I_k^m}) \boldsymbol{\sigma}_{tot} \quad k = 1, 2, 3 \quad (2.4)$$

where $\boldsymbol{\sigma}^i$ are the stress tensors in the different regions, $\boldsymbol{\sigma}_{tot}$ is the mesoscopic stress tensor and f^i are the volume fractions of the respective regions.

The fact that each partition of the interface region may respond differently to a mechanical load enables the possibility (and necessity) to define additional conditions at the interfaces. Both stress continuity (across the interface) and kinematical compatibility (in the plane of the interface) are therefore added as additional requirements. This leads to the following supplementary equations, where \vec{n}^k is the unit normal vector on the k^{th} interface.

- Compatibility between the matrix (I_k^m) and the precipitate side (I_k^p) of the k^{th} interface:

$$\boldsymbol{\varepsilon}^{I_k^p} \cdot (\mathbf{I} - \vec{n}^k \vec{n}^k) = \boldsymbol{\varepsilon}^{I_k^m} \cdot (\mathbf{I} - \vec{n}^k \vec{n}^k) \quad k = 1, 2, 3 \quad (2.5)$$

- Traction continuity at the same interface:

$$\boldsymbol{\sigma}^{I_k^p} \cdot \vec{n}^k = \boldsymbol{\sigma}^{I_k^m} \cdot \vec{n}^k \quad k = 1, 2, 3 \quad (2.6)$$

where $\boldsymbol{\sigma}$ and $\boldsymbol{\varepsilon}$ are the stress and strain tensors in the different regions.

For the material point model the mesoscopic deformation (total strain) is provided by the macro scale analysis and the mesoscopic stress must be calculated. Since the model consists of 10 distinct regions in which the deformation and stress are

homogeneous, and the symmetric stress and strain tensors contain 6 independent components, a total of 120 unknowns results. The systems (2.1) and (2.3) - (2.6) represent a total number of 60 equations, while the constitutive model (2.2) adds another 60 equations, which completes the description.

In summary, the stresses in the bulk material regions and the *average* stresses of the interface regions are coupled, whereas for the interface regions additional interface conditions in terms of stress and strain are specified. The assumption of uniform stress and strain inside the unit cell regions in combination with the conditions proposed above completely determine the problem. Additional conditions are not required nor allowed, which means that, for example, the absence of traction continuity between bulk material and interface is accepted for the sake of efficiency.

2.3 Constitutive behaviour

A strain gradient enhanced crystal plasticity approach is used to model the constitutive behaviour of the matrix phase, whereas the precipitate is treated as an elastic anisotropic material. After a general introduction concerning the underlying crystal plasticity formulation, the matrix and precipitate constitutive models will be described. Note that the matrix phase constitutive model is applied to both bulk matrix unit cell regions and the matrix sides of the interface regions. The precipitate regions and the precipitate sides of the interface regions remain elastic.

2.3.1 Strain gradient crystal plasticity

In a conventional crystal plasticity framework, the plastic deformation of metals is a natural consequence of the process of crystallographic slip. For each type of crystal lattice a set of slip systems exists along which the slip process will take place. A slip system is commonly characterised by its slip plane and its slip direction. For the considered superalloy, with a face-centred cubic (FCC) lattice, 3 slip directions on each of the 4 octahedral slip planes can be identified, resulting in 12 slip systems. In addition to the plastic slip, elastic deformation is accommodated by distortion of the crystallographic lattice. In many superalloy crystal plasticity models [3,23,24] an additional set of cubic slip systems is incorporated to account for the cross slip mechanisms that occur when the material is loaded in a direction other than $\langle 001 \rangle$. The present model here is only applied to the technologically important $\langle 001 \rangle$ loading direction, corresponding to the direction of centrifugal loading in turbine blades. However, a set of cubic slip systems can easily be incorporated if it is required to deal with other orientations.

Table 2-1 List of indices and vectors for dislocation densities and their slip systems in an FCC metal.

Dislocation density ξ	Slip system type	Slip system α	Slip direction \vec{s}	Slip plane normal \vec{n}
1	edge	1	$\frac{1}{2}\sqrt{2} [\bar{1}10]$	$\frac{1}{3}\sqrt{3} [111]$
2	edge	2	$\frac{1}{2}\sqrt{2} [10\bar{1}]$	$\frac{1}{3}\sqrt{3} [111]$
3	edge	3	$\frac{1}{2}\sqrt{2} [0\bar{1}1]$	$\frac{1}{3}\sqrt{3} [111]$
4	edge	4	$\frac{1}{2}\sqrt{2} [\bar{1}\bar{1}0]$	$\frac{1}{3}\sqrt{3} [1\bar{1}\bar{1}]$
5	edge	5	$\frac{1}{2}\sqrt{2} [101]$	$\frac{1}{3}\sqrt{3} [1\bar{1}\bar{1}]$
6	edge	6	$\frac{1}{2}\sqrt{2} [01\bar{1}]$	$\frac{1}{3}\sqrt{3} [1\bar{1}\bar{1}]$
7	edge	7	$\frac{1}{2}\sqrt{2} [110]$	$\frac{1}{3}\sqrt{3} [\bar{1}\bar{1}\bar{1}]$
8	edge	8	$\frac{1}{2}\sqrt{2} [\bar{1}01]$	$\frac{1}{3}\sqrt{3} [\bar{1}\bar{1}\bar{1}]$
9	edge	9	$\frac{1}{2}\sqrt{2} [0\bar{1}\bar{1}]$	$\frac{1}{3}\sqrt{3} [\bar{1}\bar{1}\bar{1}]$
10	edge	10	$\frac{1}{2}\sqrt{2} [1\bar{1}0]$	$\frac{1}{3}\sqrt{3} [\bar{1}\bar{1}\bar{1}]$
11	edge	11	$\frac{1}{2}\sqrt{2} [\bar{1}0\bar{1}]$	$\frac{1}{3}\sqrt{3} [\bar{1}\bar{1}\bar{1}]$
12	edge	12	$\frac{1}{2}\sqrt{2} [011]$	$\frac{1}{3}\sqrt{3} [\bar{1}\bar{1}\bar{1}]$
13	screw	-4 or 7	$\frac{1}{2}\sqrt{2} [110]$	$\frac{1}{3}\sqrt{3} [1\bar{1}\bar{1}]$ or $\frac{1}{3}\sqrt{3} [\bar{1}\bar{1}\bar{1}]$
14	screw	5 or -11	$\frac{1}{2}\sqrt{2} [101]$	$\frac{1}{3}\sqrt{3} [1\bar{1}\bar{1}]$ or $\frac{1}{3}\sqrt{3} [\bar{1}\bar{1}\bar{1}]$
15	screw	-9 or 12	$\frac{1}{2}\sqrt{2} [011]$	$\frac{1}{3}\sqrt{3} [\bar{1}\bar{1}\bar{1}]$ or $\frac{1}{3}\sqrt{3} [\bar{1}\bar{1}\bar{1}]$
16	screw	1 or -10	$\frac{1}{2}\sqrt{2} [\bar{1}\bar{1}0]$	$\frac{1}{3}\sqrt{3} [111]$ or $\frac{1}{3}\sqrt{3} [\bar{1}\bar{1}\bar{1}]$
17	screw	2 or -8	$\frac{1}{2}\sqrt{2} [10\bar{1}]$	$\frac{1}{3}\sqrt{3} [111]$ or $\frac{1}{3}\sqrt{3} [\bar{1}\bar{1}\bar{1}]$
18	screw	3 or -6	$\frac{1}{2}\sqrt{2} [0\bar{1}1]$	$\frac{1}{3}\sqrt{3} [111]$ or $\frac{1}{3}\sqrt{3} [1\bar{1}\bar{1}]$

Clearly, crystallographic slip is carried by the movement of dislocations. Yet, also the hardening behaviour of metals is attributed to dislocations. Plastic deformation causes multiplication of dislocations and their mutual interaction impedes the motion of gliding dislocations, which causes strengthening. The total dislocation population can be considered to consist of two parts:

- statistically stored dislocations (SSDs)
- geometrically necessary dislocations (GNDs) [50]

The SSDs are randomly oriented and therefore do not have any directional effect and no net Burgers vector. They accumulate through a statistical process. On the other hand, when a gradient in the plastic deformation occurs in the material, a change of the GND density is required to maintain lattice compatibility. Individual dislocations

cannot be distinguished as SSDs or GNDs. The GNDs are therefore the fraction of the total dislocation population with a non-zero net Burgers vector. Moreover, as will be shown later, a gradient in the GND density causes an internal stress which affects the plastic deformation. These strain gradient dependent influences give the model a non-local character. They enable the prediction of size effects which cannot be captured by conventional crystal plasticity theories.

In the present model it is assumed that all SSD densities are of the edge type, whereas for the GNDs both edge and screw dislocations are considered. This implies that for an FCC metal 12 edge SSD densities are taken into account, next to 12 edge and 6 screw GND densities [51]. A complete overview of the dislocation densities, including their type and slip system is given in Table 2-1. Each screw dislocation can move on either of the two slip planes in which it can reside. This is indicated in Table 2-1 by the two corresponding slip system numbers, where a negative number means that the defined slip direction should be reversed.

The elastic material behaviour is modelled using a standard formulation for orthotropic materials with cubic symmetry. The three independent components of the elastic tensor ${}^4\mathbf{C}$ of both phases in CMSX-4 at 850 °C are given in Table 2-2 [24].

Table 2-2 ${}^4\mathbf{C}$ elastic tensor components for CMSX-4 at 850 °C [24].

	γ -matrix	γ' -precipitate
C_{1111} (GPa)	190.9	216.9
C_{1122} (GPa)	127.3	144.6
C_{1212} (GPa)	100.2	105.2

The next subsection shows how the strain gradient based crystal plasticity framework is used to elaborate the matrix phase constitutive model.

2.3.2 Matrix constitutive model

The basic ingredient of the crystal plasticity framework is the relation between the slip rates $\dot{\gamma}^\alpha$ and the resolved shear stresses τ^α for all the slip systems α . The following formulation is proposed here:

$$\dot{\gamma}^\alpha = \dot{\gamma}_0 \left\{ \frac{|\tau_{eff}^\alpha|}{s^\alpha} \right\}^m \left\{ 1 - \exp\left(-\frac{|\tau_{eff}^\alpha|}{\tau^{or}}\right) \right\}^n \text{sign}(\tau_{eff}^\alpha) \quad (2.7)$$

where τ^{or} denotes the Orowan stress, s^α the actual slip resistance and τ_{eff}^α the effective shear stress on slip system α , obtained from the effective stress tensor $\boldsymbol{\sigma}_{eff}$ by

$$\tau_{\text{eff}}^{\alpha} = \sigma_{\text{eff}} : \mathbf{P}^{\alpha} \quad (2.8)$$

where \mathbf{P}^{α} is the symmetric Schmid tensor defined as

$$\mathbf{P}^{\alpha} = \frac{1}{2}(\bar{s}^{\alpha}\bar{n}^{\alpha} + \bar{n}^{\alpha}\bar{s}^{\alpha}) \quad (2.9)$$

The unit length vectors \bar{n}^{α} and \bar{s}^{α} are the slip plane normal and slip direction, respectively. The effective stress tensor is defined as the combination of the externally applied stress, the back stress and the misfit stress (see section 4) according to

$$\sigma_{\text{eff}} = \sigma + \sigma_{\text{misfit}} - \sigma_b \quad (2.10)$$

The formulation in equation (2.7) is an extended version of the slip law used in the work of Evers et al. [37,38] for a single phase FCC material. For the present two-phase material an additional threshold term is added to account for the Orowan stress, which is the stress required to bow a dislocation line into the channel between two precipitates. This stress is given by [52] as

$$\tau^{\text{or}} = \frac{\mu b}{2\pi d} \ln\left(\frac{d}{r_0}\right) = \alpha \frac{\mu b}{d} \quad (2.11)$$

where μ is the shear modulus, b the length of the Burgers vector, d the spacing between two precipitates (equal to the channel width) and r_0 the dislocation core radius (in the order of b). There is no generally accepted value for the constant α . The used values range from 0.238 to 2.15 for different materials and conditions [22-24,27-29,42,52], where in some cases the constant α was used as an adjustable parameter. A value of $\alpha = 0.85$ is taken here, as was done by Busso et al. [24]. If the effective stress exceeds this Orowan stress threshold, dislocation lines enter the matrix channel and the typical slip threshold (governed by s^{α}) determines whether or not they can move any further. This is the case if the effective stress exceeds the slip resistance. The slip resistance is in a certain sense also an Orowan type stress related to the average spacing of obstacles inside the matrix phase, such as other dislocation segments. While both thresholds are a result of microscopic phenomena, the Orowan threshold is related to a mesoscopic length scale. Moreover, the slip resistance threshold term determines the actual slip rate value, whereas the Orowan threshold is essentially active or inactive (as the exponential term is ranging from 0 to 1). As soon as the Orowan threshold τ^{or} is exceeded by the effective stress or when the growth of the dislocation density triggers an increase of the slip resistance s^{α} to a value that exceeds the Orowan threshold, the slip resistance contribution becomes the active threshold that determines the slip rate.

Slip resistance

Generally speaking, slip resistance or dislocation drag is caused by several obstacles such as solute atoms, precipitates (e.g. carbides, intermetallics, secondary γ' -particles) and other dislocations, each having a contribution to the overall slip resistance. The physical mechanism associated with an increasing slip rate at increasing temperature is the decrease of dislocation drag (related to the slip resistance). The temperature dependence of all these contributions is assumed to be identical, resulting in a classical expression for the temperature dependent slip resistance

$$s^\alpha = s_0^\alpha \exp\left[\frac{Q}{kT}\right] \quad (2.12)$$

where s_0^α is the athermal slip resistance, Q is an activation energy for overcoming the barriers, $k = 1.38 \cdot 10^{-23} \text{ J K}^{-1}$ is the Boltzmann constant and T the absolute temperature.

The amount and spacing of solute atoms and precipitates (other than γ') in the matrix phase is assumed to be constant, which means that the isothermal lattice slip resistance due to these obstacles is constant as well. The second contribution to the total slip resistance depends on the dislocation densities in the material. This contribution is related to the resistance of sessile / forest dislocations and therefore depends on the total dislocation density, composed of the SSDs and the GNDs. The relation between the slip resistance and the dislocation density is defined according to

$$s_{disl}^\alpha = c\mu b \sqrt{|\rho_{SSD}^\alpha| + |\rho_{GND}^\alpha|} \quad (2.13)$$

where c is a strength parameter. Evers et al. [37] used an interaction matrix containing experimentally determined entries to define the interactions between dislocations on different slip systems. These values are not available for Ni-base superalloys, so only interactions with dislocations on the same slip system (self hardening) will be taken into account, as was done by Busso et al. [24]. Interactions with dislocations on other slip systems (cross hardening) are neglected. Also the contribution to the slip resistance of the screw-type GND densities ($\xi = 13 \dots 18$) whose slip plane is ambiguous (see Table 2-1) is neglected.

The exploitation of equation (2.13) requires the knowledge of all dislocation densities (12 edge dislocation densities for the SSDs and 12 edge and 6 screw dislocation densities for the GNDs). The GND densities can be obtained from the plastic deformation gradients in the material as will be explained in section 2.4.2 dealing with the back stresses. The SSD densities are calculated on the basis of an appropriate evolution equation [37], starting from their initial value $\rho_{SSD,0}$:

$$\dot{\rho}_{SSD}^{\alpha} = \frac{1}{b} \left(\frac{1}{L^{\alpha}} - 2\gamma_c \rho_{SSD}^{\alpha} \right) |\dot{\gamma}^{\alpha}|, \quad \rho_{SSD}^{\alpha}(t=0) = \rho_{SSD,0}^{\alpha} \quad (2.14)$$

which is the net effect of dislocation accumulation (left term) and annihilation (right term). The parameter γ_c represents the critical annihilation length, i.e. the average distance below which two dislocations of opposite sign annihilate spontaneously. The accumulation rate is linked to the average dislocation segment length of mobile dislocations on system α , which is determined by the current dislocation state through

$$L^{\alpha} = \frac{K}{\sqrt{|\rho_{SSD}^{\alpha}| + |\rho_{GND}^{\alpha}|}} \quad (2.15)$$

where K is a material constant.

Further, the experimental tensile curves in section 2.5 show that after some amount of yielding strain softening occurs in the material. This phenomenon is typical for superalloys and has been the subject of several studies. Busso and co-workers [8,24,53] and Choi et al. [26] performed unit cell finite element analyses and concluded that the softening might be attributed to lattice rotations around the corners of the precipitates. These rotations induce activation of additional slip systems and result in a fast increase of plastic slip. In these analyses, the precipitate was assumed to behave elastically. On the other hand, Fedelich [23] states that the softening is related to the onset of precipitate shearing, a phenomenon which was not accounted for in the FE unit cell analyses mentioned above.

The present model is specifically developed to be efficient in a multiscale approach. The consequential choice for small strain kinematics and uniform stress and strain in the unit cell regions mean that local lattice rotations cannot be predicted. Also the mechanism of precipitate shearing is not included. Therefore, in the present framework the softening effect is incorporated in a phenomenological way by adding a softening term

$$s_{soft}^{\alpha} = C_{soft} \left(1 - \sqrt{\frac{\rho_{SSD}^{\alpha}}{\tilde{\rho}_{SSD}^{\alpha}}} \right)^p \quad (2.16)$$

to the slip resistance, where C_{soft} and p are constants and $\tilde{\rho}_{SSD}^{\alpha}$ is the equilibrium value of the SSD density. This equilibrium value follows from equation (2.14) by requiring that the creation and annihilation terms are equal. Rather than a real slip resistance, the contribution s_{soft}^{α} should be considered as a reflection of the lack of dislocation mobility. It represents, in a phenomenological way, the increase of dislocation mobility, and consequential decrease of s^{α} , associated with either local lattice rotations or precipitate

shearing. In forthcoming work, a precipitate constitutive model will be proposed to properly capture precipitate shearing. The need for a phenomenological term that accounts for softening will then be re-assessed.

Finally, it is assumed that the athermal *lattice* slip resistance is caused by an initial SSD density $\rho_{SSD,0}$, which means that its effect on the total slip resistance is incorporated in the *dislocation* slip resistance as given by equation (2.13). Therefore, combination of equations (2.13) and (2.16) yields the total athermal slip resistance to be used in equation (2.12):

$$s_0^\alpha = s_{disl}^\alpha + s_{soft}^\alpha \quad (2.17)$$

2.3.3 Precipitate constitutive model

In the present approach, the precipitate in the superalloy is assumed to be elastic, which implies that both the unit cell precipitate region and the precipitate sides of the interface regions are treated as anisotropic elastic media. As was mentioned in the introduction, this assumption is only acceptable under certain conditions. The precipitate may deform inelastically when it is sheared by a dislocation or bypassed by dislocation climb. However, these processes have considerable thresholds in terms of stress and temperature. Therefore, at temperatures below 950 °C and moderate stress levels the simplification of an elastically deforming precipitate is justified. These conditions are, nevertheless, sufficient to demonstrate the importance of strain gradient effects, which is the aim of the present chapter. The development of an enhanced constitutive model that includes crystal plasticity in the precipitate for more extreme conditions, will be treated in chapter 3.

2.4 Internal stresses

The interface between the two different phases plays an important role in the mechanical behaviour of the multi-phase material, because of the development of significant internal stresses that interact with the externally applied stress, see (2.10). In the present model the following internal stresses are incorporated:

- misfit stress: stress that originates from the lattice misfit between the γ and γ' -phases at the level of the coherent interface that is formed. This is a *long-range* stress field that spans the complete unit cell.
- back stress: stress that originates from deformation-induced plastic strain gradients inducing a gradient in the GND density at the interfaces. This is a *short-range* stress field that only acts in the interface regions.

Apart from these two explicitly defined internal stress fields, an internal redistribution of stresses occurs due to differences in plastic deformation between both phases.

2.4.1 Lattice misfit

The γ and γ' -phases both have an FCC lattice structure with a slightly different lattice (dimension) parameter. They form a coherent interface, which means that the crystal lattice planes are continuous across the interface, but a misfit strain exists to accommodate the difference in lattice parameter. For most superalloys the misfit is called negative, which means that the lattice parameter of the precipitate is smaller than the matrix lattice parameter. To bridge the misfit, both the precipitate and matrix are strained, causing compressive misfit stresses in the matrix (parallel to the interface) and tensile stresses in the precipitate.

The amount of straining of the matrix and precipitate is dependent on the magnitude of the misfit, the elastic moduli of both materials and their relative sizes [54]. The unconstrained misfit is defined as

$$\delta = \frac{a_{\gamma'} - a_{\gamma}}{a_{\gamma}} \quad (2.18)$$

with $a_{\gamma'}$ and a_{γ} the lattice parameters of the γ' and γ -phases respectively. If the coefficient of thermal expansion is not equal for both phases, the misfit is temperature dependent, since the difference in lattice parameter changes with temperature. The misfit is assumed to be accommodated equally by both phases, leading to a misfit strain

$$\varepsilon_{misfit} = \frac{\frac{1}{2}(a_{\gamma'} - a_{\gamma})}{a_{\gamma}} \quad (2.19)$$

in the matrix (in the two directions in the plane of the interface) and the same strain with opposite sign in the precipitate. Using the normal vector of the interface \vec{n}^i , the components of the misfit strain tensor are defined as

$$\varepsilon_{misfit}^i = \varepsilon_{misfit} (\mathbf{I} - \vec{n}^i \vec{n}^i) + \varepsilon_n^i \vec{n}^i \vec{n}^i \quad (2.20)$$

with ε_{misfit} given by (2.19) for the matrix regions and with ε_n^i the misfit strain in normal direction resulting from the requirement that the associated stress component vanishes. This misfit strain tensor represents an initial elastic strain (also called eigenstrain), triggering an initial stress in each of the regions. Since the misfit is accommodated *elastically* in both phases, the misfit stress and strain tensor are directly related to each other by a modified (plane stress) elastic stiffness tensor ${}^4\mathbf{B}_{misfit}^i$, which ensures that only the stress components parallel to the interface are non-zero

$$\boldsymbol{\sigma}_{misfit}^i = {}^4\mathbf{B}_{misfit}^i : \boldsymbol{\varepsilon}_{misfit}^i \quad (2.21)$$

Usually, the misfit strain is used as an initial strain in the equilibrium calculation of the local stresses. However, in an approach that is based on the Sachs interaction law this is not straightforward, since the different regions are coupled by their stresses, which affects the stress redistribution due to the misfit strains. At the same time, the use of the Sachs interaction law makes it possible to superpose a separately calculated internal stress [e.g. misfit stress, equation (2.21)] to the calculated local stress to constitute an effective stress tensor. The effective stress tensor is then used in the constitutive law, equation (2.2), to calculate the plastic strains.

The misfit between the two phases can be partially relaxed by plastic deformation of one or both phases. Plastic deformation generates misfit dislocations at the interface resulting in a loss of coherency between the phases and a corresponding relaxation of the misfit. When the total misfit strain would be completely accommodated by plastic slip, the effective stresses in both phases would be similar and the misfit would effectively vanish. For the interface regions this is automatically ensured by the compatibility requirements, according to equation (2.5). Plastic deformation in one region causes a local stress redistribution across the two phases and a corresponding decrease of the misfit. For the bulk regions (1 precipitate and 3 matrix regions), which are not subject to compatibility requirements, the absolute values of the misfit strain components [equation (2.20)] are reduced by the absolute value of the plastic strain difference ($\Delta\boldsymbol{\varepsilon}_{pl}^i$) between the two phases, until the misfit completely vanishes:

$$\left| \boldsymbol{\varepsilon}_{misfit,ij}^i \right| \rightarrow \left| \boldsymbol{\varepsilon}_{misfit,ij}^i \right| - \left| \Delta\boldsymbol{\varepsilon}_{pl,ij}^i \right| \quad (2.22)$$

This simulates the loss of coherency due to plastic deformation in one or both phases. When a tensile stress is applied to the material, the effective stress in the matrix channels parallel to the loading direction will be lowered by the compressive misfit stress. This is not the case for the channels perpendicular to the loading axis, and it is generally accepted now that the deformation is initially localized in these matrix channels.

2.4.2 Strain gradient induced back stress

The back stress on a slip system originates from the spatial distribution of dislocations and is therefore only related to the GND density. For SSDs, which usually have a random orientation, the back stress contribution will be negligible. The value of the

back stress tensor is calculated by summation of the internal stress fields caused by the individual edge and screw dislocation densities.

$$\boldsymbol{\sigma}_b = -(\boldsymbol{\sigma}_e^{\text{int}} + \boldsymbol{\sigma}_s^{\text{int}}) \quad (2.23)$$

For a field of edge dislocations the stress field in a point is approximated by summation of the contributions of all dislocation systems ξ in a region with radius R around that point [55], resulting in

$$\boldsymbol{\sigma}_e^{\text{int}} = \frac{\mu b R^2}{8(1-\nu)} \sum_{\xi=1}^{12} \bar{\nabla} \rho_{GND}^{\xi} \cdot (3\bar{n}^{\xi} \bar{s}^{\xi} \bar{s}^{\xi} - \bar{s}^{\xi} \bar{s}^{\xi} \bar{n}^{\xi} - \bar{s}^{\xi} \bar{n}^{\xi} \bar{s}^{\xi} + \bar{n}^{\xi} \bar{n}^{\xi} \bar{n}^{\xi} + 4\nu \bar{n}^{\xi} \bar{p}^{\xi} \bar{p}^{\xi}) \quad (2.24)$$

where the vectors \bar{s} and \bar{n} are in the direction of the Burgers vector and slip plane normal respectively and \bar{p} is defined as $\bar{p} = \bar{s} \times \bar{n}$, i.e. the dislocation line vector for an edge dislocation.

For the field of screw dislocations the stress field is given by

$$\boldsymbol{\sigma}_s^{\text{int}} = \frac{\mu b R^2}{4} \sum_{\xi=13}^{18} \bar{\nabla} \rho_{GND}^{\xi} \cdot (-\bar{n}^{\xi} \bar{s}^{\xi} \bar{p}^{\xi} - \bar{n}^{\xi} \bar{p}^{\xi} \bar{s}^{\xi} + \bar{p}^{\xi} \bar{s}^{\xi} \bar{n}^{\xi} + \bar{p}^{\xi} \bar{n}^{\xi} \bar{s}^{\xi}) \quad (2.25)$$

where $\bar{p} = \bar{s} \times \bar{n}$ is now perpendicular to the dislocation line direction (since the Burgers vector is parallel to the dislocation line). Note that only a non-zero gradient of the GND densities causes a non-vanishing contribution.

To calculate the back stress, it is necessary to know the distribution of the dislocation densities for all individual slip systems. These densities can be obtained from the slip gradients in the material. Since the two phases form a coherent interface this can be done on the slip system level [38,55]. Slip gradients in the direction of the slip will be accommodated by edge dislocations while slip gradients perpendicular to the slip direction will be accommodated by screw dislocations. For the edge dislocations ($\xi = 1 \dots 12$) the GND densities are obtained from the slip gradients by

$$\rho_{GND}^{\xi} = \rho_{GND,0}^{\xi} - \frac{1}{b} \bar{\nabla} \gamma^{\xi} \cdot \bar{s}^{\xi} \quad (2.26)$$

and for the screw dislocations ($\xi = 13 \dots 18$) by

$$\rho_{GND}^{\xi} = \rho_{GND,0}^{\xi} + \frac{1}{b} (\bar{\nabla} \gamma^{\alpha_1} \cdot \bar{p}^{\alpha_1} + \bar{\nabla} \gamma^{\alpha_2} \cdot \bar{p}^{\alpha_2}) \quad (2.27)$$

The screw dislocation densities are the result of the combined effect of the slip gradients on the two available slip planes α_1 and α_2 , as given in Table 2-I. The initial values of the GND densities, $\rho_{GND,0}^{\xi}$, can be used to account for pre-deformation effects, if necessary.

Since the real deformation distribution in the unit cell is simplified by assuming uniform deformation inside each region, gradients in slip are captured through discrete steps in between regions only. This is illustrated in Figure 2-5, where the solid curve represents the expected distribution of plastic slip and the set of horizontal solid lines the piecewise uniform approximation. The GND density distribution corresponding to the real deformation is approximated by the dashed line. The gradients in the dislocation density and slip, as used in the equations (2.24)-(2.27), are replaced by their piece-wise discrete analogues. For example, when defined relative to a x,y,z -coordinate system, the gradient in GND density can be written as

$$\bar{\nabla} \rho_{GND}^{\epsilon} \approx \frac{\Delta \rho_{GND}^{\epsilon}}{l} \bar{n}_x \quad (2.28)$$

for the interface regions with their normal in the x -direction. In this relation $\Delta \rho_{GND}$ is the difference in GND density between both sides of the region and l is the width of the region. No gradient in y - or z -direction is present in these regions.

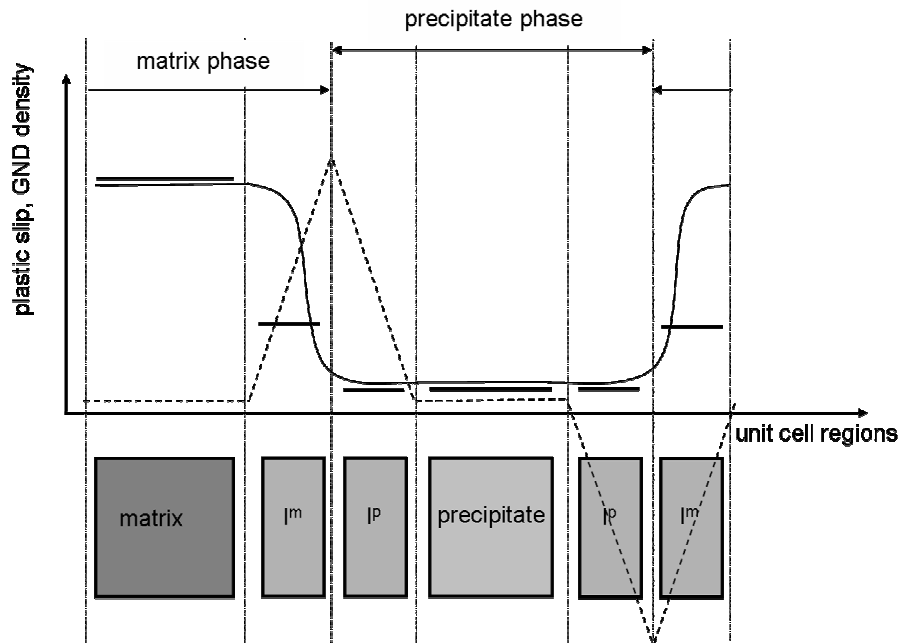


Figure 2-5 Overview of gradients in slip and GND density. The solid curved line represents the continuous plastic slip distribution that is expected in the real material and the series of straight solid lines the piecewise uniform approximation. The dashed line represents the GND density distribution.

Further, the slip gradient is assumed to be accommodated by the interface regions only, which means that the total slip difference between the matrix γ and a precipitate γ' is distributed over the two interface regions in between both bulk regions. Moreover, it is assumed that the GND densities increase (or decrease) linearly from zero in the γ - and γ' -regions to a maximum (or minimum) value at the boundary between the constituents of the interface regions (see Figure 2-5). According to equations (2.26)-(2.27) the GND density is proportional to the gradient in plastic slip. This gradient is based on the slip difference between the bulk γ - and γ' -regions. Due to the assumption of a linear variation of GND density inside a region, the GND density is the only relevant quantity whose distribution is not uniform inside a region. This assumption is necessary since only a *gradient* in GND density induces a back stress, but also physically more sound than a uniform GND density.

Finally, Figure 2-5 also shows that the two interface regions on either side of a matrix or precipitate region behave identically, both in terms of plastic deformation and in terms of GND density gradients (which determine the back stress). This motivates the reduction of the number of interface regions in the model that was mentioned in section 2.2.1.

2.4.3 Model summary

The complete model as described in sections 2.2, 2.3 and 2.4 is summarized in Table 2-3.

Table 2-3 Overview of model equations

unit cell region(s)		
Equilibrium		
Strain averaging	all	$\sum_i f^i \boldsymbol{\varepsilon}_{tot}^i = \boldsymbol{\varepsilon}_{tot}$
Sachs interaction	$\gamma', \gamma_1, \gamma_2, \gamma_3$	$\boldsymbol{\sigma}^{\gamma'} = \boldsymbol{\sigma}^{\gamma_1} = \boldsymbol{\sigma}^{\gamma_2} = \boldsymbol{\sigma}^{\gamma_3} = \boldsymbol{\sigma}_{tot}$
Modified Sachs interaction	$I_1^p, I_1^m, I_2^p, I_2^m, I_3^p, I_3^m$	$f^{I_k^p} \boldsymbol{\sigma}^{I_k^p} + f^{I_k^m} \boldsymbol{\sigma}^{I_k^m} = (f^{I_k^p} + f^{I_k^m}) \boldsymbol{\sigma}_{tot}$
Strain compatibility	$I_1^p, I_1^m, I_2^p, I_2^m, I_3^p, I_3^m$	$\boldsymbol{\varepsilon}^{I_k^p} \cdot (\mathbf{I} - \vec{n}^k \vec{n}^k) = \boldsymbol{\varepsilon}^{I_k^m} \cdot (\mathbf{I} - \vec{n}^k \vec{n}^k)$
Traction continuity	$I_1^p, I_1^m, I_2^p, I_2^m, I_3^p, I_3^m$	$\boldsymbol{\sigma}^{I_k^p} \cdot \vec{n}^k = \boldsymbol{\sigma}^{I_k^m} \cdot \vec{n}^k$
Constitutive model	all	$\boldsymbol{\varepsilon}^i \rightarrow \text{constitutive box} \rightarrow \boldsymbol{\sigma}^i$

Table 2-3 (continued)

Internal stresses		
Misfit	<i>all</i>	$\boldsymbol{\sigma}_{misfit}^i = {}^4\mathbf{B}_{misfit}^i : \boldsymbol{\varepsilon}_{misfit}^i$ $\boldsymbol{\sigma}_b = -(\boldsymbol{\sigma}_e^{int} + \boldsymbol{\sigma}_s^{int})$
Back stress	$I_1^p, I_1^m, I_2^p,$ I_2^m, I_3^p, I_3^m	$\boldsymbol{\sigma}_e^{int} = \frac{\mu b R^2}{8(1-\nu)} \sum_{\xi=1}^{12} \bar{\nabla} \rho_{GND}^{\xi} \cdot \begin{pmatrix} 3\bar{n}^{\xi} \bar{s}^{\xi} \bar{s}^{\xi} - \bar{s}^{\xi} \bar{s}^{\xi} \bar{n}^{\xi} \\ -\bar{s}^{\xi} \bar{n}^{\xi} \bar{s}^{\xi} + \bar{n}^{\xi} \bar{n}^{\xi} \bar{n}^{\xi} + 4\nu \bar{n}^{\xi} \bar{p}^{\xi} \bar{p}^{\xi} \end{pmatrix}$ $\boldsymbol{\sigma}_s^{int} = \frac{\mu b R^2}{4} \sum_{\xi=13}^{18} \bar{\nabla} \rho_{GND}^{\xi} \cdot \begin{pmatrix} -\bar{n}^{\xi} \bar{s}^{\xi} \bar{p}^{\xi} - \bar{n}^{\xi} \bar{p}^{\xi} \bar{s}^{\xi} \\ + \bar{p}^{\xi} \bar{s}^{\xi} \bar{n}^{\xi} + \bar{p}^{\xi} \bar{n}^{\xi} \bar{s}^{\xi} \end{pmatrix}$
Matrix constitutive model		
Effective stress	$\gamma_1, \gamma_2, \gamma_3,$ I_1^m, I_2^m, I_3^m	$\boldsymbol{\sigma}_{eff} = \boldsymbol{\sigma} + \boldsymbol{\sigma}_{misfit} - \boldsymbol{\sigma}_b$
Slip rate	$\gamma_1, \gamma_2, \gamma_3,$ I_1^m, I_2^m, I_3^m	$\dot{\gamma}^{\alpha} = \dot{\gamma}_0 \left\{ \frac{ \tau_{eff}^{\alpha} }{s^{\alpha}} \right\}^m \left\{ 1 - \exp\left(-\frac{ \tau_{eff}^{\alpha} }{\tau^{or}}\right) \right\}^n \text{sign}(\tau_{eff}^{\alpha})$
Slip resistance	$\gamma_1, \gamma_2, \gamma_3,$ I_1^m, I_2^m, I_3^m	$s^{\alpha} = \left\{ c\mu b \sqrt{ \rho_{SSD}^{\alpha} + \rho_{GND}^{\alpha} } + C_{soft} \left(1 - \sqrt{\frac{\rho_{SSD}^{\alpha}}{\tilde{\rho}_{SSD}^{\alpha}}} \right)^p \right\} \exp\left[\frac{Q}{kT}\right]$
Precipitate constitutive model		
	$\gamma', I_1^p, I_2^p, I_3^p$	<i>no plastic slip, purely elastic</i>
Dislocation densities		
GND densities	$I_1^p, I_1^m, I_2^p,$ I_2^m, I_3^p, I_3^m	$\rho_{GND}^{\xi} = \rho_{GND,0}^{\xi} - \frac{1}{b} \bar{\nabla} \gamma^{\xi} \cdot \bar{s}^{\xi} \quad (\text{edge dislocations})$ $\rho_{GND}^{\xi} = \rho_{GND,0}^{\xi} + \frac{1}{b} (\bar{\nabla} \gamma^{\alpha_1} \cdot \bar{p}^{\alpha_1} + \bar{\nabla} \gamma^{\alpha_2} \cdot \bar{p}^{\alpha_2}) \quad (\text{screw})$
SSD evolution	$\gamma_1, \gamma_2, \gamma_3,$ I_1^m, I_2^m, I_3^m	$\dot{\rho}_{SSD}^{\alpha} = \frac{1}{b} \left(\frac{1}{L^{\alpha}} - 2\gamma_c \rho_{SSD}^{\alpha} \right) \dot{\gamma}^{\alpha} $

2.5 Application

The framework described in the previous sections has been applied to the single crystal Ni-base superalloy CMSX-4 to demonstrate the effect of strain gradients on the mechanical response. First, the determination of the model parameters is discussed and simulated tensile and creep curves are compared to experimental results. Then, the contributions of the Orowan threshold and the strain gradient induced back stresses to the observed size effects are demonstrated and the simulated size effects due to a change in the microstructural dimensions are compared to experimental results.

Finally, a real multiscale analysis is performed, showing the effect of a change in microstructural dimensions on the creep strain accumulation in a gas turbine blade.

Table 2-4 Model parameters for the matrix phase of CMSX-4.

Model parameter	Symbol	Value	Unit	Used in equation
Reference slip rate	$\dot{\gamma}_0$	$6.5 \cdot 10^{-10}$	s ⁻¹	(2.7)
Rate sensitivity exponent	n	4		(2.7)
Orowan threshold				
Rate sensitivity exponent slip resistance	m	11.7		(2.7)
Reference activation energy	Q	$3.62 \cdot 10^{-20}$	J	(2.12)
Strength parameter	c	0.034		(2.13)
Shear modulus	μ	100.2	GPa	(2.13)
Burgers vector length	b	0.254	nm	(2.11), (2.13), (2.14)
Parameter in Orowan stress	α	0.85		(2.11)
Critical annihilation length	γ_c	7.2	nm	(2.14)
Initial SSD density	$\rho_{SSD,o}$	$5.0 \cdot 10^{13}$	m ⁻²	(2.14)
Material constant	K	7		(2.15)
Softening constant	C_{soft}	90	MPa	(2.16)
Softening exponent	p	0.7		(2.16)
Radius of dislocation influence region	R	8.3	nm	(2.24), (2.25)

The lattice constants of the γ and γ' -phase at 850 °C are 0.3590 nm and 0.3586 nm respectively, which leads to an unconstrained misfit δ equal to $-1.1 \cdot 10^{-3}$, see equation (2.18). The model parameters used for CMSX-4 are given in Table 2-4. The parameters α , k , b and μ are physical quantities with a fixed value, obtained from [27,22]. The matrix phase parameters $\dot{\gamma}_0$ and m in the slip law, equation (2.7), and c , γ_c , $\rho_{SSD,o}$, K , C_{soft} , Q and p in relations (2.12) to (2.17) for the slip resistance and the SSD density evolution, determine the mechanical behaviour for a fixed microstructure. Their values were obtained by calibrating the model to the experimental results [56] shown in Figure 2-6, using a least-squares fitting method. The parameters n and R and the relative width of the matrix phase interface layer determine the material size dependence. The value of n determines the relative strength of the Orowan threshold and the radius of the dislocation influence region R quantifies the magnitude of the back stress. The values for R and n were obtained by fitting the model to the two endpoints (only two points) of the experimentally determined size dependence curve in Figure 2-12, using a

least-squares fitting method. The obtained value for the radius of the dislocation influence region R is significantly smaller than the rather large value of $3.16 \mu\text{m}$ that Evers et al. [38] obtained by fitting their model to results on pure copper. The value used here is more realistic for the present application, since it is in the same order as the dimensions of the matrix phase. Moreover, several studies [57-59] recently showed that R should be in the order of the dislocation spacing, which is equivalent to the inverse square root of the dislocation density. In our model, dislocation densities develop from an initial value of $5 \cdot 10^{13}$ to values up to 10^{16} m^{-2} , which corresponds to R -values ranging from 30 to 140 nm. This is in the same order of magnitude as the resulting value for R .

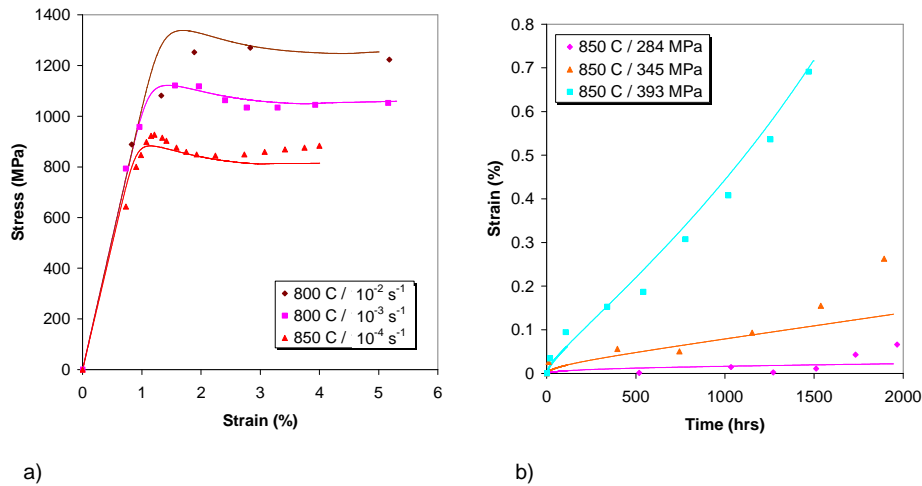
The width of the precipitate part of the interface layer does not affect the size dependence, because no plastic deformation occurs in the precipitate. Therefore this width can be chosen freely in between some limits, e.g. a physically acceptable fraction of the precipitate size. Increasing the width of the matrix interface layer decreases the slip gradients and the resulting back stress and therefore diminishes the size dependence. But on the other hand it increases the volume fraction of the interface regions, which results in stronger size effects. An interfacial width of 30 % of the matrix phase width proved to yield the best compromise between these two counteracting phenomena. This means that the interface effects are acting in a boundary zone with a characteristic size of 19% of the total channel width, located on each side of the channel. This is very close to the value of 23 % presented by Busso et al. [24] for the normalized channel width that contains the strain gradients in their FE unit cell analysis.

2.5.1 Simulation results

In this subsection the model capabilities are demonstrated by comparing simulated tensile and creep curves to experimental results. The model has been implemented in a finite element (FE) code. Tensile tests at 800 and 850 °C at strain rates of 10^{-4} , 10^{-3} and 10^{-2} s^{-1} and creep tests at 850 °C and 284, 345 and 393 MPa are simulated by using an FE model with only a single element. The results are shown in Figure 2-6, together with experimental results for CMSX-4 [56].

The results in Figure 2-6 demonstrate that the present framework is able to simulate the real material response adequately. For the tensile curves, especially the steady-state stress levels correspond well to the experimental values, whereas the deviations are somewhat larger at the initial yielding stage of the curves. This is due to the use of the phenomenological description of the softening behaviour. The simulated

creep curves describe the material behaviour quite well for the primary and secondary creep regime. The tertiary regime is associated with precipitate shearing and microstructural degradation. Since these mechanisms are not included in the present framework, the model is not able to accurately simulate the material response for this part of the creep curve.



a) b)
Figure 2-6 Simulated curves (solid lines) compared to experimental results (markers) for CMSX-4; a) stress-strain curves at strain rates of 10^{-4} s^{-1} at 850 °C and 10^{-3} and 10^{-2} s^{-1} at 800 °C; b) creep curves at 284, 345 and 393 MPa at 850 °C.

To demonstrate the contributions of the individual unit cell regions to the macroscopic response, the evolution of the effective stresses and plastic strains on the micro-level during one of the tensile tests in Figure 2-6 is plotted in Figure 2-7 and Figure 2-8.

Figure 2-7a shows that the regions have different starting values, which is caused by the misfit stress. In the precipitate (both bulk and interface) regions the tensile misfit stress increases the effective stress, while the compressive misfit stress in the matrix regions parallel to the applied load decreases the effective stress. As the misfit stresses only occur in the plane of the γ/γ' -interface, they do not affect the stresses in the load direction in the regions that are normal to the applied load.

The figure also shows that the misfit stresses quickly disappear as soon as the plastic deformation starts. After that, the stresses in all bulk regions equal the macroscopic stress, as is required by the Sachs interaction law. Also, the average value of the matrix and precipitate interface regions equals the macroscopic stress, but the strain gradient related back stresses cause a large difference between the two sides

(matrix and precipitate) of the interface regions, especially for the regions parallel to the applied load. Finally, the results for the bulk and interface unit cell *regions* in Figure 2-7a are used to calculate the volume averaged values for the different *phases* (matrix and precipitate) in the material, as is shown in Figure 2-7b.

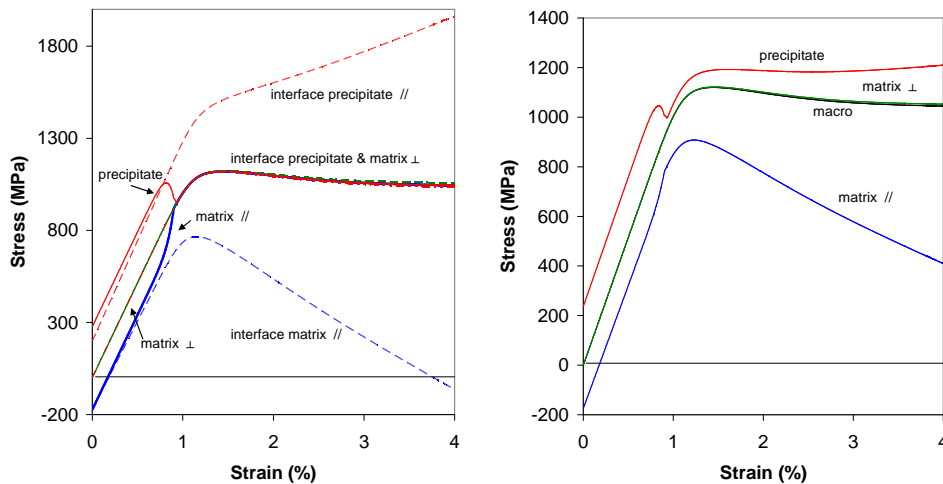


Figure 2-7 Variation of micro-level effective stresses during a tensile test at 800 °C and a strain rate of 10^{-3} s^{-1} . a) stresses in individual unit cell regions; b) stresses in material phases, obtained from combining the results in a), compared to the macroscopic (unit cell averaged) stress. In all cases the stress component in the direction of the applied load is plotted. The symbols \perp and $//$ denote the regions oriented normal and parallel to the applied load, respectively.

Figure 2-8 shows the evolution of plastic strain in the different regions. There is a difference in plastic deformation rate between the matrix bulk regions parallel and normal to the applied load. This is caused by the different (initial) stress levels and the resulting differences in evolution rate of the slip resistance. The plastic flow in the interface regions is limited due to the development of strain gradient related back stresses that reduce the effective stress. The precipitate bulk and interface regions are absent in this figure, since they only deform elastically.

Finally, the evolution of the dislocation densities is illustrated in Figure 2-9, which compares the SSD and GND densities on a specific slip system in both bulk and interface regions at three stages during a tensile test. This shows that in the bulk regions, where no GNDs are present, the SSD density increases with a factor two during the test. In the interface regions strain gradients develop, which are accommodated by a rapidly increasing GND density. The resulting back stresses reduce

the effective stress and therefore lower the slip rate. Consequently, the SSD density hardly increases in these regions.

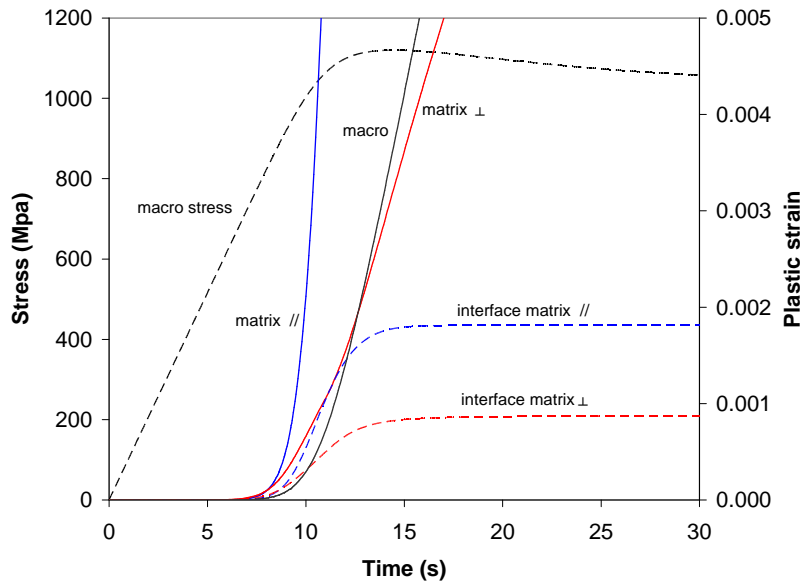


Figure 2-8 Plastic strain evolution in the unit cell regions during a tensile test at 800 °C and a strain rate of 10^{-3} s^{-1} . The strain component in the direction of the applied load is plotted. The macroscopic (unit cell averaged) stress and strain are plotted as a reference.

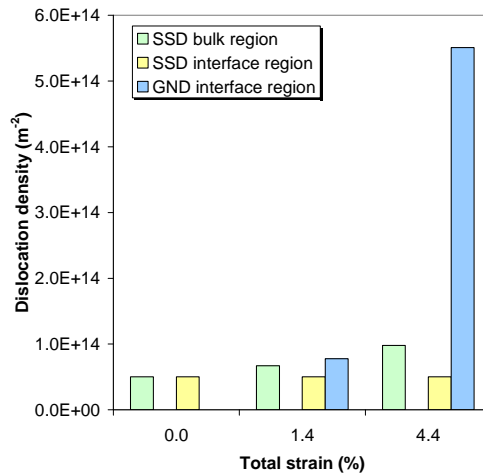


Figure 2-9 Evolution of the SSD and GND densities during a tensile test at 800 °C and a strain rate of 10^{-3} s^{-1} . Values are given for a bulk matrix region and an interface region at three stages of the tensile test.

2.5.2 Strain gradient effects and size dependence

Nickel-base superalloys show a clear size dependence, which means that the mechanical behaviour changes when proportionally increasing or decreasing the microstructural dimensions while keeping all volume fractions constant. The present framework is able to simulate these microstructural size effects.

There are two essential contributions that make the model response size dependent. Firstly, the Orowan threshold stress is size dependent, since it is inversely proportional to the γ -channel width h . Secondly, the GND density is size dependent, because it is related to strain gradients. Reducing the microstructural dimensions will increase the strain gradients and consequently the GND densities. GND densities in their turn contribute to the slip resistance and, through their gradients, govern the back stress. The Orowan threshold is incorporated in several existing superalloy models [22,23,28,29,30], whereas only strain gradient effects are present in the two FE unit cell approaches [24,25,26] discussed before. This section will demonstrate the necessity and possibility of including both ingredients in superalloy constitutive models.

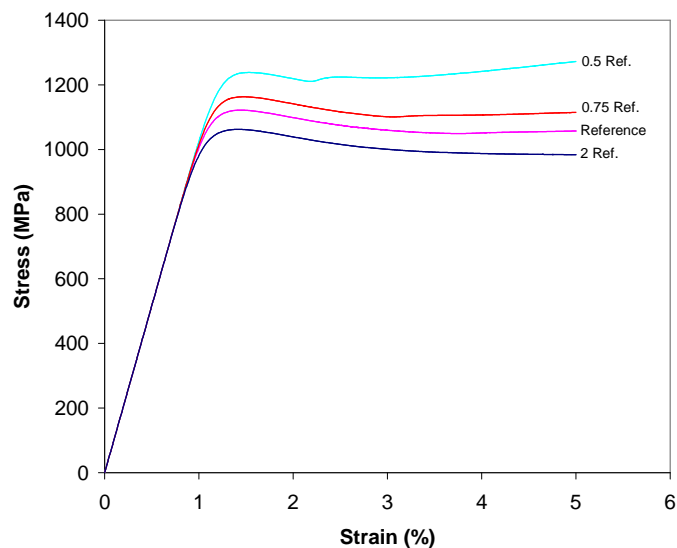


Figure 2-10 Effect of changing microstructural dimensions on the stress-strain curve at a strain rate of 10^{-3} s^{-1} , including the effect of Geometrically Necessary Dislocations and resulting back stresses. The reference case is $L = 500 \text{ nm}$ and $h = 60 \text{ nm}$.

The model parameters from Table 2-4 lead to an initial slip resistance ($s^{\alpha} = 98 \text{ MPa}$) which is lower than the Orowan stress ($\tau^{or} = 255 \text{ MPa}$). This means that the Orowan threshold is the decisive threshold in this case. Downsizing the complete unit cell by a

factor 2 or 4 increases the Orowan threshold by the same factor. The GND densities in the interface regions are proportional to the gradients in the plastic slip. Changing the interfacial width by increasing or decreasing the unit cell dimensions affects the gradients and hence the GND densities. Consequently, the material response changes since the GNDs contribute to the slip resistance and constitute the source of back stresses.

The unit cell dimensions were varied to quantify these size effects. Figure 2-10 shows the stress-strain curves at a rate of 10^{-3} s^{-1} for the reference case, for which the microstructural dimensions used are $L = 500 \text{ nm}$ and $h = 60 \text{ nm}$, and for three other cases with all unit cell dimensions multiplied by a factor 0.5, 0.75 and 2. In these simulations both the Orowan effect and the GND effects are included.

To separate the effects of GNDs and the Orowan threshold, the internal stresses were removed from the model by setting all GND densities to zero. The resulting stress-strain curves are shown in Figure 2-11 for the reference case and for three other unit cell sizes, where the observed effects are now due to the change of the Orowan threshold only. This figure shows that the shape of the curves for the different unit cell sizes remains the same, while the maximum stress again shifts to a higher level with a decreasing matrix channel width.

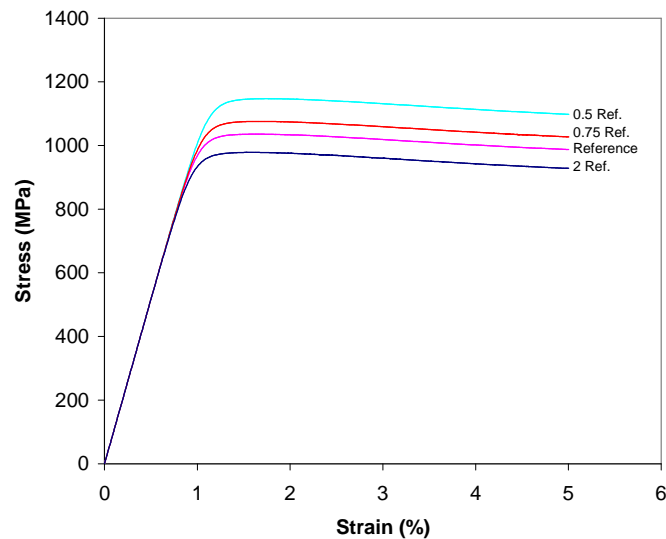


Figure 2-11 Effect of changing microstructural dimensions on the stress-strain curve, using the model without Geometrically Necessary Dislocations. The reference case is $L = 500 \text{ nm}$ and $h = 60 \text{ nm}$.

Comparison of the curves in Figure 2-10 and Figure 2-11 shows that their shape is identical for small strains ($< 1.3\%$), but quite different for larger strains. Also, the yield points for the curves in Figure 2-10 are higher than those in Figure 2-11. The increased slip resistance and back stresses that develop due to increasing internal strain gradients reduce the slip rates. Hence the material stress response is increasing. This effect is stronger when the microstructural dimensions decrease below the values of the reference case, i.e. smaller is stronger.

Finally, the simulated size effects were compared to experimental results (Figure 2-12). Duhl [60] measured the change of the steady-state flow stress at different precipitate sizes for PWA1480, a similar nickel-base superalloy with a high precipitate volume fraction. The steady-state flow stresses were normalised by the values for the reference cases to enable a direct comparison in Figure 2-12. Although the experimental results were determined at $760\text{ }^{\circ}\text{C}$ and the present model was calibrated for $800\text{ }^{\circ}\text{C}$, the observed size effect could be simulated quite well. In the simulations, the steady-state flow stress was defined as the stress level at the end of the curve (at 5% total strain). During the deformation, the slip resistance and back stress evolve until the plastic strain rate equals the externally applied strain rate. From that point on the stress has attained a steady-state value. In the majority of the simulations this point was reached before a strain level of 5% .

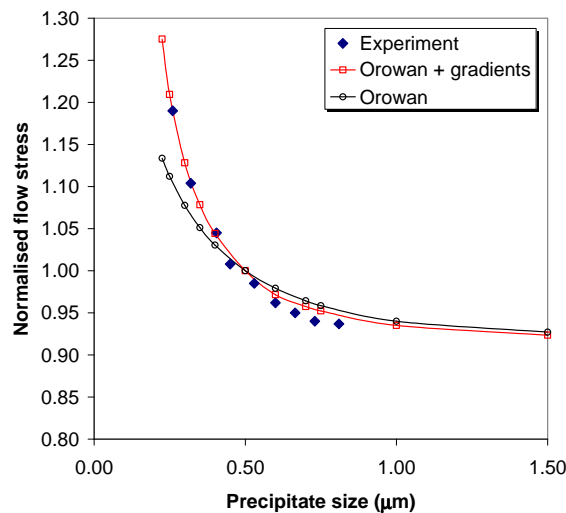


Figure 2-12 Simulated effect of changing microstructural dimensions on the steady-state flow stress for CMSX-4 at $800\text{ }^{\circ}\text{C}$. Results for simulations with Orowan effect only and with Orowan + strain gradient effects. Experimental data for PWA1480 at $760\text{ }^{\circ}\text{C}$ obtained from [60].

Figure 2-12 also shows the simulated size dependence for the model without strain gradient effects, where the Orowan threshold is the only cause of size effects. For large microstructural dimensions, the curve is almost identical to the strain gradient curve, but for small dimensions there is a significant difference. At these dimensions the plastic strain gradients play an important role and the material size dependence cannot be described by the Orowan effect only.

Busso et al. [24] performed the same simulations with their gradient-dependent unit cell finite element model, consisting of about 500 finite elements. The present model with only 10 unit cell regions predicts the size effects at least as good as the model by Busso et al. [24], but with a considerably lower computational effort.

2.5.3 Computational efficiency and multiscale analysis

The present framework is developed specifically to be used in a multiscale analysis on real gas turbine components. Therefore, it is essential that the model is computationally efficient. This efficiency is largely determined by the model's level of detail and the associated number of internal variables. Even though a direct comparison between different modelling approaches in terms of computational efficiency is difficult (in view of the many small or large differences in model capabilities and assumptions), an attempt is made in Table 2-5.

The left-hand side of the table provides information about the model characteristics and capabilities, also classified by one or two + or – signs. In the right-hand side of the table the computational efficiency is quantified. The first column provides the number of degrees of freedom (d.o.f.) to be solved to obtain the local stress distribution for a given plastic strain distribution. For the analytical models this is the number of equations, for the FE models three (nodal d.o.f.) times the number of nodes, both for one material point.

Then the number of internal variables per material point is specified and the time integration method is mentioned. For the present model, the time integration is fully explicit, both on the local (unit cell) and global (macro) level. Finally, the overall computational efficiency is classified by one or two + or – signs.

Table 2-5 shows that the different approaches can be classified in three groups: traditional single phase models, analytical unit cell models and finite element unit cell models, requiring small, medium and very large computational effort, respectively. Within the groups the computational effort is comparable, but the level of detail and model capabilities differ considerably. The present modelling approach can be considered as the most extensive method amongst the analytical unit cell models, where it is the only model including strain gradient effects.

Table 2-5 Comparison of different modelling approaches.

Author(s)	Characteristics / level of detail / capabilities	Computational efficiency				
		# d.o.f.	# int. vars	time integr.		
Traditional models	- single phase model - no microstructural details	- -	3 - 6	0	+	+
Svoboda and Lukas [30]	- 4 regions unit cell - analytic stress calculation - dislocation based creep law in γ / γ' - for $\langle 001 \rangle$ only - isotropic elastic properties	-	24	54	not specified	+
Fedelich [23]	- 8 regions unit cell - Fourier series approach for stress calculation - dislocation based plasticity in γ / γ'	+	24, using 216 structural tensor (Ω_{kl}) components	192	Runge-Kutta	+
Tinga et al. (present model)	- 10 regions unit cell - analytic stress calculation - dislocation based <i>strain gradient</i> plasticity in $\gamma /$ elastic precipitate	+	60	216	fully explicit	+
Kuttner and Wahi [29]	- 125 elm FE model - Norton creep law for γ/γ'	+	~ 1000	0	not specified	-
Busso et al. [24]	- 424 elm FE model - dislocation based <i>strain gradient</i> plasticity in $\gamma /$ elastic precipitate	+	~ 4000	$\sim 10^5$	fully implicit	-
Choi et al. [26]	- 424 elm FE model - phenomenological <i>strain gradient</i> plasticity in $\gamma /$ elastic precipitate	+	~ 4000	$\sim 10^5$	combined explicit / implicit	-

To clearly emphasize the computational efficiency of the present framework and to demonstrate the multiscale capabilities, the proposed multiscale model was applied to a finite element model of an aero-engine low pressure turbine blade discretized with 5668 hexagonal (8-noded) elements and 7302 nodes.

The proposed unit cell model was implemented in a user-subroutine of the commercial finite element code MSC.Marc. During the analysis, it is solved for each

integration point in the turbine blade model. A short-term creep analysis, divided into 32 time steps, was performed in only half an hour on a desktop PC. The temperature and stress distribution used in the creep analysis are shown in Figure 2-13 a and b respectively. Then the creep strain accumulation in a component with a reference microstructure ($L = 500 \text{ nm}$, $h = 60 \text{ nm}$) can be compared to the accumulation in a blade with a coarsened microstructure ($L = 1000 \text{ nm}$, $h = 120 \text{ nm}$). The results are shown in Figure 2-13 c and d.

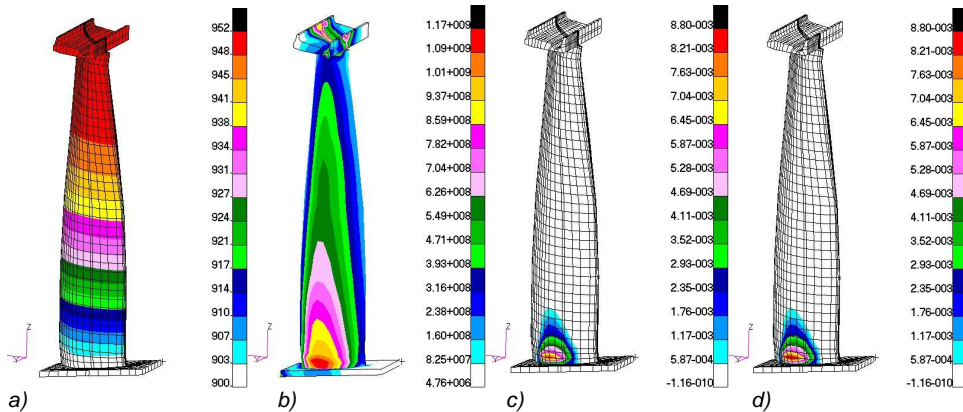


Figure 2-13 Finite element analysis results on a gas turbine blade. a) temperature distribution, b) equivalent stress distribution, c) accumulated creep strain for reference microstructure, d) accumulated creep strain for coarsened microstructure.

The evolution of the creep strain in time is plotted in Figure 2-14, which shows that the creep strain rate in the component with the coarsened microstructure is considerably higher than in the blade with the reference microstructure.

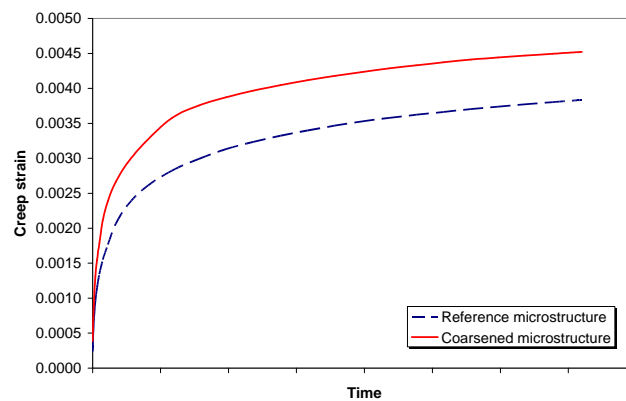


Figure 2-14 Creep strain accumulation in time for a reference and a coarsened microstructure.

This analysis clearly demonstrates that the proposed framework can be used efficiently in a multiscale approach. And it also reveals the relevance, for the engineering practice, of including strain-gradient effects in superalloy mechanical models.

2.6 Conclusions

Strain gradient effects are incorporated in a newly developed efficient crystal plasticity framework for nickel-base superalloys with the following innovative characteristics:

- The proposed unit cell contains special interface regions, in which the plastic strain gradients are located. In these interface regions strain gradient induced back stresses will develop as well as stresses due to the lattice misfit between the two phases.
- The limited size of the unit cell and the micromechanical simplifications, which condense the governing equations to 10 uniformly deforming regions, make the framework particularly efficient in a multiscale approach. The unit cell response is determined numerically on a material point level within a macroscopic FE code, which is computationally much more efficient than a detailed FE-based unit cell discretization.
- The material constitutive behaviour is simulated by using an extension of an existing non-local strain gradient crystal plasticity model for the matrix material. In this model, non-uniform distributions of geometrically necessary dislocations (GNDs), induced by strain gradients in the interface regions, affect the hardening behaviour. Further, the model has been modified here for the present two-phase material by adding a threshold term related to the Orowan stress to the hardening law. Continuous dislocation densities and slip gradients, as typically used in the FE formulation, are approximated here by piecewise uniform fields for application in an efficient unit cell approach.

The model was applied to the Ni-base superalloy CMSX-4, where it proved to be capable of accurately simulating the experimentally observed change of the steady-state flow stress with varying microstructural dimensions. Further, the multiscale capability was demonstrated by applying the model in a gas turbine blade finite element analysis. Therefore, it can be concluded that the proposed framework is able to describe the material response and size effects to a level of detail similar to complex FE unit cell models, while being computationally much more efficient.

Chapter 3

Cube slip and precipitate phase constitutive model²

Abstract - An advanced constitutive model incorporating two specific aspects of Ni-base superalloy deformation behaviour is proposed. Several deformation mechanisms are active in these two-phase materials. In the matrix phase, cube slip plays an important role in the orientation dependence of the material. Moreover, inelastic deformation of the precipitate phase leads to non-Schmid effects in the material response. Cube slip is modelled here by incorporating a zig-zag cross slip mechanism into the constitutive relations for the matrix phase. A cross slip factor is proposed that quantifies the amount of cross slip and consequently represents the orientation dependence of the cube slip. Further, a detailed precipitate phase constitutive model is proposed, which enables the simulation of the anomalous yield behaviour and other non-Schmid effects, like the tension-compression asymmetry. The cross slip mechanism and the associated splitting of partial dislocations in the γ' -phase, that are responsible for the anomalous yield behaviour, are incorporated in the model. The proposed formulations are implemented in a recently developed crystal plasticity framework for single crystal Ni-base superalloys and a consistent set of model parameters for the commercial alloy CMSX-4 is determined. The model is shown to reasonably predict the material tensile response and creep behaviour for a range of temperatures and stress or strain rate levels. The incorporation of the cross slip mechanisms in the matrix and precipitate results in an adequate simulation of the material orientation dependence and the experimentally determined tension-compression asymmetry.

3.1 Introduction

The superior high temperature behaviour of single crystal nickel-base superalloys is attributed to their characteristic two-phase composite microstructure. This microstructure consists of a γ -matrix containing a large volume fraction of γ' -particles

² This chapter is based on: Tinga, T., Brekelmans, W. A. M. and Geers, M. G. D.; *Cube slip and non-Schmid effects in single crystal nickel-base superalloys*; Modelling and Simulation in Materials Science and Engineering, submitted (2009), 1-30.

(see Figure 1-3). The Ni_3Al (γ') -precipitates are cuboidal and are more or less regularly distributed in a Ni-matrix (γ -phase). The typical precipitate size is $0.5\ \mu\text{m}$ while the matrix channel width is typically $60\ \text{nm}$. The high resistance of the superalloy against inelastic deformation at elevated temperatures makes it very suitable for use as gas turbine blade material.

The design process of gas turbine components, but also the maintenance and overhaul activities, require a reliable prediction of the thermo-mechanical characteristics of the used materials. Therefore, modelling of the mechanical behaviour of superalloys has been subject of numerous studies. Initially the material was treated as a homogeneous single phase material [2-12,61]. Since these approaches are addressing the macroscopic level, they can easily be used as a constitutive description in a finite element (FE) analysis, which is nowadays the common method used for component stress analysis and life time assessment. More recently, models were developed that take into account the two-phase nature of superalloys. In these microstructural models the shape, dimensions and properties of both phases are considered as model parameters. However, the length scale of the microstructure, which is in the order of micrometers, is much smaller than the engineering length scale. Modelling an entire macroscopic component taking into account all microstructural details is therefore not feasible in the engineering practice.

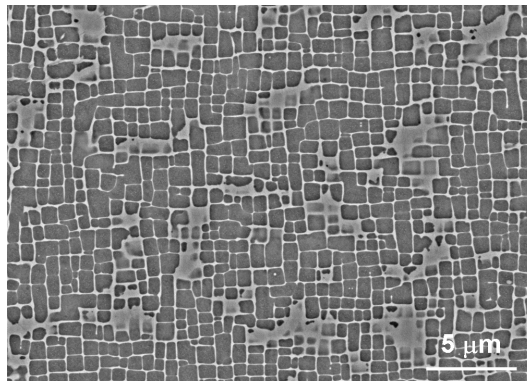


Figure 3-1 Micrograph of a superalloy microstructure showing the cuboidal γ' -precipitates in a γ -matrix [36].

One way to cover this difference in length scales is the use of a multiscale approach in which an appropriate homogenization method is applied to connect the microscopic to the macroscopic level, as was done by Fedelich [22,23]. Another way to overcome the length scale problem is the use of microstructural models that predict the material

response in a closed-form set of equations on the level of a material point only [24-30]. Except for the model by Svoboda and Lukas [28,30], all these approaches use a detailed finite element description of the unit cell. The microstructural results are then used to develop constitutive descriptions which are applicable in traditional methods at the macroscopic level. Clearly, the analyses on the microscopic and the macroscopic level are completely separated in this case.

The existing microstructural models take along two drawbacks. Firstly they require a considerable computational effort, which is particularly the case for the finite element based material point models. And secondly, the majority of the proposed models is only valid for a small range of load conditions (temperature, stress level). However, the life assessment of real gas turbine components requires a computational efficient model that is applicable over a wide range of conditions. Therefore, the authors recently proposed a multiscale framework for nickel-base superalloys [62] that meets these two criteria.

The present paper addresses two aspects of constitutive behaviour that are specific to Ni-base superalloys, namely cube slip in the matrix phase and inelastic deformation of the precipitate phase, leading to non-Schmid effects. Addition of these aspects extends the application range of the previously proposed framework [62] considerably. Moreover, the proposed formulations provide a more general view on the modelling of superalloy constitutive behaviour and may be used in other modelling approaches.

For an FCC lattice usually only 12 octahedral $\{111\}\langle 011 \rangle$ slip systems are considered. However, for superalloys it seems to be inevitable to also include a set of cube $\{001\}\langle 011 \rangle$ slip systems. This is necessary to correctly simulate the experimentally observed response of the material when it is loaded in, for example, a $\langle 111 \rangle$ direction. For this orientation the yield stress is much lower than for the $\langle 001 \rangle$ orientation, although the resolved shear stresses on the activated slip systems in the latter case are lowest. There is, however, much debate whether cube slip physically really happens in the matrix phase of the material, or that it is only a phenomenological description of cross slip processes on the octahedral systems. On the macroscopic level, several researchers, e.g. Méric et al. [63], have shown cube slip traces on $\langle 111 \rangle$ oriented specimens that can be interpreted as *macroscopic* cube slip. Also, on the microscopic level, the sequential cross slip of screw dislocations on two sets of octahedral systems, resulting in zig-zag slip on a macroscopic cube plane, has been observed extensively in the matrix phase of several superalloys [40,64,65]. Actual *microscopic* cube slip has only

been observed occasionally [40,65] in experiments, and seems to be limited to specific conditions.

Knowing that the cross slip mechanism is the major source of macroscopic cube slip, it is surprising to notice that almost all crystal plasticity models for superalloys [3,23,24,63] applied to orientations other than $\langle 001 \rangle$, explicitly include the cube slip systems to describe (macroscopic) cube slip. This is undesirable for two reasons. Firstly, it does not reflect the physical mechanism behind the cube slip, and secondly, it requires the introduction of an additional set of model parameters and a set of dislocation densities for the cube slip systems, which make the model computationally less efficient. Therefore, a formulation is proposed here to include macroscopic cube slip in the model through the behaviour of the octahedral cross slip mechanisms, instead of adding artificial cube slip systems.

Another phenomenon that is often neglected is the inelastic deformation of the precipitate. It is only included in a few superalloy constitutive models. Almost any model treats the precipitate phase as an elastic medium in which no plastic deformation occurs. This means that the mechanisms of recovery climb and precipitate shearing by dislocations are not considered, which limits the applicability of these models at larger plastic strains (0.5 - 2 %, depending on temperature) considerably. However, in gas turbine components local creep strains beyond these values occur, which means that the engineering practice requires a model that can be applied up to higher plastic strains. A few models include, to various levels of detail, the inelastic deformation of the precipitate [23,30]. However, the precipitate anomalous yield behaviour, that will be discussed next, is not included in these models. In the present paper, the computationally efficient framework in [62], which specifically pays attention to strain-gradient based internal stresses at the γ/γ' -interfaces, is extended with a detailed precipitate inelastic constitutive model that includes the anomalous yield behaviour.

From an experimental point of view, a lot of research [11,30,39-47] has been done on the plastic deformation of Ni_3Al intermetallics, both as a separate phase and as a precipitate in superalloys. As a result, the deformation mechanisms in this material are relatively well understood. A moving dislocation in the matrix phase that encounters a precipitate can either cut through the particle or climb around it. Since the intermetallic is an ordered (L1_2) solid solution of Al in Ni, it forms a superlattice with a perfect dislocation which is twice as large as the matrix perfect dislocation. Therefore, on entering the precipitate, a matrix dislocation causes either an anti-phase boundary (APB) or a superlattice intrinsic stacking fault (SISF), depending on the

dislocation dissociation mechanism. It appears that precipitate shearing becomes an important deformation mechanism in superalloys at temperatures above 950 °C and at larger strains (latest stages of steady-state creep). At lower temperatures, considerable stresses in the range of 500 to 600 MPa are required to initiate particle shearing.

Also, the typical anomalous yield behaviour of this intermetallic has been subject of research [66-69]. Contrary to what is commonly observed in metals, the yield stress increases with temperature up to a peak temperature, $T_p \approx 500 - 900$ °C, and then steadily decreases. Moreover, the material response depends on the sense of the applied stress, resulting in a tension-compression asymmetry. The extended crystal plasticity theory by Qin and Bassani [67] can be used to model these effects. However, in almost any superalloy constitutive model this non-Schmid behaviour is neglected. One exception is the rather simple constitutive model by Allan [70], which is specifically developed to describe these effects, but is considerably limited in other aspects.

In summary, the present paper proposes an original formulation to include macroscopic cube slip in the matrix phase constitutive behaviour, by incorporating the octahedral cross slip mechanism. A constitutive model for the precipitate phase is developed, for which existing formulations for both the precipitate shearing and climb mechanisms are evaluated, combined and extended to form an adequate characterization. Using this formulation, the Ni₃Al anomalous yield behaviour is included in a comprehensive superalloy constitutive model for the first time.

In the next section the previously proposed [62] multiscale framework is briefly summarized. In section 3.3 the cross slip processes that lead to macroscopic cube slip are discussed in detail and a formulation is proposed to include the cross slip in the matrix phase constitutive model. Section 3.4 focuses on the new precipitate constitutive model that is proposed by describing the different deformation mechanisms and defining formulations to model the mechanical response. Also, the role of the Ni₃Al anomalous yield behaviour is discussed. In section 3.5, the model parameters are determined by fitting the model to experimental results on the Ni-base superalloy CMSX-4. In section 3.6 the model capabilities are demonstrated by comparing simulated macroscopic tensile and creep curves to experimental results for a range of temperatures, stresses and strain rates. Also, the orientation dependence governed by cube slip and the effect of the precipitate anomalous yield behaviour on the alloy mechanical response are illustrated. Finally, section 3.7 forwards some concluding remarks.

3.2 Multiscale framework

In this section the previously proposed multiscale framework is summarized. For a detailed description and background the reader is referred to chapter 2 [62]. First, the different length scales are illustrated and the mesoscopic unit cell is defined. Then the strain-gradient crystal plasticity theory used to model the constitutive behaviour of the two phases is briefly discussed. Finally, the internal stresses that develop inside the unit cell are described.

3.2.1 Unit cell description

The different length scales covered by the model are shown schematically in Figure 2-2a. The *macroscopic* length scale characterises the engineering level on which a finite element (FE) model is commonly used to solve the governing equilibrium problem. The *mesoscopic* length scale represents the scale of the microstructure at the level of a macroscopic material point. At this length scale the material is considered as a compound of two different phases: γ' -precipitates embedded in a γ -matrix.

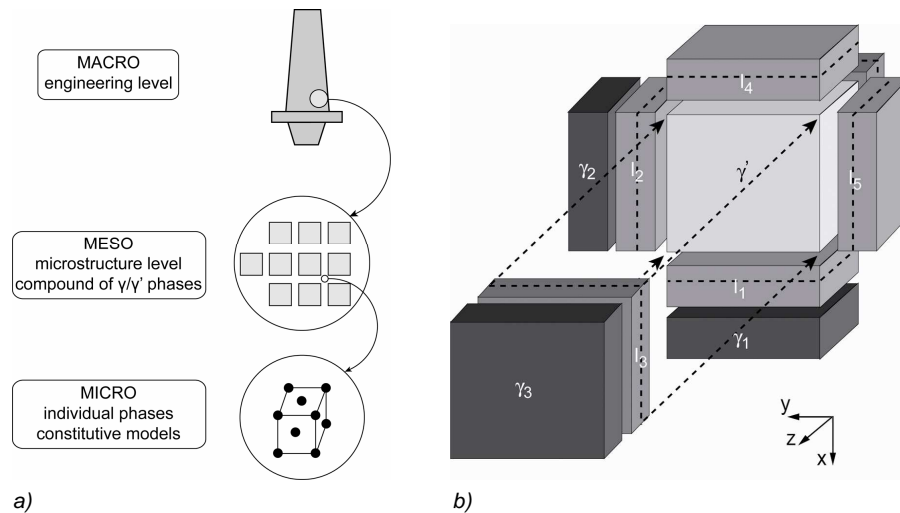


Figure 3-2 Schematic overview of the model, showing (a) the multiscale character and (b) the multi-phase unit cell, consisting of one precipitate (γ'), three matrix (γ_i) and six double interface (I_i) regions.

Finally, the *microscopic* length scale reflects the crystallographic nature of the individual material phases. The constitutive behaviour is defined on this level using a crystal plasticity framework.

On the material point level the Ni-base superalloy microstructure, consisting of γ' -precipitates in a γ -matrix, is represented by a unit cell containing 16 regions (see Figure 2-2b):

- 1 γ' -precipitate region,
- 3 γ -matrix channel regions ($\gamma_j, j = 1 \dots 3$) with different orientations (normal along the $[001]$, $[010]$ and $[100]$ direction),
- 12 interface regions (I_k^m and $I_k^p, k = 1 \dots 6$) containing the γ/γ' -interfaces. A matrix and a precipitate region together form a bi-crystal, which is located on each face of the γ' -precipitate.

The bi-crystal regions take into account the processes that take place at the γ/γ' -interfaces.

3.2.2 Strain-gradient crystal plasticity

A strain-gradient enhanced crystal plasticity approach [37] is used to model the constitutive behaviour of the two phases. In a conventional crystal plasticity framework, the plastic deformation of metals naturally results from the process of crystallographic slip, which is carried by the movement of dislocations. Yet, also the hardening behaviour of metals is attributed to dislocations. Plastic deformation causes multiplication of dislocations and their mutual interaction impedes the motion of gliding dislocations, which causes strengthening. Based on their field characteristics, the total dislocation population can be considered to consist of two parts:

- statistically stored dislocations (SSD),
- geometrically necessary dislocations (GND) [50].

The SSDs are randomly oriented and therefore do not have any directional effect and no net Burgers vector. They accumulate through a statistical process. On the other hand, when a gradient in the plastic deformation occurs in the material, a change of the GND density is required to maintain lattice compatibility. Individual dislocations cannot be distinguished as SSDs or GNDs. The GNDs represent therefore the fraction of the total dislocation population with a non-zero net Burgers vector. A gradient in the GND density causes an internal stress which affects the plastic deformation. These strain-gradient dependent influences give the model a non-local character.

For both phases of the considered superalloy, each with a face-centred cubic (FCC) lattice, 3 slip directions on each of the 4 octahedral slip planes can be identified, resulting in 12 equivalent slip systems. In the present model it is assumed that all SSD densities are of the edge type, whereas for the GNDs both edge and screw dislocations

are considered. This implies that for an FCC metal 12 edge SSD densities are taken into account, next to 12 edge and 6 screw GND densities [50]. A complete overview of all slip systems, including the related orientations that will be used in sections 3.3 and 3.4, is given in Table 3-1. Each screw dislocation can move on either of the two slip planes in which it can reside. This means that, after a certain amount of glide, it can cross slip to the associated slip plane, identified by the fifth column in Table 3-1.

Table 3-1 List of indices and vectors for dislocation densities and slip systems in an FCC metal.

Slip system number and slip direction		Slip plane normal	Shear stress	Associated slip system			Cube plane normal
α_1	\vec{s}^{α_1}	\vec{n}^{α_1}	τ^{pe}	α_2	\vec{n}^{α_2}	τ^e	$\vec{n}_c^{\alpha_1}$
1	$\frac{1}{2}\sqrt{2}$ $[\bar{1}10]$	$\frac{1}{3}\sqrt{3}$ $[111]$	$\frac{1}{6}\sqrt{6}$ $[\bar{1}\bar{1}2]$	10	$\frac{1}{3}\sqrt{3}$ $[11\bar{1}]$	$\frac{1}{6}\sqrt{6}$ $[112]$	$[001]$
2	$\frac{1}{2}\sqrt{2}$ $[10\bar{1}]$	$\frac{1}{3}\sqrt{3}$ $[111]$	$\frac{1}{6}\sqrt{6}$ $[\bar{1}2\bar{1}]$	8	$\frac{1}{3}\sqrt{3}$ $[1\bar{1}1]$	$\frac{1}{6}\sqrt{6}$ $[121]$	$[010]$
3	$\frac{1}{2}\sqrt{2}$ $[0\bar{1}1]$	$\frac{1}{3}\sqrt{3}$ $[111]$	$\frac{1}{6}\sqrt{6}$ $[2\bar{1}\bar{1}]$	6	$\frac{1}{3}\sqrt{3}$ $[\bar{1}11]$	$\frac{1}{6}\sqrt{6}$ $[211]$	$[100]$
4	$\frac{1}{2}\sqrt{2}$ $[\bar{1}\bar{1}0]$	$\frac{1}{3}\sqrt{3}$ $[1\bar{1}\bar{1}]$	$\frac{1}{6}\sqrt{6}$ $[\bar{1}1\bar{2}]$	7	$\frac{1}{3}\sqrt{3}$ $[1\bar{1}1]$	$\frac{1}{6}\sqrt{6}$ $[1\bar{1}2]$	$[00\bar{1}]$
5	$\frac{1}{2}\sqrt{2}$ $[101]$	$\frac{1}{3}\sqrt{3}$ $[1\bar{1}\bar{1}]$	$\frac{1}{6}\sqrt{6}$ $[\bar{1}2\bar{1}]$	11	$\frac{1}{3}\sqrt{3}$ $[11\bar{1}]$	$\frac{1}{6}\sqrt{6}$ $[12\bar{1}]$	$[0\bar{1}0]$
6	$\frac{1}{2}\sqrt{2}$ $[01\bar{1}]$	$\frac{1}{3}\sqrt{3}$ $[1\bar{1}\bar{1}]$	$\frac{1}{6}\sqrt{6}$ $[211]$	3	$\frac{1}{3}\sqrt{3}$ $[\bar{1}\bar{1}\bar{1}]$	$\frac{1}{6}\sqrt{6}$ $[2\bar{1}\bar{1}]$	$[100]$
7	$\frac{1}{2}\sqrt{2}$ $[110]$	$\frac{1}{3}\sqrt{3}$ $[\bar{1}1\bar{1}]$	$\frac{1}{6}\sqrt{6}$ $[1\bar{1}2]$	4	$\frac{1}{3}\sqrt{3}$ $[\bar{1}11]$	$\frac{1}{6}\sqrt{6}$ $[\bar{1}12]$	$[00\bar{1}]$
8	$\frac{1}{2}\sqrt{2}$ $[\bar{1}01]$	$\frac{1}{3}\sqrt{3}$ $[\bar{1}1\bar{1}]$	$\frac{1}{6}\sqrt{6}$ $[121]$	2	$\frac{1}{3}\sqrt{3}$ $[\bar{1}\bar{1}\bar{1}]$	$\frac{1}{6}\sqrt{6}$ $[\bar{1}2\bar{1}]$	$[010]$
9	$\frac{1}{2}\sqrt{2}$ $[0\bar{1}\bar{1}]$	$\frac{1}{3}\sqrt{3}$ $[\bar{1}\bar{1}\bar{1}]$	$\frac{1}{6}\sqrt{6}$ $[\bar{2}1\bar{1}]$	12	$\frac{1}{3}\sqrt{3}$ $[11\bar{1}]$	$\frac{1}{6}\sqrt{6}$ $[\bar{2}1\bar{1}]$	$[\bar{1}00]$
10	$\frac{1}{2}\sqrt{2}$ $[1\bar{1}0]$	$\frac{1}{3}\sqrt{3}$ $[\bar{1}\bar{1}1]$	$\frac{1}{6}\sqrt{6}$ $[112]$	1	$\frac{1}{3}\sqrt{3}$ $[\bar{1}\bar{1}\bar{1}]$	$\frac{1}{6}\sqrt{6}$ $[\bar{1}\bar{1}2]$	$[001]$
11	$\frac{1}{2}\sqrt{2}$ $[\bar{1}0\bar{1}]$	$\frac{1}{3}\sqrt{3}$ $[\bar{1}\bar{1}1]$	$\frac{1}{6}\sqrt{6}$ $[12\bar{1}]$	5	$\frac{1}{3}\sqrt{3}$ $[\bar{1}11]$	$\frac{1}{6}\sqrt{6}$ $[\bar{1}21]$	$[0\bar{1}0]$
12	$\frac{1}{2}\sqrt{2}$ $[011]$	$\frac{1}{3}\sqrt{3}$ $[\bar{1}\bar{1}1]$	$\frac{1}{6}\sqrt{6}$ $[\bar{2}1\bar{1}]$	9	$\frac{1}{3}\sqrt{3}$ $[1\bar{1}1]$	$\frac{1}{6}\sqrt{6}$ $[\bar{2}1\bar{1}]$	$[\bar{1}00]$

Table 3-2 4C elastic tensor components for CMSX-4 at various temperatures [56].

T (°C)	C_{1111} (GPa)	C_{1122} (GPa)	C_{1212} (GPa)
20	273.6	182.4	123.7
550	239.4	159.6	121.3
700	231.4	154.3	117.6
800	223.9	149.3	114.6
850	215.4	143.6	112.1
900	207.6	138.4	111.5
950	204.4	136.3	107.9

The elastic material behaviour is modelled using a standard formulation for orthotropic materials with cubic symmetry. The three independent components of the elastic tensor ${}^4\mathbf{C}$ of both phases in CMSX-4 at 850 °C are given in Table 3-3 [24]. Since no values are available at other temperatures, the temperature dependence of the alloy (Table 3-2 [56]) is used to scale the values for the individual phases.

Table 3-3 ${}^4\mathbf{C}$ elastic tensor components for CMSX-4 phases at 850 °C [24].

	γ -matrix	γ' -precipitate
C_{1111} (GPa)	190.9	216.9
C_{1122} (GPa)	127.3	144.6
C_{1212} (GPa)	100.2	112.9

3.2.3 Internal stresses

The interface between the two different phases plays an important role in the mechanical behaviour of the multi-phase material, because of the development of significant internal stresses that interact with the externally applied stress. In the present model the following internal stresses are incorporated:

- misfit stress: stress that originates from the lattice misfit between the γ - and γ' -phases at the level of the coherent interface that is formed,
- back stress: stress that originates from deformation-induced plastic strain-gradients leading to a gradient in the GND density at the interfaces.

These interface effects are only included in the interface regions of the model. The relations describing these effects can be found in [62].

3.3 Cube slip

As discussed in the introduction, the majority of the superalloy constitutive models contain a set of cube slip systems to correctly simulate the material behaviour at orientations other than $\langle 001 \rangle$, whereas experiments show that the occurrence of macroscopic cube slip is quite exceptional. In this section, the octahedral cross slip processes, that are physically responsible for the major part of the cube slip, are discussed. Then the matrix phase constitutive model used in [62] is briefly summarized and a formulation is proposed to include the octahedral cross slip in this description.

3.3.1 Cross slip mechanism

The zig-zag cross slip mechanism, that causes macroscopic cube slip, has been described in detail by Bettge and Österle [64,65], and is illustrated in Figure 3-3. The

leading edge-type section of a dislocation loop entering a matrix channel glides on an octahedral plane in a direction parallel to the γ/γ' -interfaces. The loop can widen by moving its trailing screw-type sections towards the interfaces. This process is limited by the width of the matrix channel, since the dislocation segments cannot easily move beyond the γ/γ' -interfaces. Therefore, after a certain amount of deformation, a large number of screw-type segments are deposited at the γ/γ' -interfaces. However, under certain conditions, the screw-type segments can cross slip onto another slip system, which enables them to widen the loop further by moving on the cross slip plane. Again, this movement stops when the segment arrives at the opposite interface, but by cross slipping to the original slip plane, further movement is possible. This repeated cross slip produces a zig-zag edge-type segment of the loop, with a length considerably larger than the original length. Gliding of this segment produces significantly more plastic deformation than the original segment. Moreover, it produces a macroscopic deformation that is similar to slip on a cube slip system.

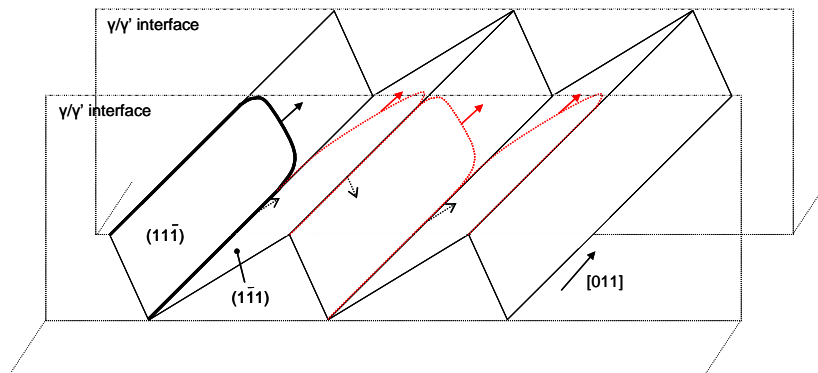


Figure 3-3 Schematic representation of the cross slip process resulting in macroscopic cube slip.

The cross slip process can only occur on specific pairs of slip systems if the orientation of the crystal relative to the applied load is such that the resolved shear stress is in the same direction on both of the two associated slip planes [65]. Regarding the first requirement, cross slip can only occur onto a slip system for which the line of intersection coincides with the slip direction. In other words, the two slip systems must have the same slip direction. In that case the screw-type segments of the loop already reside on both slip planes and the edge-type segment on the cross slip plane may enhance the total slip. Whether or not cross slip enhances the total slip depends on the second requirement: the slip is enhanced when the direction (or sign) of the resolved

shear stress is equal on both slip systems. If the resolved shear stresses have opposite signs, the edge-type segment on the cross slip plane would move in opposite direction as compared to the segment on the original plane. Hence, there is no driving force in this case and the cross slip will therefore not occur.

The 12 octahedral $\{111\}\langle 011\rangle$ slip systems provide 6 pairs of cross slip enabling slip systems (see Table 3-1). For example, the $(\bar{1}\bar{1}1)[011]$ slip system acts as the cross slip plane for the $(1\bar{1}1)[011]$ system, as shown schematically in Figure 3-3. The orientation of the crystal relative to the applied load determines whether the signs of the resolved shear stresses are equal. For a uniaxial applied load on a $\langle 001\rangle$ oriented material, the signs of the resolved shear stresses are opposite for all six pairs of associated slip systems, i.e. cross slip will not occur. On the other hand, for a $\langle 111\rangle$ orientation, the signs are equal on four of the six pairs of systems, which enables considerable cross slip. This cross slip mechanism then lowers the deformation resistance of the material considerably, which explains the apparent lower yield stress for the $\langle 111\rangle$ orientation.

3.3.2 Matrix phase constitutive model

The basic ingredient of the crystal plasticity framework in [62] is the relation between the slip rates $\dot{\gamma}^\alpha$ and the resolved shear stresses τ^α for the 12 octahedral slip systems α . The following formulation is used:

$$\dot{\gamma}^\alpha = \dot{\gamma}_0 \left\{ \frac{|\tau_{eff}^\alpha|}{s^\alpha} \right\}^m \left\{ 1 - \exp\left(-\frac{|\tau_{eff}^\alpha|}{\tau^{or}}\right) \right\}^n \text{sign}(\tau_{eff}^\alpha) \quad (3.1)$$

where τ^{or} denotes the Orowan stress, s^α the actual slip resistance and m , n and $\dot{\gamma}_0$ are material constants. The effective stress τ_{eff}^α on slip system α is obtained from the effective stress tensor $\boldsymbol{\sigma}_{eff}$ by

$$\tau_{eff}^\alpha = \boldsymbol{\sigma}_{eff} : \mathbf{P}^\alpha \quad (3.2)$$

where \mathbf{P}^α is the symmetric Schmid tensor defined as

$$\mathbf{P}^\alpha = \frac{1}{2} (\bar{s}^\alpha \bar{n}^\alpha + \bar{n}^\alpha \bar{s}^\alpha) \quad (3.3)$$

The unit length vectors \bar{n}^α and \bar{s}^α are the slip plane normal and slip direction, respectively. The effective stress tensor is defined as the combination of the externally applied stress, the misfit stress and the back stress according to

$$\boldsymbol{\sigma}_{eff} = \boldsymbol{\sigma} + \boldsymbol{\sigma}_{misfit} - \boldsymbol{\sigma}_b \quad (3.4)$$

The Orowan stress, which is the stress required to bow a dislocation line into the channel between two precipitates is given by [52] as

$$\tau^{or} = \frac{\mu b}{2\pi d} \ln\left(\frac{d}{r_0}\right) = \alpha \frac{\mu b}{d} \quad (3.5)$$

where the shear modulus μ is equal to the elastic constant C_{1212} , b the length of the Burgers vector, d the spacing between two precipitates (equal to the channel width) and r_0 the dislocation core radius (in the order of b). A value of 0.85 was taken for α [62].

The slip resistance is related to the availability of mobile dislocations and the resistance of sessile / forest dislocations and therefore depends on the total dislocation density, composed of the SSDs and the GNDs. Moreover, the slip resistance generally decreases with temperature, which was expressed by an exponential term in the original formulation in [62]. However, the analysis of experimental tensile test results [56] over a broad temperature range (550 °C to 950°C) demonstrates that the yield stress of the material initially increases with temperature and only beyond a temperature of 850 °C decreases again. The slip resistance is closely related to the yield stress and therefore a modification of its temperature dependence at low temperatures is proposed here, defined according to

$$s^\alpha = c\mu b \sqrt{|\rho_{SSD}^\alpha| + |\rho_{GND}^\alpha|} (1 - b_1) \exp\left[\frac{Q}{kT} + b_2 T\right] \quad (3.6)$$

where ρ_{SSD}^α and ρ_{GND}^α are the dislocation densities, Q is the activation energy to overcome slip barriers, $k = 1.38 \cdot 10^{-23}$ J K⁻¹ is the Boltzmann constant and T the absolute temperature. The strength parameter c is a material constant. The parameters b_1 and b_2 are zero at temperatures of 850 °C or higher and will attain finite values below that temperature. They thus represent, in a phenomenological manner, the mechanism causing the yield stress increase.

The formulation of equation (3.6) requires the calculation of all dislocation densities (12 edge dislocation densities for the SSDs and 12 edge and 6 screw dislocation densities for the GNDs). The GND densities can be obtained from the plastic deformation gradients in the material as explained in [62]. The SSD densities are calculated on the basis of an appropriate evolution equation [37], starting from an initial value $\rho_{SSD,0}$:

$$\dot{\rho}_{SSD}^\alpha = \frac{1}{b} \left(\frac{1}{L^\alpha} - 2\gamma_c \rho_{SSD}^\alpha \right) |\dot{\gamma}^\alpha|, \quad \rho_{SSD}^\alpha(t=0) = \rho_{SSD,0} \quad (3.7)$$

This evolution equation reflects the net effect of dislocation accumulation (left term in the right-hand side) and annihilation (right term). The parameter γ_c represents the critical annihilation length, i.e. the average distance below which two dislocations of opposite sign annihilate spontaneously. The accumulation rate is linked to the average

dislocation segment length of mobile dislocations on system α , which is determined by the current (total) dislocation state through

$$L^\alpha = \frac{K}{\sqrt{|\rho_{SSD}^\alpha| + |\rho_{GND}^\alpha|}} \quad (3.8)$$

where K is a material constant.

3.3.3 Incorporation of cross slip

As discussed above, cross slip is possible for screw dislocations, which reside in two octahedral $\{111\}$ planes simultaneously. The 12 slip systems can therefore be split into six pairs of cross slip enabling slip systems as indicated in Table 3-1. If the orientation of the resolved shear stresses enables cross slip, the slip rates on both slip systems will be significantly higher than for the case where no cross slip is possible.

The amount of cross slip, and thus the increase of the slip rates, depend on the Schmid factors of the two associated slip systems α_1 and α_2 . The Schmid factor SF^α for slip system α is obtained from the ratio between the resolved shear stress and the Von Mises equivalent stress:

$$SF^\alpha = \frac{\tau_{eff}^\alpha}{\sigma_{eq}} \quad (3.9)$$

A parameter Ω^α is introduced here to quantify the amount of cross slip. It is defined as the positive superposition of the Schmid factors if the signs of the two resolved shear stresses are equal. If the resolved shear stresses are opposite, no cross slip can occur and Ω^α will be zero:

$$\Omega^\alpha = \begin{cases} \left| \frac{\tau_{eff}^{\alpha_1} + \tau_{eff}^{\alpha_2}}{\sigma_{eq}} \right| & \text{for } \tau_{eff}^{\alpha_1} \tau_{eff}^{\alpha_2} \geq 0 \\ 0 & \text{for } \tau_{eff}^{\alpha_1} \tau_{eff}^{\alpha_2} < 0 \end{cases} \quad (3.10)$$

A higher value of Ω^α indicates a more favourable condition for cross slip. The slip rate $\dot{\gamma}^\alpha$ due to dislocation glide depends on the velocity of the gliding dislocation line and its length. Since cross slip yields an extension of the dislocation line length (see Figure 3-3), it will also increase the slip rate. Therefore, a cross slip factor F based on the value of Ω^α is incorporated to enhance the slip rate of the slip systems:

$$\dot{\gamma}^\alpha = \dot{\gamma}_0 F(\Omega^\alpha) \left\{ \frac{|\tau_{eff}^\alpha|}{s^\alpha} \right\}^m \left\{ 1 - \exp\left(-\frac{|\tau_{eff}^\alpha|}{\tau^{or}} \right) \right\}^n \text{sign}(\tau_{eff}^\alpha) \quad (3.11)$$

The resolved shear stress on a slip system, which is in the direction of the Burgers vector (\vec{b}^α) and slip vector (\vec{s}^α), drives the gliding of both the edge segment in the slip direction and the screw segments in a direction normal to \vec{b}^α . The resolved shear stress therefore strongly affects the amount of cross slip. However, when the stress drops below a threshold value τ_{cs} , cross slip becomes a statistical process for which the rate is almost independent of the stress. Whether cross slip occurs in this situation depends on the local conditions, like the slip resistance or the presence of obstacles, on the slip system. The following relation between the cross slip factor F and the values of Ω^α and τ is proposed

$$F(\Omega^\alpha) = \left(C_{cs} \frac{\tau}{s^\alpha} \right)^{\varphi(\Omega^\alpha)} \quad \text{with} \quad \tau = \max(\tau_{eff}^\alpha, \tau_{cs}) \quad (3.12)$$

The stress dependence of the cross slip is a function of the orientation. For example, for a $\langle 111 \rangle$ orientation the dependence is much stronger than for $\langle 011 \rangle$. This is represented by the exponent φ , which is a function of Ω , defined as

$$\varphi(\Omega^\alpha) = A_{cs} (\Omega^\alpha)^{B_{cs}} \quad (3.13)$$

with A_{cs} , B_{cs} and C_{cs} material constants.

The evolution of the SSD density is related to the slip rate, see equation (3.7), and the effect of cross slip at this level is therefore automatically incorporated. Finally, the value of R , the radius of the dislocation influence region that governs the back stress [62], is reduced by a factor $(1 - \Omega^\alpha)$. This reduction is consistent with the physical interpretation of R , which can be associated to the dislocation spacing [58]. Since the dislocation density increases considerably during cross slip, a smaller spacing and hence a smaller R may be expected.

The factor Ω^α is calculated from a combination of resolved shear stresses on both slip systems α_1 and α_2 , so the value of Ω^α will be equal for the two systems. However, since the values of τ^α and s^α are not necessarily equal, the contribution of cross slip can be different for the two slip systems. On the other hand, the cross slip process must be considered as the result of the combined contribution of the two associated slip systems. Moreover, when the two associated slip systems are equally loaded and deformed, resulting in equal values for τ^α , s^α and Ω^α , cross slip will still occur, since it provides an easy way to increase the size of the dislocation loops and increase the plastic deformation. Without cross slip, the screw segments are blocked by the γ/γ' -interfaces and dislocation pile-ups develop there.

Finally, the proposed formulation adds only four parameters to the model. Incorporation of a set of cube slip systems would require at least five additional parameters ($\dot{\gamma}_0$, m , c , K , γ_c) and an additional set of 12 dislocation densities.

3.4 Precipitate phase constitutive model

Ni-base superalloys contain precipitates of the $\text{Ni}_3\text{Al}(\text{Si})$ intermetallic phase. These precipitates can deform plastically by two different mechanisms, particle shearing and climb, which are described in detail in this section. The anomalous yield behaviour of Ni_3Al is discussed as well. A crystal plasticity formulation for both mechanisms is proposed, properly incorporated in the slip law for the precipitate phase.

3.4.1 Precipitate deformation mechanisms

The major part of plastic deformation is accommodated by the matrix phase, where dislocations are moving through relatively narrow channels. When encountering a precipitate, a loop is created around the particle, enabling the dislocation to continue its motion on the slip plane behind the precipitate. This is illustrated in Figure 3-4 and, on the level of the crystal lattice, in Figure 3-5. The dislocation loop around the precipitate may disappear by two different mechanisms, both involving inelastic deformation of the precipitate.

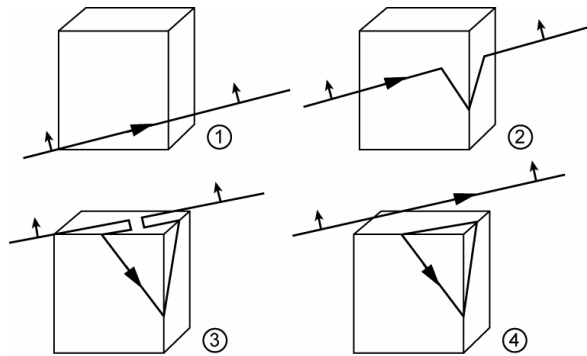


Figure 3-4 Illustration of a moving matrix dislocation line encountering a precipitate (1) and creating a loop around the particle (2-4).

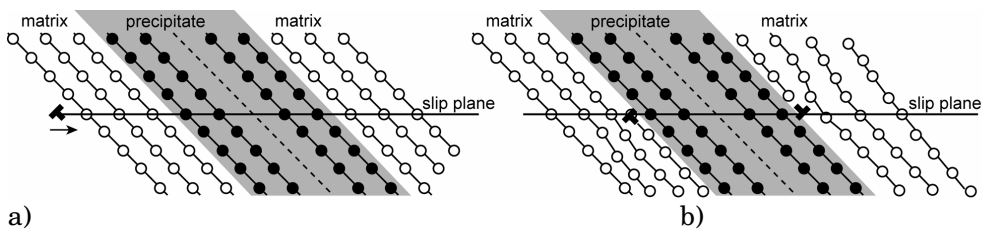


Figure 3-5 Cross-sectional view of the process shown in Figure 3-4 on the level of the crystal lattice, a) a grown-in dislocation is moving towards the precipitate, b) the moving dislocation passed the precipitate and created a loop around the precipitate.

Precipitate shearing

The first mechanism is particle shearing (Figure 3-6), where a dislocation line moves through the precipitate. This process can occur simultaneously with the movement of the dislocation line through the matrix channels between the precipitates, or in a later stage.

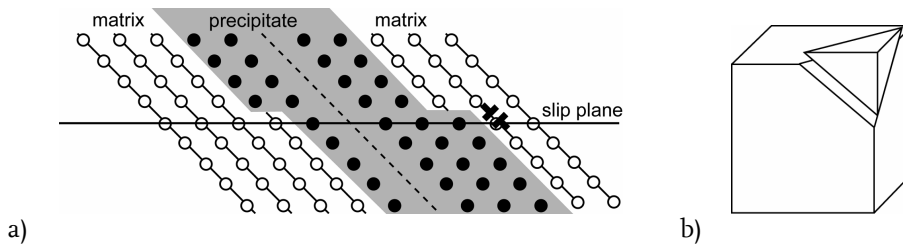


Figure 3-6 a) Cross-sectional view of particle shearing. The precipitate deforms and the dislocation loop vanishes by annihilation of the positive and negative dislocation. b) The resulting deformation of the precipitate.

In the latter case a dislocation loop is initially wrapped around the particle (after the line has passed through the matrix channels, see Figure 3-4) and when it shears the particle, the loop disappears. This is again a slip process along crystallographic planes.

Since the precipitate is an ordered ($L1_2$) solid solution of Al in Ni (Ni_3Al), it forms a superlattice with a perfect dislocation ($a\langle 110 \rangle$) which is twice as large as the nickel matrix perfect dislocation ($\frac{1}{2}a\langle 110 \rangle$). Therefore, on entering the precipitate, a matrix dislocation causes either an anti-phase boundary (APB) or a superlattice intrinsic stacking fault (SISF), depending on the dissociation mechanism. The APB or SISF is recovered when the next matrix dislocation enters the precipitate. Therefore, in the precipitate dislocations always move in pairs, connected by an APB or SISF. This is illustrated in Figure 3-7 for a dislocation line that shears the precipitate without creating

a loop around the particle. The respective energies determine which of the two mechanisms occurs.

Anomalous yield behaviour

The pair-wise movement of dislocations causes a typical phenomenon, which is known as the anomalous yield behaviour of Ni₃Al [68,71]. In experiments the following remarkable aspects are observed:

- the yield stress increases with increasing temperature up to the peak temperature (T_p),
- the flow stress shows a tension-compression asymmetry.

The latter aspect causes the material to violate the Schmid law (non-Schmid behaviour). The origin of the anomalous yield behaviour is the thermally activated locking of superdislocations by cross slip, as will be explained next.

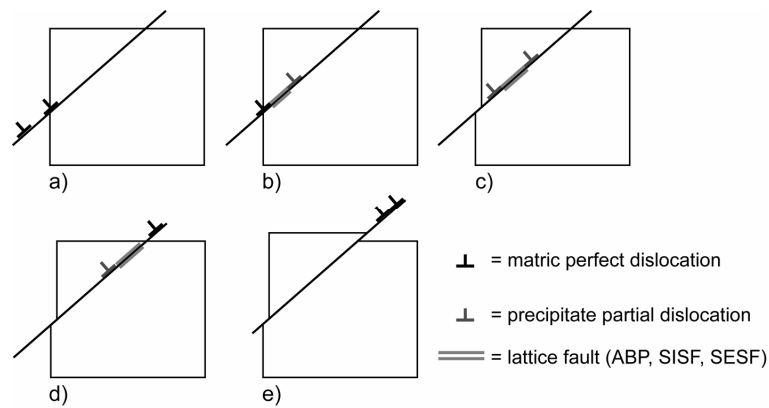


Figure 3-7 Schematic representation of the shearing of the precipitate superlattice by a pair of matrix dislocations.

The perfect superlattice dislocations ($a\langle 110 \rangle$) can dissociate in a number of ways:

$$i. \quad a[\bar{1}01] \rightarrow \frac{a}{2}[\bar{1}01] + APB + \frac{a}{2}[\bar{1}01] \quad (3.14)$$

with an APB between the superpartials. The two superpartials can further dissociate into two Shockley partials separated by a complex stacking fault (CSF)

$$\frac{a}{2}[\bar{1}01] \rightarrow \frac{a}{6}[\bar{1}\bar{1}2] + CSF + \frac{a}{6}[\bar{2}11] \quad (3.15)$$

$$2. \quad a[\bar{1}01] \rightarrow \frac{a}{3}[\bar{2}11] + \text{SISF} + \frac{a}{3}[\bar{1}\bar{1}2] \quad (3.16)$$

with a SISF between the two superpartials. The energy of this dissociation is relatively high, which means that it only occurs when the APB is unstable or its energy is high.

At low temperatures the pairs of dislocations can freely glide on the (111) planes. At higher temperatures however, screw dislocations can cross slip from (111) to (010) planes, on which they are sessile owing to the spreading of their cores onto (111) or $(1\bar{1}1)$ planes. Spreading of the dislocation core means that two Shockley partials move away from each other (dislocation splitting), with the shear stress normal to the Burgers vector as the driving force. Before a dislocation core can spread onto another slip plane, it has to form a constriction (zero dislocation splitting) as shown in Figure 3-8.

Furthermore it is assumed that cross slip only occurs locally along short segments of the dislocations, leading to the formation of pinning points. These pinning points then act as obstacles to the dislocation motion. This is also known as a Kears-Wilford lock. The cross slip process is thermally activated and is therefore more frequent at higher temperatures. Therefore, the density of pinning points also increases with increasing temperature, resulting in the observed increase in yield strength.

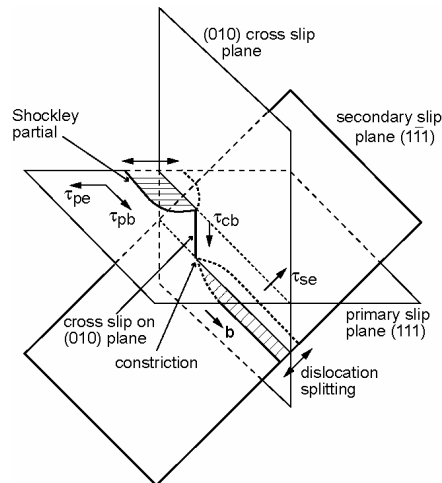


Figure 3-8 Schematic picture of a cross slipped screw dislocation with a core spread in a primary and secondary {111} plane, showing the shear stress components playing a role in the cross slip process.

Recovery climb

The second mechanism of precipitate deformation is climb or recovery, where the dislocation climbs around the precipitate. This process is thermally induced and involves diffusional processes and is therefore much slower than the previous mechanism. However, there is no stress threshold, which means that it prevails when the stress is below the threshold stress for particle shearing. The mechanism is illustrated in Figure 3-9.

Precipitate atoms are diffusing from the one side of the precipitate to the other side along the dislocation loop (pipe diffusion). This diffusion process leads to climbing of the dislocation loop and simultaneous deformation of the precipitate. The deformation is limited to the original plane of the dislocation loop. When the dislocation loop has climbed towards the apex of the precipitate, the loop can annihilate and the deformation of the precipitate is equivalent to that caused by shearing of the particle by the matrix dislocation in its initial slip plane, as visualized in Figure 3-9.

As in some other models [22,23,28,30], it will be assumed that precipitate deformation (by shearing or climb) only occurs when a complete loop around the precipitate is available. The precipitate deformation is therefore dependent on the matrix deformation (which generates the dislocation loops). On the other hand precipitate deformation decreases the number of deposited dislocation loops which decreases the back stress in the matrix region.

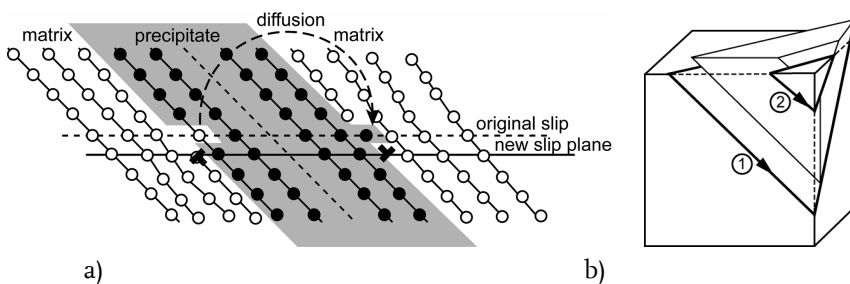


Figure 3-9 a) The dislocation climbs out of the slip plane, assisted by diffusion of precipitate atoms along the dislocation loop. The precipitate deforms and the loop is in a new slip plane. b) Precipitate deformation at an intermediate stage of the climb process. The loop has climbed from position 1 to position 2. When the dislocation loop has reached the apex of the precipitate, the deformation will be equal to that after shearing (see Figure 3-6b).

3.4.2 Crystal plasticity formulation for particle shearing

The γ' -particles do not contain grown-in dislocations [28] like the matrix phase, so deformation of the precipitate can only occur when a matrix dislocation shears the particle. A matrix dislocation must overcome a threshold before it can enter the particle,

and then the lattice slip resistance must be exceeded before it can move inside the precipitate. The magnitude of the slip rate is determined by the ratio between the effective stress and the lattice resistance, and the number of dislocations that shears the particle per unit of time. A generic equation for the slip rate, applicable to precipitate shearing, is proposed:

$$\dot{\gamma}^{\alpha} = \dot{\gamma}_0^{\alpha} \left\{ 1 - \exp \left(- \frac{|\tau_{eff}^{\alpha}|}{s_0^{\alpha}} \right) \right\}^p \text{sign}(\tau_{eff}^{\alpha}) \quad (3.17)$$

which is similar to equation (3.1) for the matrix phase. The effective stress on slip system α , τ_{eff}^{α} , is commonly defined through equations (3.2) to (3.4). In the matrix phase, the lattice slip resistance is strongly dependent on the dislocation density. Since no large increase in dislocation density inside the precipitate is expected, s_0^{α} is assumed to remain constant during deformation. The threshold for slip in (3.17) is defined as an exponential function, acting as a multiplier ranging from 0 to 1. The exponent p and the prefactor $\dot{\gamma}_0^{\alpha}$ are material constants.

The magnitude of the slip rate is governed by the number of dislocations that shears the particle per unit of time. The dislocation threshold for entering the precipitate is related to the process of dissociation into superpartials and the accompanying lattice faults (APB, SISF). This threshold is generally defined as the ratio between the lattice fault energy and the Burgers vector of the perfect superlattice dislocation. Yuan et al. [52] and Brown and Ham [72] present a threshold stress for particle shearing through dislocations connected by an APB which depends on the particle volume fraction. The relation shows that with increasing particle volume fraction the threshold decreases, but the origin of this dependence is not clear. Therefore, the volume fraction dependence was not included in the present model. On the other hand, no temperature dependent formulation for the threshold stress has been found in the literature, whereas experimental observations show a clear decrease of the applied stress required to initiate precipitate shearing (see section 3.5). Therefore, a temperature dependent threshold is proposed here

$$\tau_c^{\alpha}(T) = \tau_{c,0}^{\alpha} - a_1 \exp[a_2(T - T_0)] \quad (3.18)$$

in which $\tau_{c,0}^{\alpha}$ is the threshold stress at a reference temperature T_0 and a_1 and a_2 are constants. The values of $\tau_{c,0}^{\alpha}$, T_0 , a_1 and a_2 can be determined from experiments at different temperatures (section 3.5).

Relations for the frequency of dissociation are given in two papers by Fedelich [22,23] for the SISF and APB shearing mechanisms, respectively. However, both

formulations are not able to properly describe the observed behaviour of the superalloy CMSX-4. Since it is not possible to distinguish between the two mechanisms unambiguously, only the SISF mechanism is considered in the present model by modification of the relations used by Fedelich [22]. The frequency of dissociation is defined as

$$f_{diss} = f_0 \exp\left(-\frac{\Delta E}{kT}\right) \quad (3.19)$$

In this relation f_0 is a constant and the activation energy ΔE is given by

$$\Delta E = \beta \frac{\mu^{3/2} b_{sisf}^3}{\sqrt{|\tau_{eff}^\alpha| - \tau_c^\alpha(T)}} \quad (3.20)$$

where μ is the precipitate shear modulus, b_{sisf} is the Burgers vector of the partial dislocation $\frac{a}{3}\langle 112 \rangle$ and β is a constant. As long as the effective shear stress is below the threshold, no thermal activation is possible, $f_{diss} = 0$. For shear stresses exceeding the threshold, the frequency increases from 0 to f_0 (for $\tau_{eff}^\alpha \gg \tau_c^\alpha$).

Finally the slip rate is obtained by multiplying the dissociation frequency by the number of available dislocations at the interface, the Burgers vector b and some geometric quantities:

$$\dot{\gamma}_0^\alpha = \frac{bS}{V} f_{diss} \tilde{\rho}_{GND}^\alpha S_{int} \quad (3.21)$$

where S and V are the particle area swept by the dislocation and the particle volume, respectively and S_{int} is the area of the interface. Note that V , S and S_{int} can be expressed in terms of the microstructural dimensions. The Burgers vector in this case is the vector used to calculate the GND density. As emphasised in [62], this is the matrix phase Burgers vector.

The number of available dislocations can be obtained from the edge dislocation densities at the different interfaces. In general, GNDs are related to deformation gradients, but since in the current model deformation gradients are supposed to be concentrated at the interfaces between different regions (uniform strain inside regions), the GNDs represent the interface dislocations. Moreover, the GND density does not represent the total number of dislocations, but only describes the net effect of positive and negative dislocations. And precisely this surplus represents the number of dislocation loops available for particle shearing. Further, due to the orientation of the different slip systems relative to the particles, the slip direction \bar{s} is always parallel to one of the three precipitate-matrix interfaces in the $\{111\}$ slip plane, see Figure 3-10.

(τ_{pb} , on the primary slip plane in the direction of the Burgers vector), also other stress components drive the slip behaviour. The additional stress components are (see Figure 3-8 and Table 3-1):

- τ_{pe} : the stress on the primary slip plane normal to the Burgers vector, which drives the dislocation splitting on the primary slip plane,
- τ_{se} : the stress on the secondary slip plane normal to the Burgers vector, which drives the dislocation splitting on the secondary slip plane,
- τ_{cb} : the stress on the (010) cross slip plane in the direction of the Burgers vector.

These three additional stress components play a role in the cross slip process and an effective shear stress is defined as

$$\tau_{non-Schmid}^{\alpha} = \tau_{pb}^{\alpha} - A \operatorname{sign}(\tau_{pb}^{\alpha}) (\tau_{pe}^{\alpha} - \kappa \tau_{se}^{\alpha}) - B \tau_{cb}^{\alpha} \quad (3.23)$$

where the non-Schmid factors A , B and κ are material parameters which are temperature dependent. The stress τ_{cb}^{α} on the cube slip system always decreases the effective stress due to its positive effect on the cross slip and spreading process, resulting in a negative effect on the mobility. The effect of the combined term $\tau_{pe}^{\alpha} - \kappa \tau_{se}^{\alpha}$ depends on the sense of the resolved shear stress τ_{pb}^{α} . If τ_{pe}^{α} has a sign not equal to that of τ_{pb}^{α} , it will stimulate the dislocation splitting on the primary plane and therefore avoid the formation of a constriction and pinning points. For τ_{se}^{α} the effect is opposite: increase of the splitting on the secondary slip plane enhances formation of a constriction, resulting in a decreased mobility. The parameter κ represents the relative importance of τ_{pe}^{α} and τ_{se}^{α} in forming a constriction. Note that the contribution of τ_{pb}^{α} and τ_{cb}^{α} to the generated slip simply reverses when the applied stress is reversed (from a tensile to a compressive state). That does not hold for the spreading mechanism governed by $\tau_{pe}^{\alpha} - \kappa \tau_{se}^{\alpha}$, which is dependent both on the sense of the applied stress and the orientation of the material. For a $\langle 001 \rangle$ oriented material, an applied tensile stress leads to a decrease of the splitting on the primary plane, which decreases the mobility and thus the (absolute value of the) effective stress, whereas a compressive stress increases the splitting, increases the mobility and thus increases the (absolute value of the) effective stress. This tension-compression asymmetry is taken into account by the two parts of relation (3.23). The effect can be included in the present model by replacing the external stress part of τ_{eff}^{α} in equation (3.2) by the right-hand part of equation (3.23), according to:

$$\tau_{eff}^{\alpha} = \tau_{pb}^{\alpha} \pm A (\tau_{pe}^{\alpha} - \kappa \tau_{se}^{\alpha}) - B \tau_{cb}^{\alpha} + \tau_{misfit}^{\alpha} - \tau_b^{\alpha} \quad (3.24)$$

where the \pm selection depends on the sense of τ_{pb}^{α} according to (3.23).

The increase of the slip resistance with temperature due to the formation of pinning points is incorporated through a temperature dependent s_0^α :

$$s_0^\alpha = s_{0,T_p}^\alpha \exp\left(-\frac{k|T-T_p|}{D}\right) \quad (3.25)$$

where T_p is the peak temperature, s_{0,T_p}^α the slip resistance at T_p and D the activation energy. The decrease beyond the peak temperature is also represented by the temperature dependence of τ_c as given by equation (3.18). The reference temperature T_0 in (3.18) can thus be associated to the peak temperature T_p , which is about 750 °C for Ni₃Al [68].

In almost any superalloy constitutive model this non-Schmid behaviour is neglected, except for the rather simple model proposed by Allan [70]. Experimental results and the simulations in section 3.6.3 show that there is a clear effect on the superalloy mechanical behaviour, which justifies the inclusion of the anomalous yield behaviour in the model. However, determination of the parameters in (3.24) requires specific experimental results, which may not be readily available. Only when a detailed description of the typical Ni₃Al behaviour is required, the effort to determine the parameters may be justified. In other cases the non-Schmid behaviour can be neglected by setting the constants A and B to zero, where it should be mentioned that the non-Schmid effects particularly play a role at lower temperatures (at or below the peak temperature).

3.4.3 Crystal plasticity formulation for climb

The diagonal of the cubic particle normal to the {111} plane is denoted by H_γ , and its length equals $\sqrt{3}$ times the precipitate cube length. The average distance for a dislocation loop to climb towards the apex of the particle is then $H_\gamma/4$. The climb velocity is governed by the diffusion of precipitate atoms around the particle. This process is temperature dependent and although the dislocation loop is moving out of the slip plane, the diffusing atoms causing this climb are moving in the original slip plane. Therefore, the resolved shear stress on that slip system is defined as the driving force, as confirmed by [23] on the basis of energy considerations. Accordingly the following relation for the climb velocity is proposed:

$$v_{climb}^\alpha = C |\tau_{eff}^\alpha| \exp\left(-\frac{Q^c}{R_{gas} T}\right) \text{sign}(\tau_{eff}^\alpha) \quad (3.26)$$

where C is a proportionality constant that has to be determined from experimental results and the effective shear stress is again given by equations (3.2) to (3.4). Contrary

to the relation used by Fedelich, this relation contains a temperature dependence, which is derived from the underlying diffusion process. Q^c is the associated activation enthalpy for diffusion and $R_{gas} = 8.3144 \text{ J K}^{-1} \text{ mol}^{-1}$ is the gas constant. The activation enthalpy for self-diffusion of nickel is 142 kJ/mol [54]. Diffusion along a dislocation line is easier than through the bulk material and the activation enthalpy is known to be reduced by a factor of 0.6 [73]. Therefore, a value of Q^c equal to 85 kJ/mol will be used.

The slip rate is obtained by dividing the climb velocity by the average climb distance and multiplication by the Burgers vector, the average GND density and a number of geometric quantities, as was discussed in the previous section, leading to

$$\dot{\gamma}^\alpha = \frac{v_{climb}^\alpha}{H_{\gamma'}} \frac{4bS}{V} \tilde{\rho}_{GND}^\alpha S_{int} \quad (3.27)$$

Again V , S , $H_{\gamma'}$ and S_{int} can be expressed in terms of the microstructural dimensions. Climb also reduces the GND densities at the interfaces, because the deformation gradient across the interface is reduced.

3.4.4 Total precipitate deformation

Combining the contributions of shearing and climb [equations (3.17), (3.21) and (3.27)] leads to the following expression for the precipitate slip rate:

$$\dot{\gamma}^\alpha = \frac{SbS_{int}}{V} \tilde{\rho}_{GND}^\alpha \left[f_{diss} \left\{ 1 - \exp\left(-\frac{|\tau_{eff}^\alpha|}{s_0^\alpha}\right) \right\}^p + \frac{4v_{climb}^\alpha}{H_{\gamma'}} \right] \text{sign}(\tau_{eff}^\alpha) \quad (3.28)$$

If the stress is lower than the threshold for particle shearing, climb still leads to precipitate deformation (but at a much lower rate). If shearing occurs, the climb contribution can be neglected. The effective resolved shear stress and temperature act as driving forces for slip in a similar way as in the γ -matrix constitutive model.

3.5 Model parameter determination

Due to the inclusion of a number of physical mechanisms, the presented model contains a substantial number of model parameters. Therefore, a considerable amount of experimental data is required to determine the unique set of parameter values. In this section, the method that is used to determine the values for the commercial superalloy CMSX-4 is described.

An overview of the required constants and material parameters for the model and their eventual values is given in Table 3-4. A distinction can be made between parameters with a clear physical meaning (δ , $\lambda_{\gamma'}$, λ_{γ} , α , k , b , b_{sisf} , T_p , Q^c , R_{gas} , μ_m and μ_p)

and fit parameters for matrix slip ($\dot{\gamma}_0$, m , Q , c , γ_c , $\rho_{SSD,o}$, K , b_1 , b_2), precipitate slip (s_0^α , p , $\tau_{c,o}$, a_1 , a_2 , f_0 , β , C), matrix cube slip (A_{cs} , B_{cs} , C_{cs} , τ_{cs}), non-Schmid effects (A , B , κ , D , s_{0,T_p}^α , T_p) and size dependency (n , R). The fit parameters are determined from experimental data, as will be shown below.

Table 3-4 Model parameters for CMSX-4.

Model parameter	Symbol	Value	Unit	Eq.nr
Lattice misfit at 850°C	δ	$-1.1 \cdot 10^{-3}$		-
Matrix coefficient of thermal expansion	λ_γ	$1.48 \cdot 10^{-5}$	K ⁻¹	-
Precipitate coefficient of thermal expansion	$\lambda_{\gamma'}$	$1.32 \cdot 10^{-5}$	K ⁻¹	-
Reference slip rate	$\dot{\gamma}_0$	$2.5 \cdot 10^{-11}$	s ⁻¹	(3.1)
Rate sensitivity exponent Orowan threshold	n	2		(3.1)
Rate sensitivity exponent slip resistance	m	13.8		(3.1)
Reference activation energy	Q	$3.62 \cdot 10^{-20}$	J	(3.6)
Strength parameter	c	0.0415		(3.6)
Matrix shear modulus	μ	100.2	GPa	(3.6)
Matrix Burgers vector length	b	0.254	nm	(3.6)
Slip resistance temperature dependence	b_1	0.98275	-	(3.6)
	b_2	$3.636 \cdot 10^{-3}$	K ⁻¹	(3.6)
Orowan parameter	α	0.85		(3.5)
Critical annihilation length	γ_c	13.5	nm	(3.7)
Initial SSD density	$\rho_{SSD,o}$	$1.2 \cdot 10^{14}$	m ⁻²	(3.7)
Dislocation segment length parameter	K	3.5		(3.8)
Radius of dislocation influence region	R	20	nm	
Matrix cross slip parameters	C_{cs}	2.4		(3.12)
	A_{cs}	404		(3.13)
	B_{cs}	6.6		(3.13)
Threshold stress for cross slip	τ_{cs}	122	MPa	(3.12)
γ' lattice resistance at peak temperature	s_{0,T_p}^α	120	MPa	(3.17)
Stress exponent particle shearing	p	4		(3.17)
Frequency constant	f_0	10 ⁴	Hz	(3.19)
Energy constant	β	$3.0 \cdot 10^{-3}$		(3.20)
Partial dislocation Burgers vector	b_{sisf}	0.293	nm	(3.20)
Precipitate shear modulus	μ_p	105.2	GPa	(3.20)
Threshold stress at T_p	$\tau_{c,o}$	330	MPa	(3.18)
Peak temperature	$T_o = T_p$	750	°C	(3.18)
Threshold stress temperature dependence	a_1	2.96	MPa	(3.18)
	a_2	0.0157		(3.18)
Non-Schmid parameters	A	0.3		(3.23)
	B	0.1		(3.23)
	κ	0.4		(3.23)
Slip resistance temperature dependence	D	∞	J	(3.25)
Diffusion activation enthalpy	Q^c	85	kJ mol ⁻¹	(3.26)
Climb velocity constant	C	$3.0 \cdot 10^{-17}$	m ² s kg ⁻¹	(3.26)

The CMSX-4 microstructure (Figure 1-3) is rather regular, so for the present model the precipitates are assumed to be cubic with a size of 500 nm. The matrix channel width is taken as 60 nm. These values yield a γ' volume fraction of 72%. Experimental results for creep tests and tensile tests on CMSX-4 are obtained from a European collaborative research project [56]. Additional data was collected from the open literature [40-42,45,74-76]. An overview of the available tests used for the parameter determination and the model validation is given in Table 3-5.

Note that for most conditions only one experiment is available, that may statistically not be fully representative for that condition. Tensile test results for conditions where several experiments are available (e.g. 850 °C; 6 %/min) show that the scatter in the experimentally observed stress values is in the order of 50 MPa. On the other hand, since many experiments over a large range of conditions are used, the appropriate average behaviour will be obtained.

A least-squares fitting procedure was used to determine the model parameters. The multiscale model is implemented in a subroutine that calculates a tensile or creep curve for a specific condition and a set of model parameters. An optimization routine then minimizes the sum of the squared differences between the calculated results and corresponding experimental values. Using knowledge of the physical mechanisms at the microscopic level, the complete set of parameters is split-up into a number of smaller sets that can be calibrated separately.

Table 3-5 Overview of available experimental data: for each temperature (°C) value stress (MPa) levels for the creep tests and strain rate (%/min) levels for the tensile tests are given. The orientation is <001>, unless specified otherwise.

Creep tests					
	750 °C	800 °C	850 °C	900 °C	
	725 ^a	650	284 ^a	300	
	820	750	345 ^a	325	
			393 ^a	375 ^a	
			650 ^a	400 ^a	
				425	
Tensile tests					
550 °C	700 °C	800 °C	850 °C	950 °C	1000 °C
6.0 ^a	6.0	0.6	0.6 ^a	6.0 ^a	0.6
	0.6 <111>	6.0	6.0 ^a	6.0 <111>	4.3
		60	60 ^a		
			6.0 ^a <011>		
			6.0 ^a <111>		
			0.6 <111>		

^a tests used for fitting of the model parameters

From experimental work it is known that the mechanism of particle shearing is only active at higher stresses, since the threshold for shearing must be exceeded. A survey of experimental work on CMSX-4 [11,30,40-48,74,75] indicates the applied stress levels, as a function of temperature, where the shearing mechanism is observed to be either active or inactive. This is represented by the two solid lines in Figure 3-11 and illustrates the variation of the particle shearing threshold stress with temperature. Note that in the model the threshold is defined in terms of the effective resolved shear stress, equations (3.18) and (3.20), which is a combination of the applied stress and the internal stress, whereas Figure 3-11 shows the externally applied (normal) stress only.

For a load in the $\langle 001 \rangle$ direction, the Schmid factor is $\pm \frac{1}{\sqrt{6}}$ for 8 of the 12 slip systems and zero for the remaining 4 systems, resulting in a resolved shear stress equal to the applied tensile stress divided by $\sqrt{6}$. In the early stages of deformation the back stress is assumed to be negligible, so only the effect of the misfit stress has to be accounted for. The variation of the misfit stress and the effective shear stress are also plotted in Figure 3-11 and the latter curve was used to determine the parameters τ_{c0} (at 750 °C), a_1 and a_2 in equation (3.18). Moreover, Figure 3-11 can be used to determine which experiments from Table 3-5 should be used for fitting a specific set of parameters. For the low stress levels in the lower left part of Figure 3-11 the shearing mechanism is inactive and these test results are used to determine the parameters for the matrix slip and climb mechanisms. Once these parameters are known, the tests at high stress levels are used to determine the shearing parameters. The conditions used for the fitting procedure are indicated in Table 3-5.

Climb is a slow process, since it depends on diffusion of atoms around the precipitates. Therefore, the mechanism is not active at high strain rates during a tensile test. Further, due to the absence of a stress threshold, the climb mechanism will be active unconditionally. However, the climb mechanism cannot be separated from the matrix slip mechanism, since a certain GND density, and thus matrix slip, is required to initiate the climb mechanism. Therefore, the climb parameter C is determined simultaneously with the matrix parameters.

The matrix slip parameters $\dot{\gamma}_0$, c , γ_c , $\rho_{SSD,0}$ and K are determined from the tensile and creep tests at the conditions for which the precipitate shearing is inactive. Since deformation of the matrix phase causes the development of internal stresses, which might initiate particle shearing, only the primary part of the creep curves and the part of the tensile curves up to the maximum stress level are used. The temperature

dependence of the slip resistance, as quantified by the parameters b_1 and b_2 , is determined from the variation of the macroscopic yield stress at different temperatures.

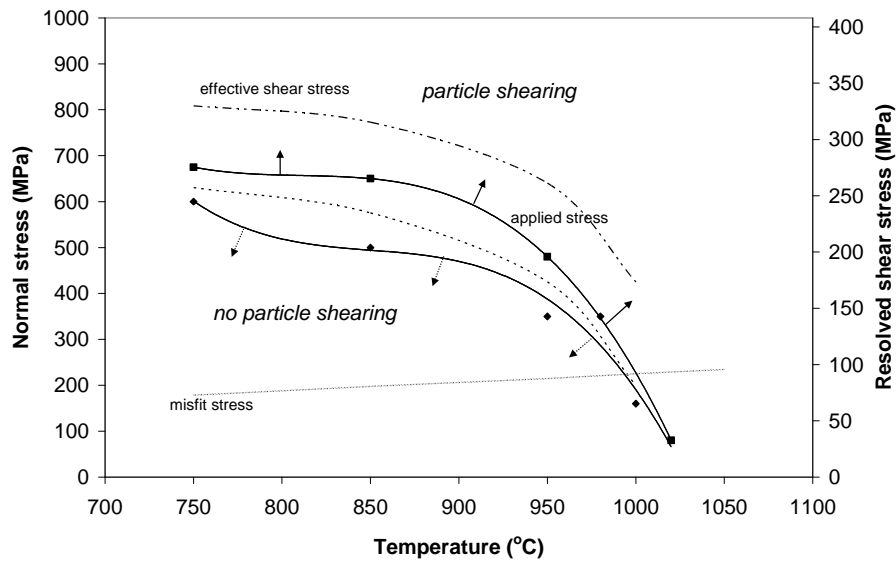


Figure 3-11 Activation of the precipitate shearing mechanism during creep tests as a function of stress and temperature. The solid lines are in terms of applied stress and are obtained from experimental observations. The effective stress is the sum of the applied stress and the temperature dependent misfit stress.

The precipitate shearing parameters p , f_0 , β and s_0^α are then determined using the conditions where the shearing mechanism is active: creep tests at higher stress levels, the secondary part of the creep curves at lower stress levels and the complete tensile curves. Only a part of the complete creep curve can be used, i.e. the part up to 0.5 % (900 °C) or to 2 % (750 °C) creep strain. At higher strains or temperatures the rafting mechanism (with gradual change of the microstructure) becomes active, which is not incorporated in the present model. At temperatures beyond 950 °C rafting starts right from the beginning of plastic deformation.

The cube slip parameter values are obtained using the tensile curves at 850 °C and 6%/min strain rate for the three orientations, as indicated in Table 3-5. With these values, the factor Ω attains a value of 0.52 for a $\langle 111 \rangle$ oriented material, resulting in an exponent ϕ equal to 6, while for a $\langle 011 \rangle$ orientation, Ω becomes 0.43 and ϕ equals 1.5.

Finally, the parameters that describe the non-Schmid behaviour, A , B , κ , D , T_p and s_{0,T_p}^α , can only be determined from tests that show the tension-compression asymmetry and the temperature dependence of the yield stress. Such tests are not

readily available for CMSX-4, so the parameters for Ni_3Al from [68] were used for A , B , κ and T_p and the slip resistance temperature dependence was neglected by setting the value of D to infinity, resulting in $s_0^\alpha = s_{0,T_p}^\alpha$. The parameters n and R describe the size dependence and their values can be determined from tests on specimens with different microstructural dimensions. Their values were taken from [62].

3.6 Results

The model described in the previous sections has been used to simulate the mechanical response of the single crystal Ni-base superalloy CMSX-4. Simulated creep curves and tensile curves are compared to experimental results to show that the model is able to describe the material mechanical behaviour for a range of conditions. Moreover, the capability of the model to represent the material orientation dependence and non-Schmid behaviour is demonstrated.

3.6.1 Simulation of creep and tensile tests

The simulated creep curves for a range of conditions are plotted in Figure 3-12 together with the experimental creep curves (mind the different scales along the axes). This figure shows all the cases that were used for the parameter determination.

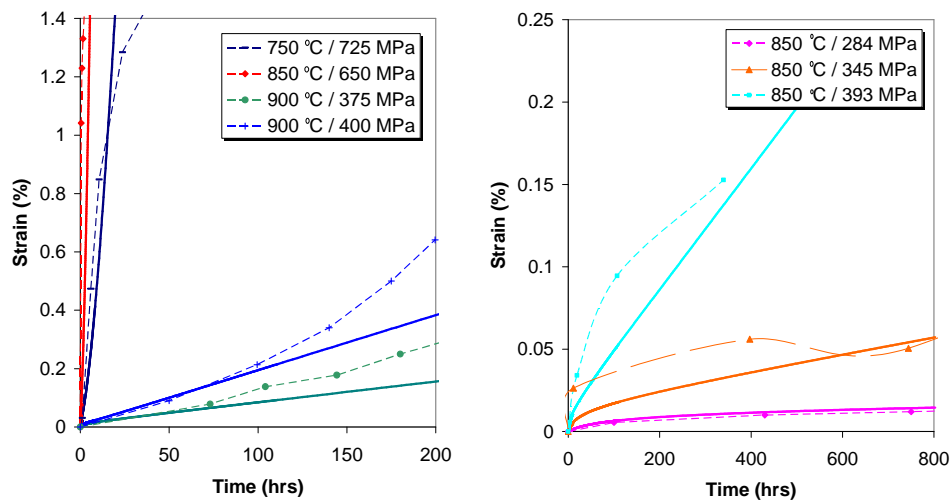


Figure 3-12 Simulated (solid lines) and experimental creep curves (dashed lines with markers) for the tests that were used for parameter determination (see Table 3-5).

A wide range of temperatures and stress levels is used to determine one set of model parameters that covers all conditions. For these conditions the model simulates the real

material behaviour quite well. Since the rafting process is not included in the model, it is not possible to apply the model at higher temperatures and / or longer creep times than those in Figure 3-12.

Figure 3-13 shows the comparison between simulated and experimental tensile curves for two different temperatures and several strain rates. The experiments are simulated quite well and especially the steady-state stress levels are in most cases close to the experimental values. The shape of the curves qualitatively matches the experiments. In general the curves show an initial peak followed by a decrease in stress, caused by the onset of precipitate shearing, and then find their way towards the steady state stress level at which the combination of matrix and precipitate plastic flow agrees with the applied strain rate.

Since one set of model parameters has been determined for a wide range of experimental conditions, predictions can be made for conditions other than those used to identify these parameters. This is demonstrated in Figure 3-14, where simulated tensile tests are compared to experimental results for a variety of test conditions. The differences between simulations and experiments are now somewhat larger, yet the simulated tensile curves still match the experiments adequately.

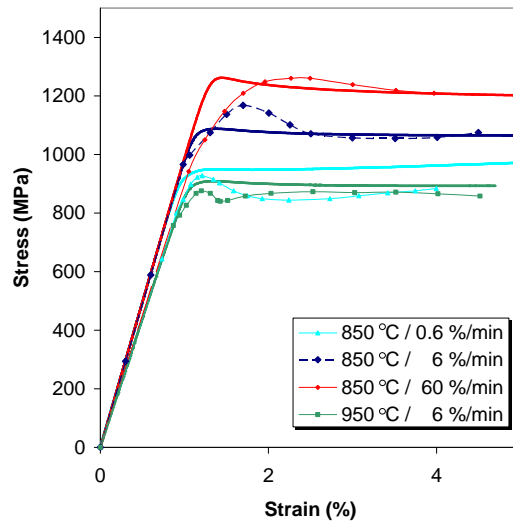


Figure 3-13 Simulated (solid lines) and experimental tensile curves (dashed lines with markers) for the conditions that were used for parameter determination.

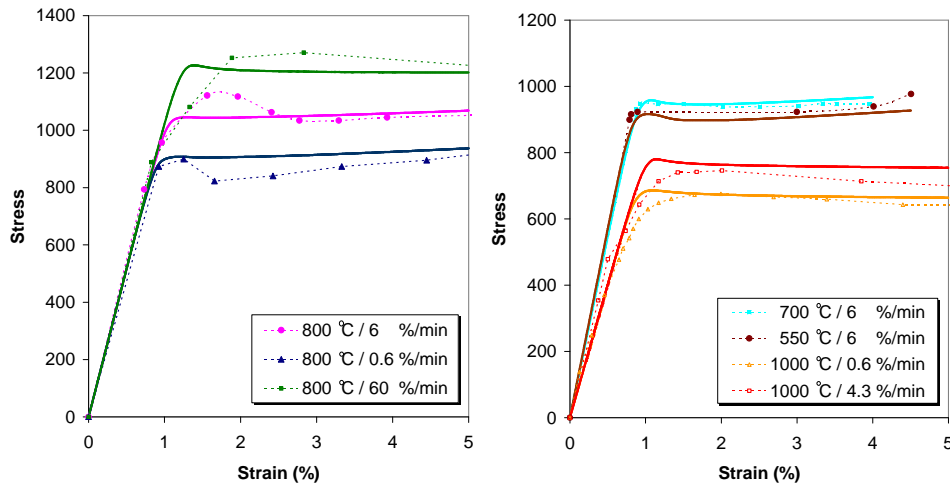


Figure 3-14 Simulated tensile curves (solid lines) compared to experimental results (dashed lines with symbols) for several conditions.

The results displayed in this subsection show that the model is able to simulate the material behaviour quite well for a range of conditions by using only a single set of model parameters. Other models are available that may describe the behaviour for a specific loading case slightly better, since the associated set of parameters is determined specifically for that case. However, such models are generally not able to describe the material behaviour at other conditions without performing a new parameter fit procedure. Moreover, in a multiscale approach, where the model is applied to real gas turbine components [62], a range of temperatures will be encountered and only a widely applicable material model is expected to produce reliable results for that purpose.

The ability to describe the material behaviour for a wide range of conditions indicates that the model contains most of the right physical mechanisms governing the material response. The main aspect that is currently still missing in the present model is the rafting mechanism. Inclusion will be subject of future work. The cyclic behaviour of the material and the associated damage accumulation are addressed in a separate paper [77].

3.6.2 Cube slip

At $\langle 111 \rangle$ and $\langle 011 \rangle$ orientations, the cross slip mechanism as discussed in section 3.3 is active, resulting in macroscopic cube slip in addition to the regular octahedral slip.

Simulated tensile curves are compared to experimental results for different orientations and test conditions in Figure 3-15.

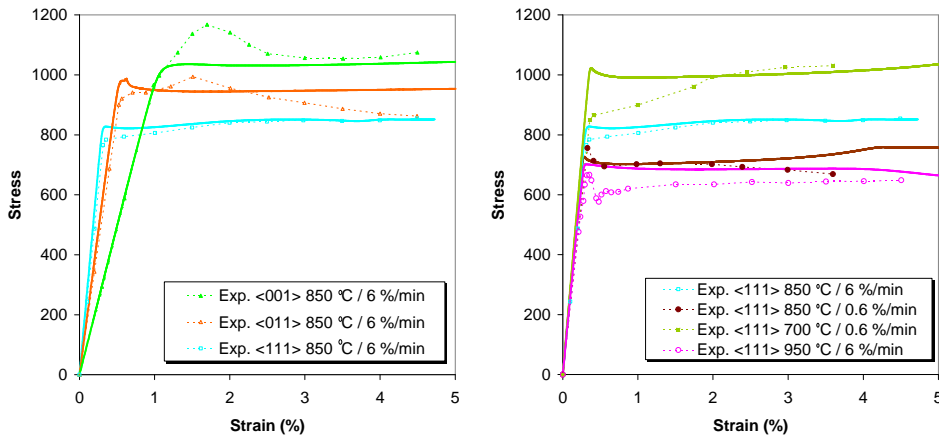


Figure 3-15 Simulated tensile curves (solid lines) compared to experimental curves for different crystal orientations at 850 °C (left) and for different temperatures and strain rates for the $\langle 111 \rangle$ orientation (right).

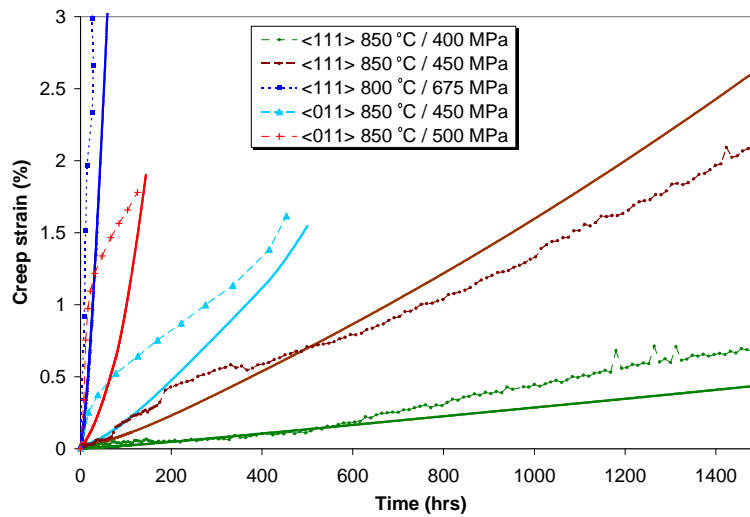


Figure 3-16 Simulated creep curves (solid lines) compared to experimental results for different crystal orientations, temperatures and stress levels.

These results clearly demonstrate the changes in elastic response of the material for the different orientations, but more importantly, also the reduced strength induced by the

cross slip mechanism. The resulting macroscopic cube slip causes much more plastic deformation in the $\langle 111 \rangle$ orientation, thereby reducing the material yield stress and strength considerably. As can be observed, the model adequately simulates these effects.

Figure 3-16 shows a number of simulated creep curves and the corresponding experimental results. Again, the model is able to simulate the material response quite reasonably over a wide range of conditions. The results in Figure 3-15 and Figure 3-16 demonstrate that the use of the formulation for the cross slip mechanism, as proposed in this work, yields an adequate simulation of the material orientation dependence.

3.6.3 Anomalous yield behaviour

In section 3.4.1 the anomalous yield behaviour of Ni_3Al was discussed. Since the superalloy is a compound of a Ni-matrix and Ni_3Al -precipitates, the anomalous yield behaviour of the precipitates will also affect the overall alloy mechanical behaviour. In this section the effects are discussed and illustrated.

The tension-compression asymmetry of the precipitate yield stress is introduced in the present model through equation (3.24). In experiments on $\text{Ni}_3(\text{Al},\text{Nb})$ [68,78] it is observed that for the $\langle 001 \rangle$ crystal orientation the tensile yield stress for the precipitates is higher than the compressive yield stress ($T > C$), while for the $\langle 011 \rangle$ orientation the effect is opposite ($T < C$).

The response of the two-phase superalloy CMSX-4, including the Ni_3Al precipitates, was investigated by Allan [70], who performed experiments at relatively low temperatures ranging from 400 °C to 850 °C and a strain rate of 10^{-4} s^{-1} . The same trends in tension-compression asymmetry were observed as for the pure Ni_3Al single phase material. The presented experimental results [70] deviate somewhat from the results in [56], that were used to determine the parameters for the present model. The variation of the yield stress with temperature shows a maximum at 650 °C, whereas the data from [56] reveals a maximum at 850 °C, as was discussed in 3.3.2. This difference may be caused by a slightly different alloy composition, heat treatment or orientation or by the fact that, in [70], test bars were reused for several experiments with intermediate annealing treatments. As a result, the simulated tensile curves at lower temperatures ($< 750 \text{ °C}$) in this section will deviate somewhat from the experimental curves in [70].

The present model was used to simulate tests at 750 °C and a strain rate of 10^{-4} s^{-1} . The results are shown in Figure 3-17 for the two crystal orientations. The simulated curves for opposite loads (using $A = 0.3$, $B = 0.1$) are compared and as a reference, the results of a simulation in which the non-Schmid effects are neglected ($A = B = 0$) are

also shown. The behaviour corresponds to the experimentally observed trends: $T > C$ for $\langle 001 \rangle$ and $T < C$ for $\langle 011 \rangle$.

Moreover, the difference in yield stress (defined here as the stress at 0.2% plastic strain) between tension and compression in the order of 50 MPa, as reported by Allan [70] for $\langle 001 \rangle$ tests at 750 °C, corresponds quite reasonably to the difference of 30 MPa in Figure 3-17. The simulated asymmetry for the $\langle 011 \rangle$ orientation is considerably smaller than the experimentally observed value. However, the absolute value of the difference depends on the values of A and κ ; for which the pure Ni_3Al values from [68] have been used in the present simulations. The availability of a reliable set of experimental data would enable the determination of the appropriate values for the non-Schmid parameters for CMSX-4.

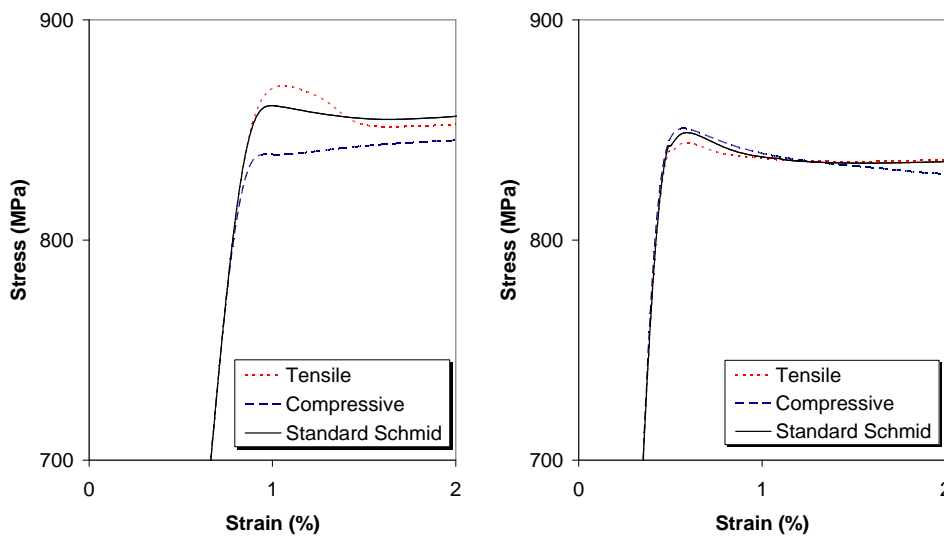


Figure 3-17 Simulated effect of the precipitate tension-compression asymmetry on the alloy uniaxial loading curve at 750 °C and a strain rate of 10^{-4} s^{-1} for two different orientations: left $\langle 001 \rangle$ and right $\langle 011 \rangle$.

Note that the observed difference is smaller than the tension-compression asymmetry found in single phase Ni_3Al . Ezz et al. [78] reported a difference in critical resolved shear stress in the order of 60 MPa, which corresponds to a difference in the uniaxial stress of about 150 MPa. The precipitate behaviour is therefore only partly observed in the alloy, as can be expected.

This is confirmed by the observation that both the simulations and the experiments [70] for the $\langle 111 \rangle$ orientation hardly show any tension-compression asymmetry. At this orientation the matrix cross slip mechanism (section 3.3) yields a significant increase of matrix slip, which reduces the influence of the precipitate behaviour considerably.

Recent numerical work on CMSX-4 by Choi et al. [79] also showed higher stresses at tensile loading (strain rate: 10^{-3} s^{-1}). However, in that work the magnitude of the tension-compression asymmetry was much smaller, because this was caused only by a geometric constraint effect imposed by the γ/γ' -microstructure. The precipitates were treated as an elastic medium and consequently the intrinsic tension-compression asymmetry of the Ni_3Al phase was neglected.

The anomalous increase of the precipitate flow stress up to the peak temperature is hardly visible in the superalloy behaviour, since the initial yielding of the alloy is associated with matrix slip and not with precipitate deformation. Therefore, the precipitate slip resistance is assumed to be constant here and the normal decrease of the yield stress beyond T_p is represented by the temperature dependence of the threshold stress τ_c as given by equation (3.18).

To summarize, the results in this section illustrate that the present model is able to correctly predict the observed trends in alloy tension-compression asymmetry.

3.7 Conclusions

Original modelling approaches for two specific aspects of Ni-base superalloy deformation behaviour are proposed in this work. Firstly, cube slip is modelled by incorporating a zig-zag cross slip mechanism into the constitutive relations for the matrix phase. A cross slip factor, based on the resolved shear stresses on the primary and secondary plane, is introduced that quantifies the amount of cross slip and therewith represents the orientation dependence of the cube slip. This formulation makes the inclusion of an additional set of cube slip systems superfluous. Secondly, a detailed precipitate phase constitutive model is established, which enables the simulation of the anomalous yield behaviour and other non-Schmid effects, like tension-compression asymmetry, in the superalloy mechanical behaviour. Dislocation density based formulations for the two precipitate deformation mechanisms, precipitate shearing and recovery climb, are proposed. Also, the cross slip mechanism and the associated splitting of partial dislocations, that are responsible for the anomalous yield behaviour, are incorporated in the model.

The formulations proposed here are implemented in a recently developed crystal plasticity framework [62] for single crystal Ni-base superalloys. One consistent set of model parameters for the commercial alloy CMSX-4 is determined from a database of experimental results. The model is shown to predict the material tensile response and creep behaviour for a range of temperatures and stress or strain rate levels. The incorporation of the cross slip mechanisms in matrix and precipitate results in an adequate simulation of the material orientation dependence and of the experimentally determined tension-compression asymmetry.

At present, the morphology of the microstructure is still assumed to remain unchanged during deformation, thereby neglecting the mechanism of rafting. Experimental work [48] has shown that precipitate coarsening is completed rapidly at temperatures above 950 °C and at proportionally longer times at lower temperatures. Consequently, the assumption of a fixed morphology still limits the application region of the present model to temperatures below 950 °C, but at lower temperatures the limitation with respect to strain level is relieved considerably. Extension of the model to include the rafting phenomenon is the subject of forthcoming work (see chapter 5).

Chapter 4

Damage model³

Abstract - *In this chapter a damage model for single crystal Ni-base superalloys is proposed that integrates time-dependent and cyclic damage into a generally applicable time-incremental damage rule. A criterion based on the Orowan stress is introduced to detect slip reversal on the microscopic level and the cyclic damage accumulation is quantified using the dislocation loop immobilization mechanism. Further, the interaction between cyclic and time-dependent damage accumulation is incorporated in the model. Implementation in a multiscale constitutive framework for Ni-base superalloys enables simulations for a wide range of loading conditions, showing adequate agreement with experimental results.*

4.1 Introduction

Nickel base superalloys are frequently used for critical components in gas turbines. Since these machines are applied as jet engines in aeroplanes and for power generation, structural integrity of their parts is critically important, both for safety and economic reasons. Therefore, gas turbine manufacturers as well as operators are eager to accurately assess the service life of their components, which is only possible if an accurate damage model is available.

Gas turbine components operate at high temperatures and under variable stresses, leading to a complex load history. This means that several failure modes are active, with creep and low cycle fatigue being the dominant mechanisms. To be able to assess the damage accumulation in these components, a combined creep-fatigue damage model should be used, which is capable of accounting for load histories that are considerably more complex than standard constant amplitude / constant temperature load sequences. The aim of the present work is to develop a model that enables to perform this task in a computationally efficient way and for a broad range of loading conditions.

³ This chapter is reproduced from: Tinga, T., Brekelmans, W. A. M. and Geers, M. G. D.; *Time-incremental creep-fatigue damage rule for single crystal Ni-base superalloys*; Materials Science and Engineering A, available online (2009), 1-9.

Ample research has been done in the field of damage modelling, based on either continuum damage mechanics or fracture mechanics models. The latter consider the initiation and propagation of discrete cracks in structures, whereas continuum damage mechanics disregards these discrete flaws and treats the material as a continuum in which the evolution of damage eventually leads to failure. The damage parameter may represent several failure mechanisms: Chaboche and Gallerneau [80] used damage parameters representing crack initiation, crack propagation, oxidation and creep damage, while Busso and co-workers [8,81,82] described the formation and growth of voids. For the small components under consideration, critical crack lengths are extremely small and the initiation of cracks completely dominates the service life [83]. For that reason, only continuum damage models will be considered here.

A damage rule can be formulated and applied in different ways. The first issue is whether or not the damage is incorporated in the thermo-mechanical constitutive description. In other words, does the accumulated damage affect the material behaviour or is it just treated as a post-processing quantity? The second issue is whether the damage evolution is defined as a time-incremental rule, where the damage rate is based on the actual values of the governing quantities, or that some cycle definition, or at least knowledge about the cycle shape / period, is required to calculate the damage.

As stated before, the aim of the present work is to develop a computationally efficient damage model that can be applied to any load history. The requirement of an efficient model implies the use of an uncoupled (post-processing based) damage rule. In that case, the analysis of one or a limited number of representative cycles can be applied to assess the time to failure. A coupled model would require the analysis of the complete load sequence, since the accumulation of damage in that case leads to a continuously changing material response. However, experimental programs [84] demonstrate that superalloys in general, and CMSX-4 in particular, do not show considerable cyclic softening before failure. This illustrates that, for this type of materials, damage evolution has a limited effect on the constitutive behaviour and that application of an uncoupled damage model is valid.

The fact that the model must be able to analyze any load sequence, also without a clear cycle definition, demands for a time-incremental damage rule, where the momentary values of the governing quantities (like stress, plastic strain rate) can be used to determine the damage rate. Time integration of this damage rate results in the damage accumulation in a certain period of time, without any precise knowledge of a cycle. Hence, for the present application, an uncoupled time-incremental damage rule appears to be the appropriate choice.

Classical fatigue life prediction models relate the life time to a single load parameter like stress [85] or strain range [86,87]. Several extensions to these original models have been proposed, taking into account the effects of mean stress, stress concentrations and environment [61,83,88,89]. Variable amplitude loading can be analyzed using a linear damage rule as proposed by Palmgren [90] and Miner [91]. Creep life models are in most cases based on the minimum creep rate as given by the classical Norton creep law and relate the creep rupture life to the hold time at a certain temperature [36]. Robinson [92] developed a time-based damage accumulation rule for creep equivalent to the Palmgren-Miner rule for fatigue.

To be incorporated into visco-plastic material models, some of the classical fatigue and creep life methods have been transformed into time-incremental damage rules [93,94]. For creep this is rather straightforward, due to the obvious time-dependence of creep damage accumulation. However, for cyclic damage this is less trivial, as will be discussed below. Multi-axiality effects on fatigue life have been incorporated into these damage rules on the basis of the critical plane approach [95-97]. This approach assumes that cracks initiate on the most severely loaded plane in a material, where the strains or stresses normal to those planes assist in crack propagation. For polycrystalline (isotropic) materials the plane normal to the maximum principal stress is often adopted to be the critical plane. Yeh and Krempl [97] also followed this approach in developing their damage rule, proposing the following evolution equation for the damage parameter D :

$$\dot{D} = L_f(\omega) \left| \frac{\dot{\epsilon}_p^s}{\dot{\epsilon}_f} \right|^n \left| \frac{\sigma_{eff}}{\sigma_f} \right|^m \left[1 + a \left(1 - \frac{\text{tr}(\boldsymbol{\sigma})}{\sigma_{eff}} \right) \right] \quad (4.1)$$

with L_f a non-negative function of the quantity $\omega = \dot{\epsilon}_p^n / \dot{\epsilon}_p^s$, $\text{tr}(\boldsymbol{\sigma})$ the trace of the stress tensor and σ_{eff} the Von Mises effective stress. The strain rates $\dot{\epsilon}_p^s$ and $\dot{\epsilon}_p^n$ are the maximum inelastic shear strain rate and normal strain rate on the critical plane, respectively. The orientation of the critical plane depends on the local stress tensor. The parameters $\dot{\epsilon}_f$, σ_f , n , m and a are material constants.

In a crystal plasticity framework for single crystal materials, it seems appropriate to use crystallographic slip planes as potential critical planes and slip system parameters like resolved shear stress and shear strain rate to calculate the damage evolution. Arakere [95,98] has shown that the fatigue life of single crystal Ni-base superalloys correlates quite well with the maximum value of the resolved shear stresses on all slip systems. However, it should be realized that, especially for symmetric loading conditions (e.g. $\langle 001 \rangle$), the deformation is more or less equally

spread over several (up to 8) equivalent slip systems. This means that none of the slip planes can be indicated unambiguously as the critical plane.

Levkovitch et al. [99,100] transferred the Yeh and Krempl [97] equation to a crystal plasticity formulation, resulting in a time-incremental damage rule for Ni-base superalloys. The evolution of the damage D is based on the resolved shear stress τ^α and slip rates $\dot{\gamma}^\alpha$ on all slip systems α according to

$$\dot{D} = \sum_{\alpha} \left(\frac{|\tau^\alpha|}{s_{oct}} \right)^{m_{oct}} \left(\frac{|\dot{\gamma}^\alpha|}{\dot{\gamma}_{oct}} \right)^{n_{oct}} \dot{\gamma}_{oct} + \sum_{\alpha} \left(\frac{|\tau^\alpha|}{s_{cub}} \right)^{m_{cub}} \left(\frac{|\dot{\gamma}^\alpha|}{\dot{\gamma}_{cub}} \right)^{n_{cub}} \dot{\gamma}_{cub} \quad (4.2)$$

taking into account both octahedral $\{111\}\langle 011 \rangle$ and cubic $\{001\}\langle 011 \rangle$ slip systems, as indicated by the subscripts *oct* and *cub*, respectively. The two sets of parameters m , n , s and $\dot{\gamma}$ have to be determined from experiments.

Although several of the reported time-incremental damage rules [97,99,100] are applied to model low cycle fatigue damage, there is a fundamental problem with calculating cyclic damage in a time-incremental manner. The reason is that effectively not the time but rather the discrete number of cycles is governing the damage accumulation. Since existing time-incremental damage rules do not consider any load reversal, they are principally unable to predict cyclic damage correctly. Yeh and Krempl [97] recognized the difference between time-dependent and cyclic damage and calculated the damage (rate) as a sum of creep and fatigue damage. However, also the cyclic damage is calculated in a time-incremental way. Levkovich et al. [99,100] modified this model to make it suitable for a crystal plasticity approach. However, they only adopted the fatigue part of the Yeh and Krempl model and neglected the creep part. The model parameters were determined such that the cyclic damage is calculated sufficiently accurate for a set of experiments. Consequently, tests with considerable time-dependent (creep) damage are simulated inaccurately, even though only relatively short hold times (< 120 s) and high strain rates were applied. This is visualized in Figure 4-1, which illustrates that the tests with a relatively large cycle time and the pure cyclic tests with a short cycle time reveal quite different trends within the band of results for the number N_f of cycles to failure. In this work [99,100], both the cyclic damage and the time-dependent damage are covered in a single time-incremental damage rule. By neglecting the extreme cases (long hold times, slow cyclic tests and very fast cyclic tests) a set of parameters can be determined that just covers all the conditions within the usual factor-2 scatter band. However, Figure 4-1 shows that the cyclic damage (here based on time) is overestimated, while the time-dependent damage is underestimated, with curves for tests with long cycle times deviating towards long

life times as a result. In other words, the cyclic and time-dependent mechanisms are related to time quite differently, but an average value is used, since only one mechanism is available in the model. This confirms that it is practically impossible to predict the total damage using a purely time-incremental damage rule, especially when extreme conditions like long hold time tests or even creep tests together with fast cyclic tests are to be analyzed.

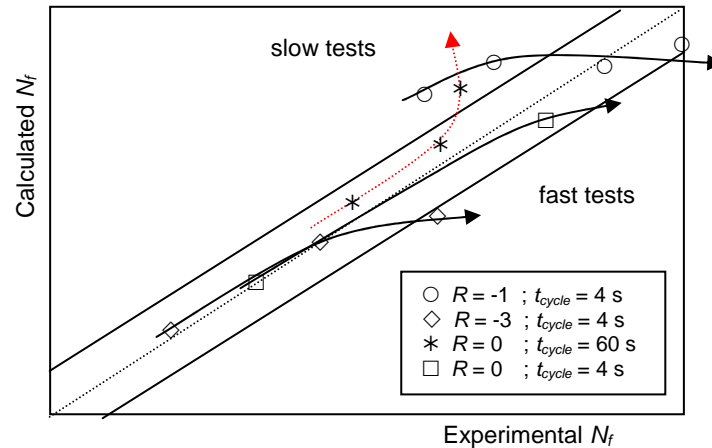


Figure 4-1 Trends in life assessment plots using time-incremental damage rules. Four sets of data from [99] are plotted. The two sets of arrows indicate the different trends between time-dependent (slow cycling or hold times) and cyclic damage (fast cycling).

The foregoing discussion indicates that it is not feasible to calculate the cyclic damage in a time-incremental way, since not the time but the discrete number of cycles is governing the damage accumulation. There are two ways to accommodate this problem:

- Incorporation of the physical mechanism that represents the cyclic damage into the constitutive model. As will be discussed in section 4.2, this mechanism can be identified as the immobilization of dislocation loops which reduces the deformability of the material. The evolution of the cyclic damage in time will affect the deformation behaviour of the material, which can be used to calculate the damage evolution for any load sequence. However, in the resulting coupled model the damage accumulation will affect the material response. As a result, a life assessment now requires the analysis of the complete load sequence instead of only a limited number of representative cycles. A recent example pursuing this approach is presented in the work by Desmorat et al. [101]. Fedelich [23]

incorporated this immobilization mechanism in a crystal plasticity model for Ni-base superalloys, but only used it to calculate the deformation and did not extend it to a damage description. The densities of deposited interfacial dislocation segments, as well as the immobilized fraction thereof, constitute an important set of state variables for this mechanism.

- Separation of the time-dependent and cyclic damage accumulation into two damage rules. The time-dependent damage can be calculated with a regular time-incremental rule, while the cyclic damage accumulation must be proportional to the number of cycles or load reversals. There are two options available to do this:
 - use well-defined cycles to calculate the damage. Ample fatigue models have been developed, which relate the number of cycles to failure (N_f) to the applied stress range [85] or strain range [86,87] and include factors to correct for the stress ratio R , temperature, etc. The calculated damage per cycle is then multiplied with the number of cycles [90,91] to obtain the total damage. This method only works for regular cyclic load sequences and a known number of analyzed cycles.
 - use a micro-mechanical criterion to detect a relevant load reversal and quantify the cyclic damage accumulation using the local quantities related to that criterion. This method can be applied for any complex load sequence and does not require knowledge of the number of cycles.

This final option is in fact a compromise between a fully coupled time-incremental damage rule that includes the physical damage mechanism, and the traditional uncoupled cycle-based damage rules. Local micro-mechanical quantities are used to determine the cyclic damage in an uncoupled way (i.e. post-processing), but the cycle is specified during the analysis.

In the present paper, the above suggested approach is followed to propose a new damage model that integrates time-dependent and cyclic damage into a generally applicable time-incremental damage rule. An original criterion based on the Orowan stress is introduced to detect slip reversal on the microscopic level and the cyclic damage accumulation is quantified using the dislocation loop immobilization mechanism. Further, the interaction between cyclic and time-dependent damage accumulation is incorporated in the model. Implementation in a multiscale constitutive framework for Ni-base superalloys enables to perform simulations for a wide range of loading conditions, revealing an adequate agreement with experimental results.

The next section discusses the cyclic and creep damage mechanism on the microscopic level in detail. In section 4.3, the new damage model is proposed and section 4.4 addresses the interaction between creep and fatigue damage. The

implementation in a multiscale constitutive framework is described in section 4.5. Simulation results are presented and compared to experimental results in section 4.6 and, finally, section 4.7 forwards some concluding remarks.

4.2 Micro level damage mechanisms

In this section, the physical mechanisms of both cyclic and time-dependent damage development are described. This will be done on the microstructural level, taking into account the role of dislocations and the typical γ/γ' microstructure. This two phase microstructure consists of a Ni matrix (γ -phase) containing a large volume fraction of cubic Ni_3Al precipitates (γ' -phase). The two phases share a coherent interface with only a small misfit due to a slight difference in lattice constants. In the face-centred cubic (FCC) material of both phases, a set of 12 slip systems will carry the plastic deformation.

Recently, the authors have presented a multiscale model [62] that simulates the mechanical response of the material. On the material point level the microstructure is represented by a unit cell containing 16 regions (see Figure 4-2): one precipitate (γ') region, three γ -matrix channel regions (γ_f) with different orientations, and six pairs of interface regions containing the γ/γ' interfaces. The interface between the two different phases plays an important role in the mechanical behaviour of the material. Therefore, special interface regions were included in the model to take into account the processes that take place at the γ/γ' -interfaces. Consequently, each phase in the two-phase material, either a precipitate or a matrix channel, is represented by two types of regions in the unit cell. The first type represents the behaviour of the pure phase (excluding interfaces) and in the second type all short-range interface effects, including dislocation induced back stress and interaction with other phases, are incorporated.

The formation and growth of micro voids in the material play a prominent role in damage accumulation under creep conditions. Metallographic inspection of crept specimens by Moss et al. [36] revealed that cracks initiated from pre-existing micro pores originating from the casting process. Also new micro cavities were formed at the γ/γ' -interfaces. Reed et al. [102] observed that at 1050 °C TCP-particles (= topologically close packed) acted as initiation sites for void formation during creep. These voids, as well as casting pores, elongated and eventually coalesced just prior to failure during creep tests.

Another important mechanism that is active under creep conditions is the microstructural coarsening effect known as rafting. At temperatures above 850 °C combined with certain externally applied stresses, the initially cuboidal precipitates

transform into elongated plates [103-105]. Since also the morphology of the matrix phase, which bears the majority of the plastic deformation, changes, there is a significant effect on the material mechanical response.

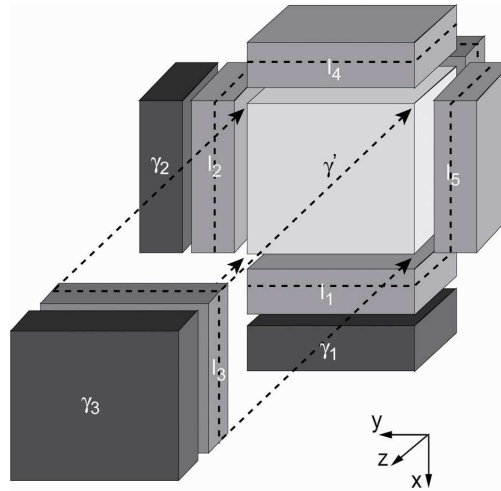


Figure 4-2 Overview of the multiphase unit cell used to calculate the mechanical response of the material.

On the micro-mechanical level, fatigue damage is attributed to irreversibility in the slip mechanism: plastic deformation is accommodated by lattice planes slipping along each other, facilitated by dislocations moving along the slip planes. Upon load reversal the dislocations should glide in the opposite direction, but this is not always possible. Part of the dislocations are immobilized and cannot move backward, which means that other planes have to take over. This process eventually, after a large number of cycles, leads to accumulation of damage (implying lack of deformability) and finally results in the initiation of cracks (leading to failure).

This phenomenon is discussed by several authors. Shyam and Milligan [106] studied the effect of slip irreversibility on the fatigue crack propagation threshold. In their work, the irreversibility is ascribed to the egress of dislocations at the free surface. Fedelich [23] presented a microstructural model for Ni-base superalloys and introduced some form of slip immobilization into the constitutive description. This was used to adequately describe the amount of reverse slip that occurs after a reversal of the externally applied load. Also the generated internal back stresses play a role in this reverse slip process. A difference was made between forward and backward slip. During forward slip, a dislocation line is forced in between two precipitates. This only

happens if the effective stress, defined as the net effect of externally applied and internal stresses (on the slip plane in slip direction), exceeds the Orowan threshold ($\tau_{eff} > \tau^{or}$). This threshold value is determined by the precipitate spacing d according to

$$\tau^{or} = \alpha \frac{\mu b}{d} \quad (4.3)$$

where μ is the shear modulus, b the Burgers vector and α a dimensionless constant related to the dislocation core radius. Following [62], $\alpha = 0.85$ is used here. Moreover, the trailing segments of the loops are deposited onto the γ/γ' -interfaces, see Figure 4-3.

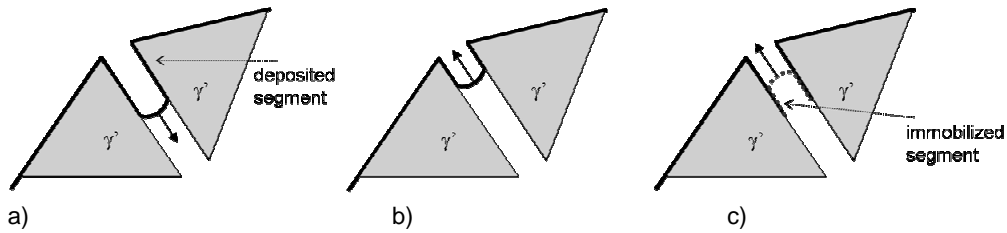


Figure 4-3 Dislocation line forced into the γ -channel in between two γ' -precipitates; a) segments of the line are deposited onto the γ/γ' -interfaces; b) on reduction of the applied stress the loop moves backward; c) the interfacial segments are immobilized and backward slip is only possible by bowing out in the opposite sense, thereby depositing new segments on the interface .

When the applied load is reduced, ideally the loop would shrink back due to the dislocation line tension and the deposited segments would disappear. However, this only happens when nothing hinders the backward glide of the loop. It also means that backward slip occurs as soon as the effective stress drops below the Orowan threshold again, $\tau_{eff} < \tau^{or}$ (and not when $\tau_{eff} < -\tau^{or}$ as predicted by most plasticity models). The line tension of the dislocation then exceeds the effective stress and causes slip in the opposite direction. However, in practice there will be obstacles for the backward glide, which makes the velocity of backwards moving dislocations different from their forward velocity. The following mechanisms hinder the backward motion:

- bulk material loop immobilization: a part of the moving dislocation loops is immobilized caused by reactions with other loops
- immobilization of the interfacial segments: the segments deposited onto the γ/γ' -interfaces are immobilized and prevent the complete loop from moving backwards.

Possible mechanisms are:

- the interfacial segments react with segments of other slip systems and form networks on the γ/γ' -interfaces

- some of the segments locally affect the misfit, resulting in loss of coherency
- the interfacial segments can climb or cross slip, thus leaving the original slip plane

In all these cases the interfacial segments are immobilized and hence backward slip is more difficult than the preceding forward slip

Note that the first of these two mechanisms occurs in any material, but the second mechanism is specific for the typical two-phase (γ/γ') microstructure of superalloys. Also the reversal of slip at the Orowan stress is typical for these (precipitation strengthened) materials, since in ordinary materials the reversal would take place at zero stress.

This same mechanism, until now only used to describe reverse flow [23], is expected to play a role in cyclic damage accumulation as well. In an ideal material, any dislocation moving in one direction would be able to move backwards upon load removal and no damage would be accumulated, see Figure 4-4. However, the immobilization process discussed before gradually decreases the deformability of the material, which means that damage is accumulated.

Further, the immobilization process can be regarded as a combined *isotropic* and *kinematic* hardening effect. Each time an interfacial segment is immobilized, the resistance to dislocations moving in the channel in both directions will increase (isotropic hardening). Moreover, the deposited segments will contribute to the internal back stress [62], where the sign of this contribution depends on the direction of the dislocation line vector. The signed back stress provides a kinematic effect.

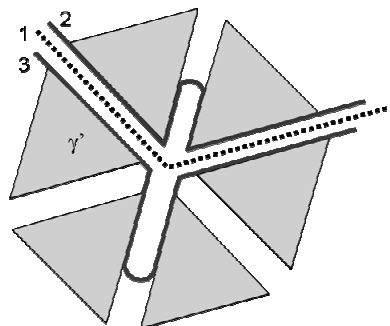


Figure 4-4 Schematic representation of a dislocation line moving on a $\{111\}$ plane in the matrix phase. In an ideal case a dislocation line (1) would be forced in between two precipitates (2) by an applied load. Upon removal of the load, the line would shrink back to its original location (1). Application of an opposite force will push the line in between two other precipitates (3). Without any immobilization this process can last infinitely long.

To be able to use the immobilization mechanism to predict the damage accumulation, the amount of immobilization must be quantified. The damage model proposed in the next section is implemented in a multiscale constitutive framework [62] whereby characteristic internal variables, like slip rate and resolved shear stress, are here used to quantify the damage.

4.3 Proposed damage model

Following the discussion in the introduction of this paper, the proposed damage model contains both a time-dependent and cyclic damage contribution. For the time-dependent part the model as presented by Levkovitch et al. [99,100] is used. Note that Levkovitch et al. regarded this as a fatigue damage model, while in the present approach it is used as a time-dependent creep damage model. The creep damage accumulation rate \dot{D}_i^{cr} in each of the three matrix regions ($i = 1, 2, 3$) of the unit cell (Figure 4-2) is therefore defined as

$$\dot{D}_i^{cr} = \sum_{\alpha=1}^{12} \dot{D}_{cr}^{\alpha} = \sum_{\alpha=1}^{12} \left(\frac{|\tau^{\alpha}|}{s} \right)^{m_c} \left(\frac{|\dot{\gamma}^{\alpha}|}{\dot{\gamma}_{0,c}} \right)^{n_c} \quad (4.4)$$

where the damage rate is determined by the values of the resolved shear stress (τ^{α}) and slip rate ($\dot{\gamma}^{\alpha}$) on the activated slip systems (α). The reference stress s is only used to make the first factor dimensionless, so its value can be taken arbitrarily, while the parameters m_c , n_c , and $\dot{\gamma}_{0,c}$ have to be determined from experiments. Since a temperature dependence of the slip rate is included in the constitutive framework, no separate temperature dependence of the damage rate is required here. This formulation represents, in a phenomenological way, the mechanism of void formation and growth, as discussed in the previous section. Note that in the present work only the technologically interesting $\langle 001 \rangle$ orientation of the material is considered, which means that the cubic slip systems can be neglected.

Cyclic damage is time-independent and fully depends on the applied cyclic load and resulting material response. Given the lack of a precise definition of a cycle in the load sequence, the forward and backward slip mechanism discussed in the previous section are used here to quantify the cyclic damage accumulation during a certain part of the load sequence in the following way:

1. count the (discrete) number of (relevant) load reversals using the criterion:

$$\begin{aligned} \text{start of cycle : } & \left| \tau_{eff}^{\alpha} \right| > \tau^{or} \\ \text{end of cycle : } & \left| \tau_{eff}^{\alpha} \right| < \tau^{or} \end{aligned} \quad (4.5)$$

2. quantify the fatigue (cyclic) damage contribution of each slip reversal according to

$$\Delta D_i^{fat} = \sum_{\alpha=1}^{12} \Delta D_{fat}^{\alpha} \quad (4.6)$$

It is thus assumed that damage is accumulated at each slip reversal, i.e. when forward slip is followed by backward slip. In a cycle also containing a compressive part (e.g. $R = -1$), there can be two cyclic damage contributions during one load cycle, depending on the magnitude of the applied load.

For the quantification of the fatigue damage, several internal variables tend to be physically relevant. They will be discussed here and the appropriate quantities will be selected.

- Total dislocation density (SSD + GND), either on the present slip system or on all other slip systems: a higher dislocation density on the present slip system will increase the probability of a reaction of the current loop with other loops (*bulk mechanism*). A higher dislocation density on other slip systems will increase the probability of network formation (*interface mechanism*). However, the SSD densities stabilize rather quickly during a load sequence, while the present damage model particularly applies to a stabilized cycle. In that case, the dislocation densities are not very sensitive to differences in loading conditions, which makes them less suitable as a damage quantifier.
- GND density on the present slip system: represents the *effective* number of deposited interfacial dislocation segments. The indication *effective* reflects that it is the difference between deposited segments by channel filling and removed segments by climb or shearing, which is necessary to maintain the lattice compatibility between the two phases. The number of segments that has been deposited can therefore be much larger, so the GND density is not an adequate damage quantifier.
- climb rate: a high climb rate will favour the immobilization of dislocation loops (*interface mechanism*), but in that case also the time is important. The climb rate is defined in the constitutive model as

$$\dot{\gamma}^{\alpha} = C \left| \tau_{eff}^{\alpha} \right| \rho_{GND}^{\alpha} \exp\left(\frac{-Q^c}{RT}\right) \quad (4.7)$$

with ρ_{GND}^{α} the GND density, T the absolute temperature and C and Q^c model parameters. The climb rate is hardly sensitive to loading conditions like stress and strain rate, but definitely sensitive to temperature. Therefore, it will be used to model the temperature dependence in the damage rule.

- effective resolved shear stress: a higher τ^{eff} will cause more slip (either carried by a larger number of dislocations or resulting in larger deposited interfacial segments) and hence, assuming that the fraction of the segments that is immobilized is rather constant, the amount of immobilized dislocations will be higher (*interface + bulk mechanism*). Therefore, the effective resolved shear stress appears to be a valid variable to quantify the damage.
- slip rate: following the same reasoning as for the resolved shear stress, a higher slip rate means that the number of moving dislocations is larger, which increases the number of immobilized loops (*interface + bulk mechanism*). Also the slip rate is a suitable damage quantifier.

From these considerations, the following cyclic damage rule is proposed

$$\Delta D_i^{fat} = \sum_{\alpha=1}^{12} \Delta D_{fat}^{\alpha} = \sum_{\alpha=1}^{12} \left(\frac{|\tau_{max}^{\alpha}|}{\tau_{ref}} \right)^{m_{fat}} \left(\frac{|\dot{\gamma}_{max}^{\alpha}|}{\dot{\gamma}_{0,fat}} \right)^{n_{fat}} \exp\left(\frac{-Q^c}{RT}\right) \quad (4.8)$$

where τ_{max}^{α} and $\dot{\gamma}_{max}^{\alpha}$ are the *maximum* values of resolved shear stress and slip rate during the “cycle” and the exponential term represents the temperature dependence of the climb mechanism. The reference stress τ_{ref} is again used to make the first factor dimensionless and the parameters m_{fat} , n_{fat} and $\dot{\gamma}_{0,fat}$ have to be determined from experiments.

Finally, the cyclic and time-dependent damage contributions are added to obtain the total damage increase during a time increment Δt

$$\Delta D_i = \dot{D}_i^{cr} \Delta t + \Delta D_i^{fat} \quad (4.9)$$

During a transient analysis, the time-dependent damage contributes every time step, while the cyclic damage contribution is only non-zero at the time step in which the end of a cycle is detected, using the second criterion in (5).

4.4 Creep – fatigue interaction

Typical loading conditions in gas turbine components, i.e. high temperatures in combination with variable stresses, cause simultaneous accumulation of time-dependent (creep) and cyclic (fatigue) damage. The relative importance of either mechanism is determined by the specific loading condition. In this section the relation between the two mechanisms is illustrated and the creep-fatigue interaction is discussed.

To study the interaction between cyclic and time-dependent damage, a set of strain-controlled low cycle fatigue (LCF) experiments [84] has been analyzed. In these experiments, a constant amplitude, fully reversed ($R = -1$) cyclic deformation (see Figure

4-5a) is applied until the test bar fails. The differences in applied strain range ($\Delta\epsilon_{tot}$), varying from 1.15 % to 2.20 %, yield different numbers of cycles to failure. Moreover, the cycle time (t_{cycle}) is varied by using tests at different strain rates (see Figure 4-5b) and hold times (see Figure 4-5c).

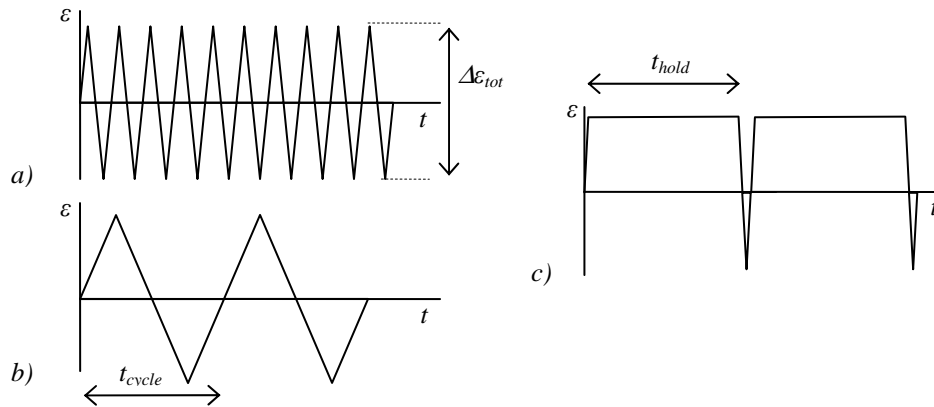


Figure 4-5 Schematic overview of different load sequences; a) high strain rate; b) low strain rate; c) cycle with hold time.

The relation between cyclic and time-dependent damage is illustrated by plotting the time to failure versus the number of cycles to failure for all these experiments, see Figure 4-6a. This figure shows the results for five sets of experiments which differ in time-per-cycle, as caused by differences in applied strain rates or hold times. The different life times within the sets are due to the different applied strain ranges.

This plot provides insight in the relative importance of cyclic and time-dependent damage. For the experiments with a long time-per-cycle the number of cycles to failure is rather limited and time-dependent damage dominates. On the other hand, for the tests with short cycle times the number of cycles to failure is high, but the total time to failure is small. This means that for these tests the cyclic damage will dominate. The limiting cases are pure creep tests (no cycles, represented by the vertical axis in Figure 4-6) and very fast cyclic tests (very small time to failure, horizontal axis).

Departing from the results in Figure 4-6a, the effect of a variation in cycle time for tests with similar applied strain ranges can be analysed. This is shown in Figure 4-6b, where only the seven tests with an applied strain range between 1.7% and 1.9% are plotted. Assuming that the cyclic fatigue damage per cycle in these tests is comparable, the effect of time-dependent creep damage becomes clear. For the tests with longer cycle times, time-dependent damage also contributes to the total damage

and consequently the number of cycles to failure decreases. The solid line in Figure 4-6b represents this trend. Many damage models (e.g. [61]) assume that both damage contributions are independent and can be added linearly, based on the classical rules by Palmgren-Miner [90,91] and Robinson [92]. This would result in a straight line connecting the loci of the limiting cases (dashed line). It is clear that the real trend deviates from this line, which means that there is a significant interaction and that the two damage mechanisms are not independent. The presence of cyclic damage increases the creep damage rate and vice versa.

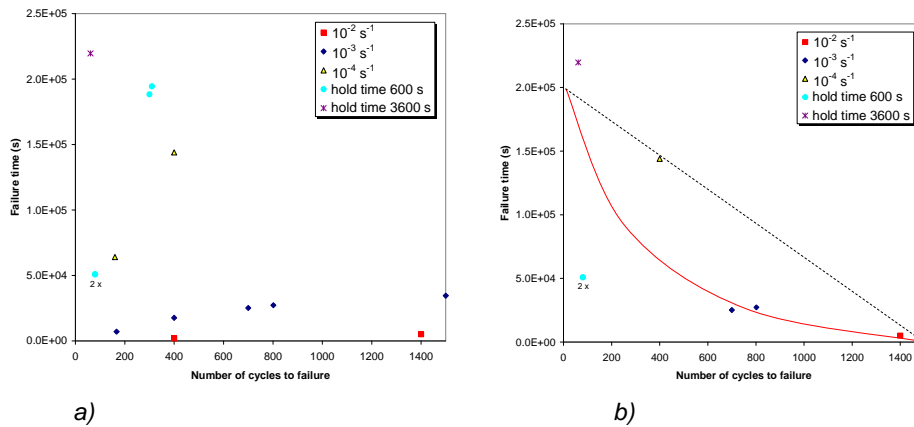


Figure 4-6 Failure time vs. number of cycles to failure for a set of low cycle fatigue experiments at 850 °C with different cycle times, caused by differences in strain rates and hold times, and different applied strain ranges. a) all tests; b) tests with similar amounts of fatigue damage per cycle ($\Delta\epsilon_{tot} = 1.7 - 1.9\%$). The solid line shows the trend according to the experimental results, while the dashed line represents the (theoretical) linear interaction.

The physical mechanisms of creep and fatigue failure in Ni-base superalloys have been discussed in section 4.2. Creep failure is attributed to the formation, growth and coalescence of voids in the material, whereas fatigue failure is related to the immobilization of dislocation segments resulting in irreversibility of slip. The interaction of the two mechanisms, that is observed in Figure 4-6b, may be explained as follows. Voids that develop in the material during creep will provide additional internal free surface. This gives the opportunity for parts of dislocation lines to escape and thereby enhances the irreversibility of slip. The other way around, immobilized dislocation pile-ups created by cyclic loading will favour the formation and growth of voids. In this way, presence of one type of damage affects the amount and evolution rate of the other type of damage, resulting in the observed interaction.

The creep-fatigue interaction can be incorporated in the damage model by replacing the linear interaction between fatigue and creep damage (4.9) by a more sophisticated damage rule. The following rule is proposed here

$$D_i^{tot} = D_i^{cr} + D_i^{fat} + A_{int} \frac{D_i^{cr} D_i^{fat}}{D_i^{cr} + D_i^{fat}} \quad (4.10)$$

where the last contribution in the right-hand side represents the creep-fatigue interaction. For the relevant material, CMSX-4 at 850 °C, a value of 3.5 for the interaction coefficient A_{int} results in an adequate agreement between the simulated and experimental results, as is illustrated in Figure 4-7. This interaction has been incorporated in the present damage model.

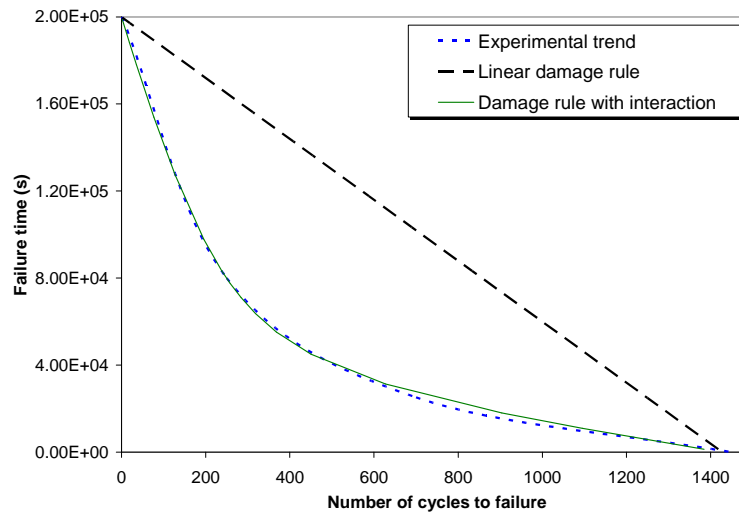


Figure 4-7 Creep-fatigue interaction in CMSX-4 at 850 °C.

4.5 Implementation

The proposed damage model has been implemented in a recently developed multiscale constitutive framework [62]. From experimental work [80,83,107-111] it is known that crack initiation is controlled by local plasticity in the vicinity of stress concentrators like casting pores or carbides. Since plastic deformation in Ni-base superalloys predominantly occurs in the matrix phase of the material, plastic slip in this phase will control the initiation and evolution of damage. Implementing the damage model in the multiscale framework offers the possibility to calculate the damage evolution in the matrix phase separately. This means that, instead of using the macroscopic (average)

stress and strain, the specific values for the different matrix channels can be used, including the effects of misfit and internal back stresses.

In the present approach, see Figure 4-2, the bulk material behaviour and the interface effects of the matrix phase are represented by the matrix channel (γ_i) and the matrix side of the interface regions (I_i^m) respectively. Therefore, the effective stress used in the damage law is obtained by (volume) averaging the stress values of the matrix and its corresponding interface regions:

$$\sigma_{eff,i}^m = f^{I_i^m} \sigma^{I_i^m} + f^{\gamma_i} \sigma^{\gamma_i} \quad i = 1, 2, 3 \quad (4.11)$$

where $f^{I_i^m}$ and f^{γ_i} are the respective volume fractions. In the same way, the representative slip rate $\dot{\gamma}_{m,i}^\alpha$ is obtained. The damage parameter can be transferred to the macro level (D) by taking the maximum value of the three individual matrix regions i

$$D = \max(D_i) \quad i = 1, 2, 3 \quad (4.12)$$

Application of the proposed damage model in a multiscale framework offers the possibility to use the local loading conditions of the region where the damage actually initiates (i.e. the matrix phase). This is an obvious benefit compared to the conventional macroscopic single crystal plasticity models developed for superalloys [2,4,10,11,12], where the material is treated as a homogeneous single phase and consequently such local information is not available. As it can be observed in Figure 4-8, the stress levels in the individual phases can differ significantly from the macroscopic value, especially for the matrix channels. This difference is caused by two effects:

- plastic deformation varies across the different regions, resulting in a redistribution of the applied stress
- the lattice misfit between the γ - and γ' -phase causes misfit stresses in both phases: tensile stresses in the precipitate and compressive stresses in the matrix channels. The relative size of these stresses varies, since
 - the direction of the misfit stress is related to the orientation of the matrix channels. This is due to the fact that the misfit is only acting in the plane of the interface, which for some regions is normal to the applied load and for others parallel.
 - the magnitude of the misfit stress is independent of the applied load: for low applied stresses the effect will be relatively large, whereas for higher loads it will be less important.

Due to these effects, the matrix phase stresses are not a fixed fraction of the macroscopic stress and therefore cannot be directly derived from the macroscopic stress tensor. Consequently, a classical single phase crystal plasticity model will not be

able to grasp these effects correctly and using a multiscale model offers a significant benefit.

To calculate the damage accumulation during a cyclic test, the implementation of the time-incremental damage rule can be activated in parallel with the deformation analysis. It should be emphasized here that the calculated damage is not used to update the constitutive behaviour, as was discussed in the introduction. The end of life is reached when the damage parameter attains the value one.

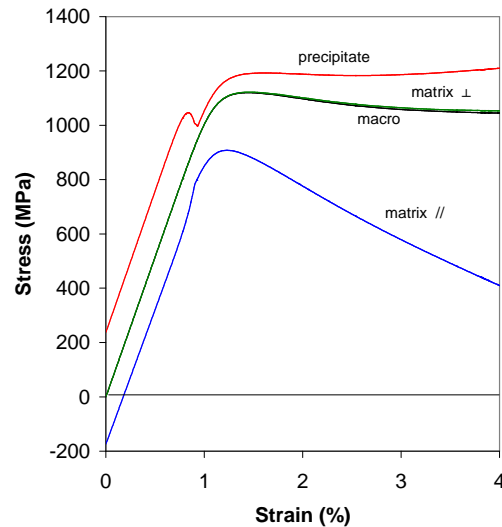


Figure 4-8 Comparison of the macroscopic stresses and the micro level effective stresses in the material phases during a tensile test at 800 °C and a strain rate of 10^{-3} s^{-1} . In all cases the stress component in the direction of the applied load is plotted. The symbols \perp and $//$ denote the matrix regions oriented normal and parallel to the applied load, respectively.

However, since the cyclic stress-strain curve stabilizes quickly, normally within about five cycles, it can be assumed that the damage evolution during the 5th cycle is representative for the remaining life.

To verify this, the change of damage accumulation per cycle (normalized with the accumulation in the first cycle) is shown in Figure 4-9 for different applied strain ranges and different cycle times (caused by differences in strain rate and hold time). The results show that the first cycle is not representative at all, but that for most loading conditions the damage accumulation stabilizes after five cycles. Assuming that the damage accumulates linearly from cycle to cycle, only the damage accumulation during the 5th cycle is calculated and inverting this value yields the number of cycles to failure. In this way, the computational efficiency of the analysis is improved considerably.

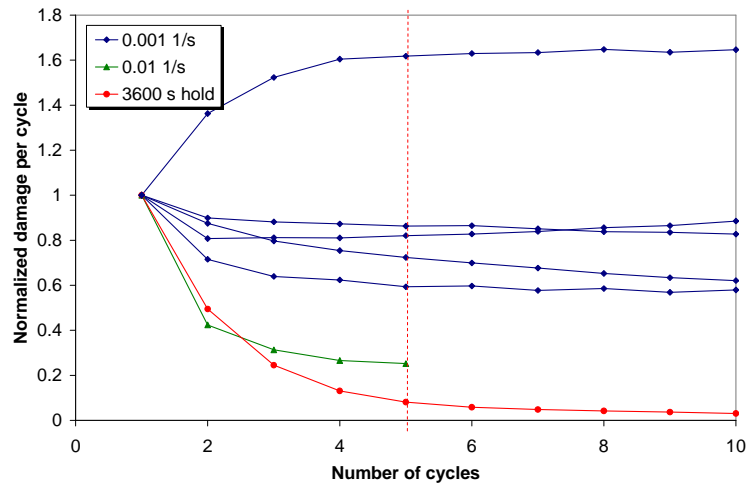


Figure 4-9 Evolution of the normalized damage accumulation per cycle for different applied strain ranges and cycle times.

Simulations have been performed for various conditions and the damage model parameters have been determined by fitting the results to experimental data obtained from cyclic tests in the 850 – 950 °C temperature range. The parameter Q^c is part of the constitutive framework and its value has been determined from monotonic (tensile and creep) experiments at temperatures ranging from 750 to 1000 °C. The obtained values for the model parameters are shown in Table 4-1 below.

Table 4-1 Damage model parameter values.

m_{fat}	1	m_c	2
n_{fat}	0.4	n_c	0.3
$\dot{\gamma}_{0,fat}$	$2.33 \cdot 10^{-2} s^{-1}$	$\dot{\gamma}_{0,c}$	$3.11 \cdot 10^5 s^{-1}$
C	$8.9 \cdot 10^{-18} m^2 s kg^{-1}$	Q^c	85 kJ mol ⁻¹
A_{int}	3.5		

4.6 Results

Simulations are performed for a number of LCF tests at different conditions. The reference case temperature is 850 °C, the strain rate is $10^{-3} s^{-1}$ and the stress ratio R equals -1. The applied total strain range is varied from 1.15% to 2 %, resulting in 10^2 to 10^4 cycles to failure. Then the conditions are varied, specifically the test temperature (950 °C), applied strain rate (10^{-4} and $10^{-2} s^{-1}$) and stress ratio ($R = 0.05$ and 0.5) are varied and tests with hold times (600 and 3600 s) are simulated. The calculated

number of cycles to failure are plotted versus the experimental number of cycles to failure in Figure 4-10.

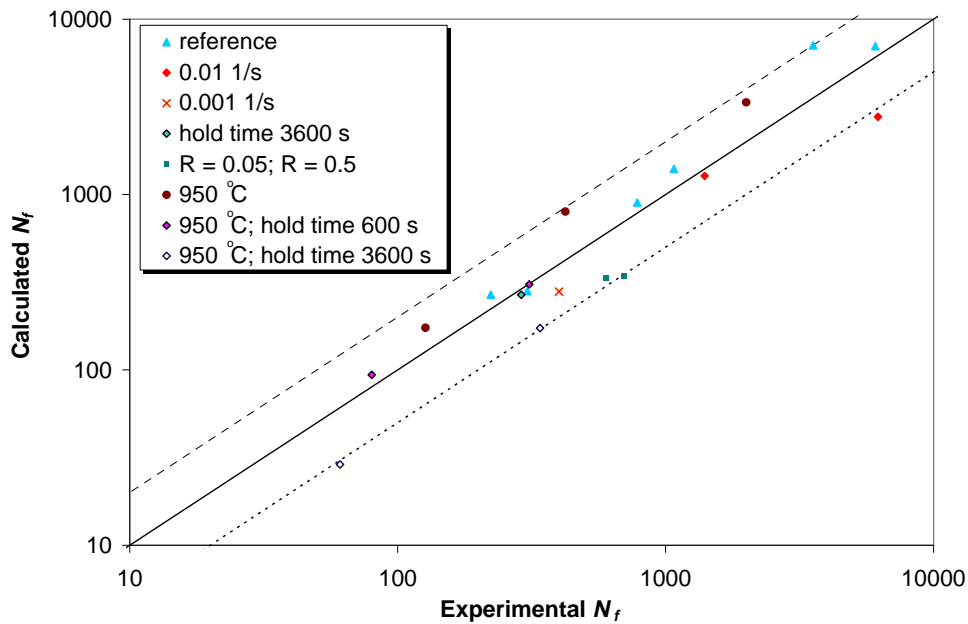


Figure 4-10 Calculated versus experimentally determined number of cycles to failure for LCF tests at different conditions. The reference case temperature is 850 °C, the strain rate is 10^{-3} s^{-1} and the stress ratio R equals -1. Variations to this reference case are indicated.

Figure 4-10 shows that the proposed model predicts numbers of cycles to failure that are within a factor two of the experimentally determined numbers for a broad range of conditions, where both fatigue dominated and creep dominated conditions are covered.

An extreme case of a cyclic test with an infinite hold time is a pure creep test. Ideally, the model should be able to also predict the rupture life for such a test. However, there are two complicating aspects that obstruct such a calculation. Firstly, during long term creep tests, the process of rafting in most cases plays an important role in the failure process, however rafting is not included in the present model. For the cyclic hold time tests in Figure 4-10, the amount of creep is still rather limited and rafting is not very significant. Secondly, the assumption was made that the damage accumulates linearly from cycle to cycle. At temperatures in the 850 – 950 °C range, creep curves contain almost exclusively tertiary regimes, in which the creep rate is continuously increasing. The damage accumulation is therefore not linear, which makes the damage model unsuitable for pure creep tests. The only way to accurately

assess the creep damage is therefore to simulate the complete creep curve, which is computationally less efficient.

For the fully reversed ($R = -1$) LCF tests with hold times the situation is different. Firstly, the creep strain that develops during the hold time in one (e.g. the compressive) part of the cycle is to a large extent removed by the plastic deformation in the opposite (e.g. tensile) part of the cycle. This is illustrated by the stress – strain loops for an arbitrary hold time experiment in Figure 4-11. Each cycle, the creep deformation is thus reduced to a minimal value by the plastic deformation, which means that the tertiary regime is never reached. Secondly, the LCF experiments are strain-controlled, contrary to the stress-controlled creep tests, which means that during the hold time the stress quickly relaxes (see Figure 4-11) and the creep rate reduces considerably. These two aspects ensure that the proposed method is valid for LCF tests with hold times, in spite of the fact that pure creep tests are not yet at reach with this model.

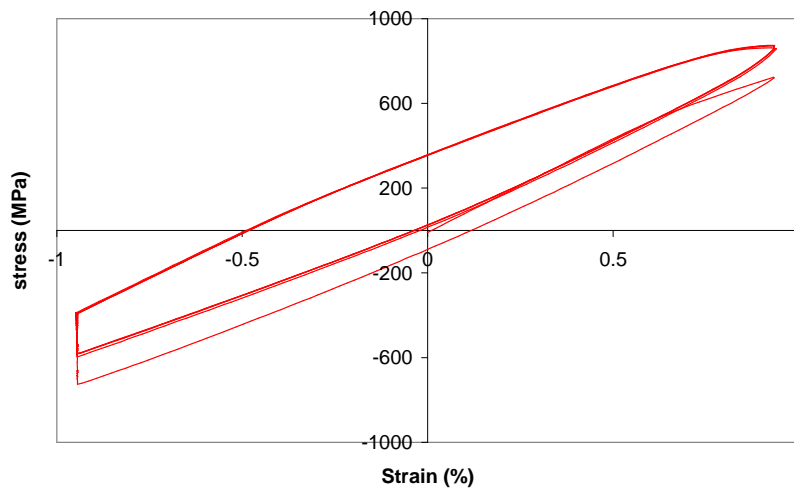


Figure 4-11 First five stress-strain loops of a strain-controlled low cycle fatigue test with a compressive hold time of 60 minutes.

4.7 Conclusion

A critical review of existing damage models and a detailed analysis of the physical mechanisms underlying damage formation in single crystal Ni-based superalloys resulted in the development of a new damage model for this particular material. The proposed formulation contains the following original aspects:

- the model integrates time-dependent (creep) and cyclic (fatigue) damage into a generally applicable time-incremental damage rule;
- to incorporate the cycle-dependence of the fatigue damage into the time-dependent damage rule, a criterion based on the Orowan stress is proposed to detect slip reversal on the microscopic level;
- the cyclic damage accumulation is quantified using the internal variables related to the dislocation loop immobilization mechanism;
- the interaction between cyclic and time-dependent damage accumulation is included in the model by adding an interaction term to the damage rule;
- the model has been implemented in a multiscale constitutive framework for Ni-base superalloys, which offers the possibility to calculate the damage accumulation specifically in the phase of the material where damage actually develops (i.e. the matrix phase).

Simulations are performed for a wide range of loading conditions by varying the applied strain range, stress ratio, temperature, strain rate and hold time. An adequate agreement between simulations and experiments has been obtained.

Chapter 5

Microstructure degradation⁴

Abstract – During high temperature loading, the regular microstructure of nickel-base superalloys consisting of a γ -matrix (Ni) containing a large volume fraction of γ' -particles (Ni_3Al) degrades. The cubic precipitates coarsen and elongate in a direction normal to the applied stress in a process called rafting. In this paper a phenomenological relation is proposed to describe the kinetics of this degradation process. Also, a relation is presented for the isotropic coarsening process that acts simultaneously and becomes dominant when the rafting is complete. The degradation affects the mechanical response of the material. The relevant mechanisms are discussed and formulations are developed to incorporate the degradation effects in an existing multiscale constitutive framework and in a recently postulated damage evolution equation. The capability of the model to simulate the behaviour of the degraded material is demonstrated by comparing the computational results to experimental observations.

5.1 Introduction

Single crystal nickel-base superalloys are widely used as gas turbine blade materials because of their high resistance against high thermo-mechanical loads. The superior high temperature behaviour is attributed to the two-phase composite microstructure consisting of a γ -matrix (Ni) containing a large volume fraction of γ' -particles (Ni_3Al). The strengthening effect of the γ' -precipitates depends largely on their size and morphology.

During high temperature service, the microstructure gradually degrades by a coarsening process. In the presence of stress, e.g. caused by the centrifugal load in a gas turbine blade, a severe directional coarsening, so-called rafting, of the initially cuboidal γ' -particles into a plate-like structure occurs, see Figure 5-1.

The gradual adaptation of the microstructure results in a deterioration of the mechanical properties. Therefore, to perform a reliable life assessment on gas turbine

⁴ This chapter is based on: Tinga, T., Brekelmans, W. A. M. and Geers, M. G. D.; *Directional coarsening in nickel-base superalloys and its effect on mechanical properties*; Materials Science and Engineering A, submitted (2009), 1-12.

blades, it is highly desirable to include this effect in the constitutive models for Ni-base superalloys.

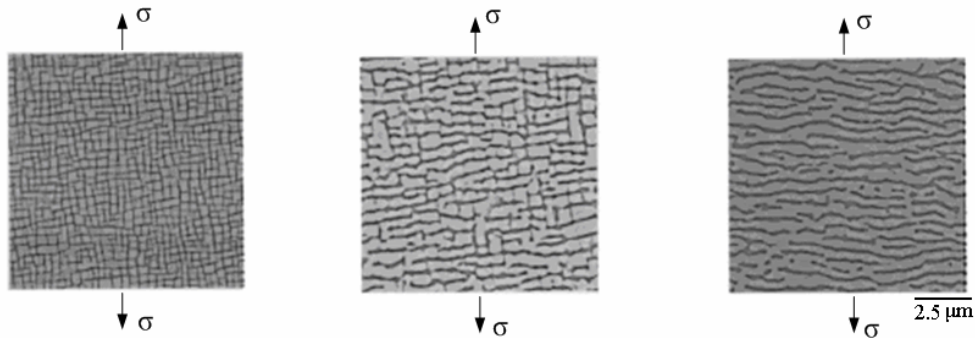


Figure 5-1 Micrographs showing different stages of the microstructure degradation during service. From the left to the right: initial state, intermediate state and fully rafted state.

In the last decades, a lot of experimental research has been done on the microstructure evolution of Ni-base superalloys. This research focused, on the one hand, on the kinetics of the degradation process and on the other hand on the effect of the microstructural changes on the mechanical response of the material.

5.1.1 Kinetics of degradation

The role of internal stresses in the degradation kinetics is addressed by several authors, and particularly the role of the misfit stress, resulting from the small difference in lattice parameters between the γ - and γ' -phases, is explored. The observation that the precipitates elongate in a direction normal to the applied stress, see Figure 5-1, is attributed to the misfit stress.

Throughout the literature, rafting is commonly examined in uniaxially loaded specimens. This is not only a relatively simple and convenient load condition, but also a condition that is representative for many locations in a turbine blade subjected to a radially directed centrifugal force. Further, the external load is commonly defined in the vertical direction, resulting in an elongation of the precipitates in the horizontal direction, see Figure 5-2. This geometrical convention is also used in the present paper, since this is the dominant loading mode to which most discussions refer. Nevertheless, this paper also deviates from this common convention in the part where the extension of the model to the multiaxial case is concerned.

Kamaraj [112] states that the driving force for rafting is the combination of the external and misfit stress into a hydrostatic stress, that affects the chemical potential of

the atoms resulting in diffusion. Further, plastic deformation causes a loss of coherency and reduction of the misfit, which enables rafting. This is confirmed by Matan et al. [113] and Véron et al. [114] who state that the reduction of misfit by creep strain creates the path for rafting in the commercial alloy CMSX-4 at 950 °C. Also, Socrate and Parks [115] conclude, from their simulation work, that during primary creep dislocation networks are formed, that reduce the misfit and enable the rafting process. Keller et al. [116] report that the dislocation networks relax the misfit specifically in the horizontal channels, but increase the misfit in the vertical channels. Finally, Sugui et al. [117] report that rafting is caused by directional diffusion of specific alloying elements. The γ' -phase forming alloying elements Al and Ta diffuse to the vertical channels, where they increase the precipitate size, whereas the γ -phase forming elements Cr and Mo diffuse towards the horizontal channels, where they widen these channels.

From these experimental observations it can be concluded that the onset of degradation is a sequential process: (i) plastic deformation of the matrix material occurs; (ii) this causes a loss of coherency at the γ/γ' -interfaces and a subsequent reduction of the misfit stress; (iii) precipitates start to raft. This hypothesis is supported by experimental results [113,118,119] demonstrating that rafting only occurs after a certain amount of (macroscopic) creep strain. Matan et al. [113] reported a threshold of 0.1% for CMSX-4 at 950 °C, while Henderson et al. [119] found 0.35% at 1000 °C.

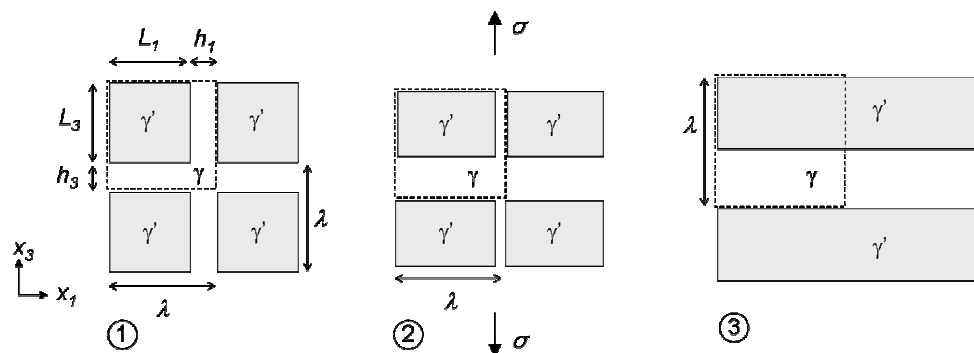


Figure 5-2 Schematic representation of the changes in microstructural dimensions at three different stages of the degradation process: 1) initial state; 2) microstructure in a rafted state, but not coarsened yet (unit cell size has not changed); 3) fully rafted microstructure after a certain amount of coarsening. The unit cell size has increased. The definition of the microstructure dimensions (L , h), periodicity (λ) and orientation of the applied stress (σ) are also shown.

Whereas a certain amount of plastic deformation is a requirement for the onset of rafting, the presence of an external stress surprisingly appears not to be a requirement to sustain the rafting process. Spontaneous rafting is observed experimentally

[113,119,120] at high temperatures and is attributed to internal stresses (e.g. misfit stress, dislocation induced back stress or dendritic stress) that act as a driving force for rafting.

The precipitate volume fraction remains more or less constant during rafting at temperatures below 980 °C, as was shown by Serin et al. [104]. Only beyond this temperature, the γ' -volume fraction decreases significantly with increasing temperature. Note that this decrease can occur without violating the conservation of mass, since γ and γ' are two phases within the same alloy. The position of the alloying elements (mainly Al) in the crystal lattice determines whether a certain region is denoted as matrix phase (Al in solid solution in Ni) or precipitate phase (ordered Ni₃Al). The actual precipitate volume fraction is therefore governed by thermodynamic equilibrium.

The rather constant precipitate volume fraction implies that elongation of the precipitates in the horizontal direction must be accompanied by a reduction of the precipitate dimension in the vertical direction and thus a widening of the associated horizontal matrix channels (Figure 5-2). That process can proceed until the vertical matrix channel in between two neighbouring precipitates has disappeared completely. From that moment, a coarsening process can further widen the horizontal matrix channels, but at a reduced rate, as shown by Epishin et al. [1]. Note that in the latter case the unit cell (Figure 5-2) increases in size.

In another paper, Epishin et al. [103] showed that in the alloy SRR99 the rafting and coarsening processes continue until a topological inversion has occurred: the γ' -phase surrounds islands of the γ -phase. This is caused by the formation of junctions penetrating the γ -phase and connecting neighbouring γ' -rafts. The junctions are formed by diffusion of γ' -forming atoms towards dislocation concentrations in the γ -phase.

Two approaches can be pursued to derive relations for the description of the degradation process: (i) using experimental results to derive phenomenological relations at a global scale; (ii) exploiting knowledge of the driving force for rafting and coarsening to develop more fundamental methods. Since the precipitate size and matrix channel width are geometrically related through their overall volume invariance, the kinetics of degradation can be described in terms of either channel widening or precipitate growth, as will be discussed next.

The phenomenological approach has been followed by Serin et al. [104] and Kamaraj et al. [121], who present a relation for channel widening. The rate of channel widening is assumed to be governed by the applied stress. They attribute this

dependence to the higher equilibrium γ' volume fraction at higher stress. Kamaraj [112] also presents a relation for the increase of the channel width. The widening rate in the channels perpendicular to the applied stress is said to be positive, which is just opposite to what is expected for an alloy with a negative misfit (in which the precipitate lattice parameter is slightly smaller than the matrix lattice parameter). Epishin et al. [1,122] performed a lot of experimental work on CMSX-4 in the framework of the European COST538 project. They observed that the channel widening process shows two stages. Initially the channels widen relatively fast until the channel width has increased to three times the original width, and then the widening rate reduces considerably, yet again constant in time. They also derived a phenomenological relation for the initial channel widening rate at a range of temperatures and applied stresses, which will be discussed in section 5.2.1. Finally, Matan et al. [113] described the kinetics of rafting by defining dimensional parameters L , T and S that characterize the microstructure, and measuring their values in interrupted creep tests. They found that the rafting parameter R (\sim aspect ratio of the precipitates) evolves in time until a saturation value is reached, which is independent of stress or strain.

Several researchers have studied the driving force for degradation and a number of models have been proposed [114,115,118,123-125]. Most of these approaches are based on energy considerations, where the precipitates evolve towards a morphology with a lower energy. The earlier models only considered the elastic energy (e.g. [124,126]), but later the role of plastic deformation was generally recognized and its effect was included in the models as well [114,115,118]. Véron et al. [114] presented a model for channel widening that is based on the competition between plasticity induced mass transport and diffusional mass transport. Socrate and Parks [115] used an energy perturbation approach to derive an interfacial normal stress τ_n that predicts the direction of movement of the γ/γ' -interface. They performed FE calculations and were able to simulate correctly a number of experimental cases. Svoboda and Lukas [118,127] extended this idea and developed an energy-based model for the growth of precipitates, which is similar to the model by Véron et al. [114]. The increase in precipitate size is related to the balance between total energy (consisting of elastic energy, potential energy of loading and energy of dislocations) and dissipation (diffusion).

Buffiere and Ignat [123] developed a dislocation based criterion to describe the raft formation, where a local diffusion mechanism is suggested as the driving force. Finally, Fedelich [125] recently demonstrated that the reduction of the internal stress, caused by the lattice misfit and the dislocation field, is the driving force for rafting. This is the first approach that correlates the rafting directly to the specific arrangement of

the dislocations. Finally, the models discussed here are mainly used to describe the direction of rafting under different load conditions. Only the models by Svoboda [118] and Fedelich [125] also attempt to capture the kinetics of the rafting process. For the coarsening process, the reduction of interfacial energy appears to be the driving force [125].

This completes the review of the work performed on the kinetics of the degradation process. In the next subsection, the contributions with respect to the effects of degradation on the mechanical performance will be reviewed. To conclude this introduction, section 5.1.3 will discuss the implications for the model development in the present chapter.

5.1.2 Effect of degradation on the mechanical response

The effect of microstructure degradation on the mechanical properties of the material has been investigated by several scientists [1,74,103,128-131]. Most of the published work focused on the effects on the creep behaviour, while the effects on the tensile and low cycle fatigue behaviour remained relatively unexplored.

Reed et al. [74] claim that in CMSX-4, at temperatures higher than 1000 °C, the raft formation and eventual inversion of the microstructure prevents the passing of γ' -particles by glide and climb of matrix dislocations, which reduces the creep rate. Kamaraj [112] states in his review that some authors report enhanced creep properties in rafted material, while others report the opposite. Shui et al. [128,129] studied the effect of P-type rafts (parallel to the load axis) on the creep behaviour. They found different effects at 800 °C and 1000 °C. At 800 °C the creep rate was higher, since the shearing of the incoherent rafts is easier than shearing of the coherent cubes. On the other hand, at 1000 °C, the performance is better, since the driving force for climb is larger on the horizontal γ/γ' -interfaces and thus, in a P-type rafted structure, climb is effectively impeded by the large vertical γ/γ' -interfaces. Finally, topological inversion of the microstructure, as observed by Epishin et al. [103] in SRR99, is accompanied by a drastic increase of the creep rate. The zig-zag shape of the interfaces in this inverted state enhances γ' -shearing, while dislocation climb is also still possible.

Ott and Mughrabi [130] studied the effect of rafting on the low cycle fatigue (LCF) life of CMSX-4 and CMSX-6 at 950 °C. It was observed that cracks propagate in γ or at the γ/γ' -interface. Therefore, parallel rafts in the material reduce the life time, since they enhance crack propagation, while perpendicular rafts increase the life by blocking the cracks. This is contradicted by Zhou et al. [131], who report that rafts

perpendicular to the loading axis increase the LCF life, since they hinder the dislocation movement.

In the context of the recent European collaborative project COST538, several groups performed tensile and low cycle fatigue tests on degraded CMSX-4 specimens. It was observed that the degraded specimens show a significantly weaker tensile response than virgin specimens and that the fatigue life for the degraded specimens is lower than that of the virgin specimens [1].

5.1.3 Implications for modelling

It can be concluded that the kinetics of degradation has been studied extensively and that the mechanisms are now at least partially understood. A number of authors proposed models to describe the kinetics of rafting, but these models are almost exclusively limited to the uniaxial load case. The amount of published experimental data on the mechanical properties of degraded microstructures is rather limited. Moreover, the mechanisms that are responsible for the observed effects are not fully clear yet. Numerical models that are capable of simulating the effects of microstructure degradation are not readily available.

In this chapter, formulations will be proposed to incorporate the kinetics of the degradation process in the constitutive framework for nickel-base superalloys presented in [62,132] (see chapters 2 and 3). The unit cell adopted there represents the Ni-base superalloy microstructure on the material point level. It contains 16 regions (see Figure 5-3): 1 γ' -precipitate region, 3 γ -matrix channel regions ($\gamma_1, \gamma_2, \gamma_3$) with different orientations and 12 interface regions (I_k^m and $I_k^p, k = 1 \dots 6$) either associated with the matrix partition or with the precipitate side. A matrix and a precipitate interface region together form a bi-crystal, which is located on each face of the γ' -precipitate, taking into account the processes that take place at the γ/γ' -interfaces.

Incorporation of the kinetics of the degradation process in the constitutive framework requires the development of a 3D kinetics description. Moreover, model equations will have to be developed that enable the simulation of the effects of microstructure degradation on the mechanical response and damage evolution. In summary, the present chapter forwards the following original aspects:

- a new phenomenological formulation to describe the kinetics of rafting for a general load condition (not limited to the commonly treated uniaxial stress state);
- a formulation for the coarsening process, acting simultaneously with the rafting process and incorporated in the kinetics description;

- incorporation of the effect of the microstructure degradation in a recently proposed constitutive framework [62,132];
- incorporation of the effect of the degradation on the damage accumulation during cyclic deformation in a recently proposed damage model for Ni-base superalloys [77].

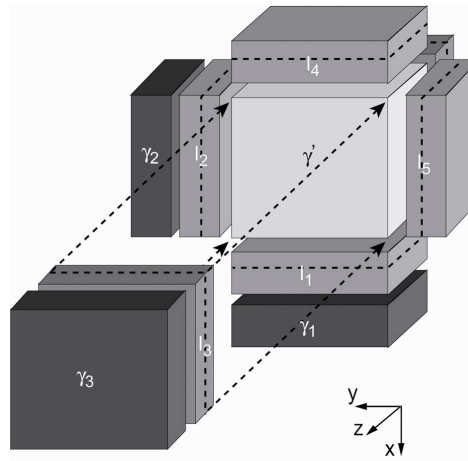


Figure 5-3 Schematic overview of the unit cell adopted in the constitutive framework in [62, 132].

In the next section a model is established to describe the kinetics of rafting for a general multiaxial load condition. In section 5.3, the effect of microstructure degradation on the mechanical response of the material is analyzed and a method to implement this in the constitutive framework is proposed. In section 5.4, the effect of microstructure degradation on the damage evolution is discussed and modelled. Finally, in section 5.5 the integral model is applied to demonstrate its predictive capabilities in reproducing experimental results.

5.2 Kinetics of microstructure degradation

In this section, the kinetics of both the rafting and coarsening process will be discussed and formulations to describe these processes are proposed.

5.2.1 Rafting

As was discussed in the introduction, the kinetics of the rafting and coarsening processes has been studied extensively. In the present work, the phenomenological

relation for the horizontal channel widening rate \dot{h} during vertical tensile loading as derived by Epishin et al. [1] is taken as the point of departure. This relation has been postulated for rafting in CMSX-4 at temperatures ranging from 850 °C to 1050 °C and stress levels from 50 to 350 MPa:

$$\dot{h}(T, \sigma) = A \exp \left[-\frac{Q - \sigma U(T)}{RT} \right] \quad (5.1)$$

where σ is the (uniaxial) stress and T the absolute temperature. The pre-exponential factor A and activation energy Q are material constants and R is the universal gas constant. The temperature dependent parameter $U(T)$ is defined as

$$U(T) = U_T (T - T_0)^n \quad (5.2)$$

for $T > T_0$. The exponent n , the reference temperature T_0 and the prefactor U_T are model parameters. For temperatures below T_0 no rafting is observed in experiments.

As was concluded in the introduction, the degradation process consists of two stages: rafting and coarsening. The relations proposed by Epishin et al. [1] describe the evolution of the width of the matrix channels normal to the applied load (horizontal channels) in a uniaxially loaded specimen during the rafting stage. In the remainder of this subsection, relations are derived to additionally calculate the evolution of the channel widths in the matrix channels parallel to the applied load (vertical channels) and of the precipitate dimensions. Further, the relations will be extended to make them applicable to a general multiaxial stress state. Then, in subsection 5.2.3, the kinetics of the coarsening process is incorporated in the formulation. Since experimental work has not clearly demonstrated whether rafting and coarsening are simultaneous or sequential processes, this question will be addressed in 5.2.4.

During the rafting process, the precipitate volume fraction remains theoretically constant [1]. This implies that the increase of the precipitate size in the directions perpendicular to the load must be compensated by a decrease of the size in the direction of the load. Further, the microstructure periodicity λ , defined as the sum of the precipitate size (L) and the matrix channel width (h), see Figure 5-2, is observed to remain more or less constant in all three directions.

These experimental observations allow the following relations between L_i and h_i :

$$L_i + h_i = \lambda \quad (i = 1, 2, 3) \quad (5.3)$$

$$L_1 L_2 L_3 = C_1 \quad (5.4)$$

The value of the precipitate volume C_i and the value of λ can be obtained from the dimensions of the virgin microstructure. For a material that is loaded uniaxially in the x_3 -direction, the channel width h_3 will increase, consistent with equation (5.1) and, according to relation (5.3), the precipitate size L_3 will decrease. Due to symmetry considerations, L_1 and L_2 will increase equally, and their values follow from relation (5.4).

For the more general case of a multiaxial load condition the precipitate size in the considered three orthogonal directions ($i = 1, 2, 3$) is proposed to satisfy:

$$\dot{L}_i(T, \sigma) = -\frac{3}{2} L_i \left[\frac{\sigma_{ii}^d}{\sigma_{VM} + \varepsilon} \right] \frac{A}{L} \exp \left[-\frac{Q - \sigma_{VM} U(T)}{RT} \right] \quad (5.5)$$

where $U(T)$ is given by (5.2), σ_{ii}^d are the diagonal components of the deviatoric stress tensor, L is the virgin precipitate size and A and ε are constants. The uniaxial stress σ in (5.1) has been replaced by the Von Mises equivalent stress (σ_{VM}) to quantify the rate of change of the precipitate dimensions. Experimental work [133] has demonstrated a strong correlation between the equivalent stress and the degree of rafting. Additionally, the deviatoric stress components (normalized by the Von Mises stress) are used to define the relative growth in the three directions. By adding the ratio of the actual value of L_i and the virgin precipitate size L to the equations, condition (5.4) is automatically satisfied. For a purely hydrostatic stress state ($\sigma_{11} = \sigma_{22} = \sigma_{33}$) it is expected that no rafting will take place at all. This is correctly captured in (5.5). Moreover, adding a small positive constant ε to the denominator of the first factor ensures that the limit of this factor behaves properly and tends to zero when σ_{VM} approaches zero. For a purely uniaxial case, the equations reduce to equation (5.1). When all three precipitate dimensions are known, equation (5.3) can be used to determine the associated matrix channel widths (h_i).

The rafting process only allows a limited increase of the channel widths, since it is associated with a simultaneous decrease of the precipitate size, as dictated by equation (5.3). Further, the decrease of the precipitate size in one direction requires an increase of its size in the transverse directions. The increase of the latter dimension is restricted by the value of λ (corresponding to the case where the vertical matrix channels have virtually disappeared). This coupling of dimensional changes in different directions only allows an increase of the matrix channel width in CMSX-4 from 60 to 161 nm. However, after completion of the rafting process, the channel width can further increase through coarsening, as will be discussed in section 5.2.3. If coarsening

occurs simultaneously with rafting, the maximum matrix channel width during rafting is larger (~ 182 nm, depending on coarsening rate), as will be shown in 5.2.4.

In the numerical implementation, the dimensions of the microstructure are modified each time increment according to equation (5.5). Several internal variables in the constitutive model [62] are dependent on these dimensions. In particular, the densities of the statistically stored dislocations (SSDs) and geometrically necessary dislocations (GNDs), that are used in [62] to model the plastic slip behaviour, might be affected by the geometrical changes. As a consequence, it is necessary to verify whether these quantities remain physically acceptable. Firstly, the SSD densities depend on the total dislocation line length that is present in the volume of the considered region. Rafting is a diffusion based process, which might reduce the number of SSDs. However, when the SSD density is close to saturation (creation and annihilation are in balance) and the external load is sustained, both diffusion and volume changes will not affect the SSD density significantly. A deviation from the saturation value will quickly be restored through the creation of additional SSDs. Since the SSD density is already saturated after a small amount of plastic deformation, the SSD densities do not need to be corrected.

The GNDs are intrinsic characteristics of the geometry of the crystal structure, since they maintain the compatibility of the deformed lattice, and their amount cannot be reduced by diffusion. Only a recrystallization of the material would reduce the number of GNDs. Moreover, the GND densities are governed by the strain gradients in the interface regions between the matrix and the precipitate phase [62] (see chapter 2 and Figure 5-3) and therefore depend on the width of the interface they reside in. Thus, the GND densities should only be corrected for the change of the interface width (w) in the actual time increment according to:

$$\rho_{GND}^{j+1} = \rho_{GND}^j \left(\frac{w^j}{w^{j+1}} \right) \quad (5.6)$$

where the superscripts j and $j+1$ refer to the previous and actual time increment, respectively. The parameter w represents the width of the interface region (either matrix side or precipitate side, see Figure 5-3). The value of w depends on the values of the channel width ($0.30 h_i$) or precipitate dimension ($0.05 L_i$) for the matrix and precipitate sides, respectively. An increase of the channel width thus yields an increased width of the corresponding matrix interface region.

5.2.2 Driving force for rafting

In the present model, rafting is described in a phenomenological way by equation (5.5). The degradation rate is a function of the temperature and the applied stress as obtained from numerous experiments [1]. However, the real driving force for rafting is a reduction of the total amount of recoverable energy in the material, as discussed in the introduction of this chapter. Therefore, to check the energetic consistency of the present formulation, the stored elastic energy in the unit cell will be determined. This is accomplished by considering the strain energy density Ψ^i in unit cell region i through its common expression:

$$\Psi^i = \frac{1}{2} \boldsymbol{\sigma}_{eff}^i : \boldsymbol{\epsilon}_{el}^i \quad (5.7)$$

where the effective stress is the sum of the externally applied stress, the misfit stress and the dislocation induced back stress. The elastic strain is related to the effective stress through the compliance tensor ${}^4\mathbf{S}$:

$$\boldsymbol{\epsilon}_{el}^i = {}^4\mathbf{S} : \boldsymbol{\sigma}_{eff}^i \quad (5.8)$$

Finally, the total strain energy density of the complete unit cell is obtained by summation over all regions

$$\Psi = \sum_{i=1}^{10} f^i \Psi^i \quad (5.9)$$

where f^i is the volume fraction of the i -th region.

Figure 5-4 shows the differences in the evolution of the strain energy density during a simulated creep test at 950 °C and 110 MPa with and without rafting. If no degradation is included, the strain energy density decreases slowly as creep proceeds, due to the plastic deformation in the material. When degradation is included in the model, the strain energy density decreases considerably faster during the rafting process. This reduction of the internal energy is generally considered as the driving force for the rafting process.

These results illustrate that it is energetically favourable for the material to raft. Further, it demonstrates that, although the degradation process is modelled here in a phenomenological way, the formulation consistently predicts a reduction of the internal energy as a result of microstructure degradation. As mentioned before, the main driving force for coarsening is the reduction of the interfacial energy. Therefore, the coarsening process is here not related to the changes in strain energy.

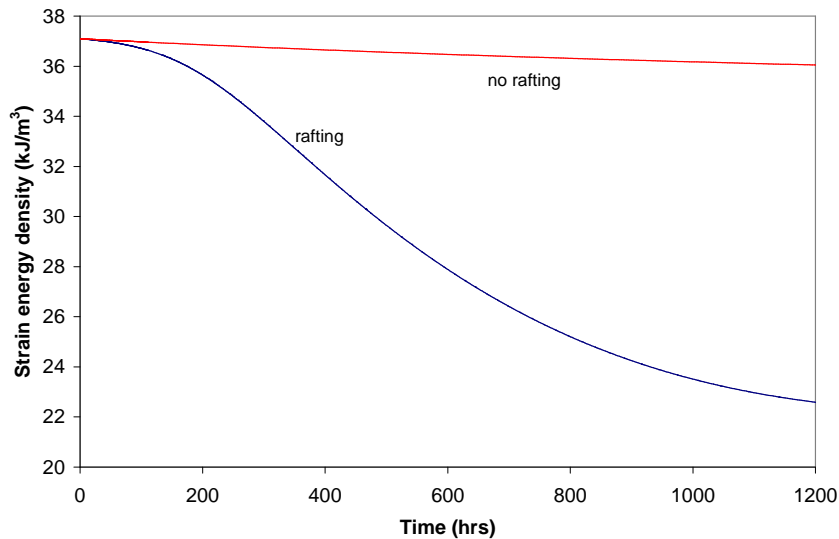


Figure 5-4 Calculated reduction of the strain energy density during a simulated creep test at 950 °C and 110 MPa. Simulations with and without rafting are compared.

Note that the present model is able to predict the direction of rafting in alloys with a negative misfit, in which the precipitate lattice parameter is slightly smaller than the lattice parameter of the matrix phase. As discussed before, experiments have shown that rafts develop normal to the applied load in these alloys. However, in alloys with a positive misfit, the rafts are shown to develop parallel to the applied load. This difference is attributed to the role of the misfit stresses in the activation of rafting. In a negative misfit alloy, plastic slip starts in the horizontal matrix channels, where it causes a loss of coherency at the γ/γ' -interface. As discussed in section 5.1.1, this loss of coherency initiates the formation of horizontal rafts. In positive misfit alloys, the misfit stresses trigger the vertical matrix channels to deform plastically, which consequently leads to the formation of vertical rafts. Since in the present model the internal stresses are not included in the evolution equation (5.5), this effect can not be simulated and the direction of raft formation is explicitly defined by the sense of the deviatoric stress components σ_{ii}^d in these equations. For the same reason, also the phenomenon of spontaneous rafting, where the microstructure degradation driven by internal stresses proceeds when the remote load is removed, is not covered by the present model.

5.2.3 Coarsening

The second degradation process that takes place in Ni-base superalloys is microstructural coarsening. Due to this process, the microstructure periodicity increases, indicating that the γ/γ' -microstructure coarsens on a more global scale: the larger precipitates and rafts increase in size to the expense of the smaller particles, which disappear. This process, and the associated topological inversion of the microstructure (γ' -phase surrounds islands of the γ -phase) is described in detail in [103].

As discussed before, the rafting process only allows a limited increase of the channel width. After completion of the rafting process, the channel width can further increase by the coarsening process, yet, with a reduction of the total number of channels. Experimental results published by Epishin et al. [1] showed a clear change of widening rate when the channel width reached the 160 – 180 nm range, indicating that the widening rate during the coarsening process is considerably smaller than during rafting.

In [1] it is suggested that rafting and coarsening are more or less sequential processes. However, these processes might also act simultaneously. Epishin et al. [1] claim that the coarsening process is controlled by the migration of γ' -terminations, which widens the remaining matrix channels, and the nucleation of γ -terminations, which results in a topological inversion. These mechanisms can only manifest themselves after the formation of rafts. However, another contribution to the coarsening is the diffusion-based process of ripening, which means that the larger precipitates increase their size to the expense of the smaller particles, which disappear. The latter mechanism is not dependent on raft formation and can therefore be active simultaneously with the rafting process. Experiments [1] have shown that the microstructure periodicity increases up to 20% during rafting, which supports the hypothesis of simultaneous coarsening.

Epishin et al. [1] determined the parameters for equations (5.1) and (5.2) from experiments at a wide range of test conditions, but did not quantify the channel widening rate during coarsening for the complete range of conditions. The only indication is the widening curve at one specific condition (950 °C, 110 MPa), for which the widening rate during coarsening was only 20% of the widening rate during rafting. In the present model, the coarsening process is implemented by increasing the unit cell size. This is realized by an increase of the periodicity parameter λ in equation (5.3) using the stress and temperature dependence of the channel widening from [1]:

$$\dot{\lambda} = f_c A \exp \left[-\frac{Q - \sigma_{VM} U(T)}{RT} \right] \quad (5.10)$$

where the uniaxial stress σ has been replaced by the Von Mises equivalent stress σ_{VM} . The constant f_c represents the fraction of the channel width evolution rate in (5.1) characterizing the evolution rate of the microstructure periodicity.

During the coarsening that occurs after the rafting has completed, the channel width and precipitate size increase proportionally from their values at the end of the rafting process (h_r , L_r and corresponding λ_r), which means that

$$\frac{\dot{h}_{coars}}{\dot{\lambda}_{coars}} = \frac{h_r}{\lambda_r} \quad (5.11)$$

Based on the experimental observation at 950 °C and 110 MPa, it can be readily assumed that the channel widening rate during coarsening equals 20% of the rate during rafting:

$$\dot{h}_{coars} = 0.20 \dot{h}_{raft} \quad (5.12)$$

As a result, the microstructure periodicity λ increases with a rate proportional to

$$\dot{\lambda}_{coars} = 0.20 \dot{h}_{raft} \left(\frac{\lambda_r}{h_r} \right) \approx 0.70 \dot{h}_{raft} \quad (5.13)$$

which means that the fraction f_c in equation (5.10) is to be taken equal to 0.70. Moreover, it is assumed that the microstructure periodicity increases equally in all directions (i.e. the unit cell remains cubic). Note that for a fully rafted microstructure (lamellar structure), only the periodicity in the direction normal to the rafts is a relevant quantity. In the plane of the rafts the periodicity is not well defined anymore, see Figure 5-2. The dimensions of the unit cell in those directions can therefore be taken arbitrarily and the assumed cubic unit cell remains a valid assumption.

5.2.4 Combined rafting and coarsening

Finally, the question whether coarsening starts after the completion of rafting or occurs simultaneously with rafting is addressed. The formulations for rafting and coarsening presented in the previous sections are based on the assumption that the two processes are sequential. To simulate the degradation with simultaneous rafting and coarsening, the following two-step procedure is used in each time increment. Firstly, the increase of the microstructure periodicity λ due to coarsening is calculated from (5.13) and the values for h_i and L_i are updated proportional to the increase of λ . Secondly, the evolution of the precipitate dimensions (L_i) due to rafting is calculated according to

(5.5), which also provides the values of h_i . The increase of λ in the first step implicitly means that the constant C_i in (5.4) increases. However, C_i remains constant during the second step (rafting), which means that (5.5) is still valid. Moreover, $f_c = 0.70$ is used for the simultaneous simulation, although strictly speaking the momentary ratio of λ and h should be used in (5.11) to relate the periodicity increase to the channel widening rate.

The experimentally determined evolution of the microstructure at 950 °C and a uniaxial load of 110 MPa [1] is shown in Figure 5-5, together with the results of the present model. If rafting and coarsening are treated as sequential processes, the rafting is completed at a horizontal channel width of 161 nm. In that condition, the two vertical channel widths are effectively zero. In [1], an approximate criterion of $h_3 = 3h_0$ is used to define the completion of rafting, which results in a final channel width equal to 180 nm. The latter value corresponds reasonably well to the experimentally observed channel width. However, this value is geometrically impossible to reach without coarsening. The approximation made in [1] did not involve any geometrical considerations in the model used.

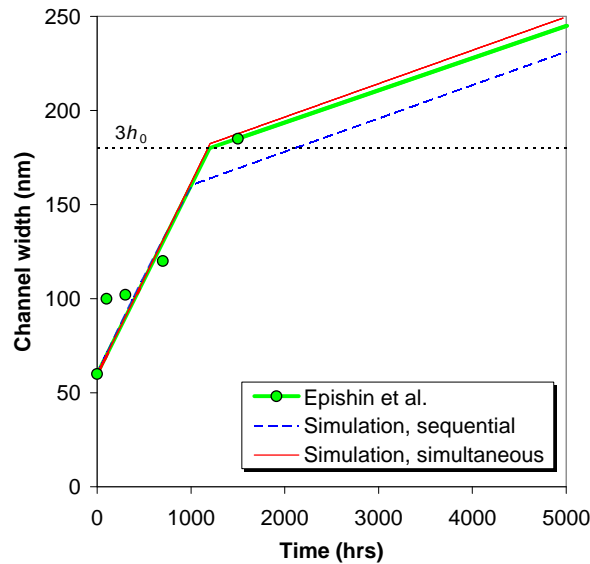


Figure 5-5 Evolution of the channel width during a creep test at 950 °C and 110 MPa. Results from [1] are compared to simulations with the present model, where rafting and coarsening are treated as sequential and simultaneous processes respectively.

If, on the other hand, the coarsening process is active simultaneously with rafting, the present model predicts a channel width at the completion of rafting of 182 nm, as can

be seen in Figure 5-5. This value is remarkably close to the experimental value, which strongly supports the hypothesis that coarsening and rafting are simultaneous processes.

Relation (5.1) from [1] describes the experimentally observed channel widening rate, stating that no coarsening occurs during rafting. In the present work, coarsening and rafting are simulated as simultaneous processes, which means that the simulation will overestimate the experimental results. On the other hand, addition of the ratio L_i/L to the evolution equation (5.5) reduces the average channel widening rate. Since these two effects have similar magnitudes, using the original value of the constant A [1] still yields results that match the experiments.

5.3 Effect on the deformation

Experiments have shown that the mechanical response of degraded material is different from the response of virgin material. In this section the relevant mechanisms are discussed and implemented in the constitutive framework presented in [62,132] (chapters 2 and 3).

5.3.1 Mechanisms

The changes in matrix channel widths and precipitate dimensions have several effects on the mechanical response:

- the Orowan threshold τ^{or} is inversely proportional to the channel width and therefore decreases in the horizontal channels and increases in the vertical channels during rafting (for a vertical uniaxial load). A decrease in Orowan stress will lead to an increased matrix slip rate [125].
- the shearing process becomes easier, since the coherency between the matrix and precipitate phases reduces during rafting. Misfit dislocations are formed at the γ/γ' -interfaces, which enhances the shearing of the precipitates by matrix dislocations [128]. Moreover, the misfit stresses are lowered through the coherency loss, which also affects the mechanical response of the material. Further, topological inversion (γ' becomes the matrix with a distribution of isolated γ -regions) results in a zig-zag shape of the rafts. This provides a number of $\{111\}$ oriented interfaces, which also enhance precipitate shearing [103].
- the recovery climb mechanism will experience more resistance, since the climbing distance increases when the precipitates become elongated. From the moment that the microstructure is completely rafted (large numbers of precipitates connected), the climbing distance is increased significantly [134,74].

The first two mechanisms yield an increased slip rate in rafted material at conditions where matrix slip and/or precipitate shearing govern the deformation rate (tensile tests, creep tests at high stress levels). On the other hand, at creep conditions where the climb mechanism dominates the deformation rate (low stresses – no shearing), the rafting process increases the load bearing capacity of the material (reduces the slip rate).

5.3.2 Incorporation in the crystal plasticity framework

In this section, the experimentally observed mechanisms as described in the previous section are incorporated in the model presented in [62,132] (chapters 2 and 3). This will enable the simulation of the effects of degradation on the mechanical response of the material.

In the matrix phase slip law, the change of the Orowan stress (τ^{or}) is automatically incorporated, since this threshold is present in the adopted formulation [62] for the slip rate $\dot{\gamma}^\alpha$ on a slip system α :

$$\dot{\gamma}^\alpha = \dot{\gamma}_0 \left\{ \frac{|\tau_{eff}^\alpha|}{s^\alpha} \right\}^m \left\{ 1 - \exp\left(-\frac{|\tau_{eff}^\alpha|}{\tau^{or}}\right) \right\}^n \text{sign}(\tau_{eff}^\alpha) \quad (5.14)$$

In this relation, τ_{eff}^α is the effective resolved shear stress, s^α represents the slip resistance and $\dot{\gamma}_0$, m and n are material constants.

Due to the formation of misfit dislocations at the interface, causing a loss of coherency, the misfit stresses are reduced. However, this also happens through plastic deformation only, i.e. without rafting. The reduction of the misfit stress as a function of the plastic deformation is already incorporated in the model [62] (see chapter 2). If the evolution of the microstructure (and associated plastic deformation) is simulated, the reduction of the misfit stresses is automatically effectuated.

The GND densities and associated back stresses are only affected indirectly, since they are based on the plastic strain gradients at the interfaces. As was discussed in 5.2.1, this effect is incorporated through equation (5.6). The remaining quantities in the slip law are not affected by the rafting.

In the precipitate phase, the slip rate contains contributions from the two precipitate phase deformation mechanisms, precipitate shearing and recovery climb, and is again a function of the effective resolved shear stress, as given by [132]

$$\dot{\gamma}^\alpha = \frac{SbS_{int}}{V} \tilde{\rho}_{GND}^\alpha \left[f_{diss} \left\{ 1 - \exp\left(-\frac{|\tau_{eff}^\alpha|}{s_0^\alpha}\right) \right\}^p + \frac{4v_{climb}^\alpha}{H_{\gamma'}} \right] \text{sign}(\tau_{eff}^\alpha) \quad (5.15)$$

where b is the Burgers vector and $\tilde{\rho}_{GND}^\alpha$ represents the number of dislocations that is available for precipitate shearing or climb. The exponent p is a material constant. The parameters for precipitate shearing are given by

$$f_{diss} = f_0 \exp\left(-\frac{\Delta E}{kT}\right) \quad (5.16)$$

$$\Delta E = \beta \frac{\mu^{3/2} b_{sisf}^3}{\sqrt{|\tau_{eff}^\alpha| - \tau_c^\alpha(T)}} \quad (5.17)$$

In these relations, T is the absolute temperature, k is the Boltzmann constant, μ is the precipitate phase shear modulus, and b_{sisf} is the Burgers vector of a partial dislocation in the precipitate. The frequency f_0 , the critical stress τ_c and the parameter β are material constants. The climb velocity is defined as

$$v_{climb}^\alpha = C |\tau_{eff}^\alpha| \exp\left(-\frac{Q^c}{RT}\right) \text{sign}(\tau_{eff}^\alpha) \quad (5.18)$$

where Q^c is an activation energy, C a material constant and R the universal gas constant. The changes in microstructural dimensions affect the geometric parameters S , S_{int} , V and H_γ . During rafting, the precipitate volume V remains constant, whereas it increases during coarsening. The climbing distance H_γ will increase, thus decreasing the climb velocity. The change of the interfacial area S_{int} depends on whether a horizontal or vertical interface is considered. The former will increase, while the latter decreases. Finally, the area (S) swept by the dislocation on shearing the particle increases during rafting. In addition to these purely geometric effects, which are naturally incorporated in the framework, a few additional mechanisms have to be included.

The significant increase of the climbing distance from the moment that the rafting is complete must be added, since this effect contributes to the mesoscopic level, which is on a length scale larger than that of the unit cell. Therefore, as long as the precipitates are not connected (incomplete rafting), the climb distance is defined as

$$H_{\gamma'} = \max(L_1, L_2, L_3) \sqrt{3} \quad (5.19)$$

but as soon as the rafting process is complete, the climb distance is increased by a factor C_{raft} through

$$H_{\gamma'} = C_{raft} \max(L_1, L_2, L_3) \sqrt{3} \quad (5.20)$$

The value of C_{raft} depends on the regularity of the microstructure. For a perfectly regular composition all vertical matrix channels will disappear exactly at the same

moment, which means that C_{raft} equals infinity. For a very irregular microstructure, only a small number of precipitates connect, represented by a value of C_{raft} in the order $2 - 10$. The moment that two neighbouring precipitates tend to touch is detected by checking whether the width of the vertical matrix channel is below a critical value.

The loss of coherency of the γ/γ' -interfaces enhances the shearing of the precipitates by matrix dislocations. This mechanism can be incorporated in the model by modifying either the values of τ_c^α , f_o or β , see (5.16) and (5.17), which are the parameters that govern the dissociation into partial dislocations required for precipitate shearing. Modification of the parameter β is selected here to reflect the effect of coherency loss on precipitate shearing. The loss of coherency proceeds gradually during the rafting process, and is already completed before the microstructure has fully rafted. After the completion of rafting, the coarsening process proceeds and a topological inversion occurs [103]. However, the resistance against precipitate shearing does not change significantly during this final stage of the degradation process.

To incorporate this effect, the parameter β in (5.17) is replaced by the parameter β^* , with an initial value (for a virgin microstructure) equal to the original value of β . For an increasing channel width h , the value of β^* decreases linearly, proportional to the increase of h from its initial value h_o to a final value h_f , according to

$$\beta^* = \beta \left[1 - C_\beta \frac{h - h_o}{h_f - h_o} \right] \quad (5.21)$$

The value of h_f , i.e. the channel width associated to a complete coherency loss, and C_β are determined from experimental results.

5.4 Effect on the damage accumulation

In addition to the effects of degradation on the material mechanical response, the damage accumulation is also affected. This section discusses the responsible mechanisms and forwards a formulation to incorporate these effects in the damage model, for which the basis is presented in [77] (chapter 4).

5.4.1 Mechanisms

The degradation of the microstructure contributes to the damage accumulation both directly and indirectly. Directly, the previously addressed changes in the mechanical response naturally affect the damage evolution. Indirectly, fatigue crack propagation is much easier in the rafted structure than in the virgin microstructure [1]. Experimental studies [135,130] have shown that the crack growth rate increases considerably when the

material has rafted. Moreover, metallographic investigation has confirmed that crack growth occurs preferably along the extended γ/γ' -interfaces [130]. The lamellar morphology of the rafts therefore reduces the life time and enhances the damage evolution.

5.4.2 Incorporation in the damage model

The mechanism described above is incorporated in the damage model [77] (chapter 4) by extending the parameters that govern the cyclic damage evolution:

$$\Delta D_i^{fat} = \sum_{\alpha=1}^{12} \Delta^\alpha D_i^{fat} = \sum_{\alpha=1}^{12} \left(\frac{|\tau_{max}^\alpha|}{\tau_{ref}} \right)^{m_{fat}} \left(\frac{|\dot{\gamma}_{max}^\alpha|}{\dot{\gamma}_{0,fat}} \right)^{n_{fat}} \exp\left(\frac{-Q^c}{RT}\right) \quad (5.22)$$

where ΔD_i^{fat} is the cyclic damage increment in unit cell region i for the present cycle, which contains contributions from all 12 slip systems. This damage increment depends on the maximum resolved shear stress (τ_{max}^α) and slip rate ($\dot{\gamma}_{max}^\alpha$) during the cycle. The parameters m_{fat} , n_{fat} , τ_{ref} , $\dot{\gamma}_{0,fat}$ and Q^c are material constants and R is the universal gas constant.

The stress and slip rate sensitivities (m_{fat} , n_{fat}) are not expected to change due to degradation of the microstructure. The observed reduction in the number of cycles to failure is incorporated in the model by decreasing the value of the scaling factor $\dot{\gamma}_{0,fat}$ to $\dot{\gamma}_{0,fat}^*$. As the amount of available experimental data is limited, it is hardly possible to determine the gradual change of the damage accumulation process during rafting. Therefore, the value of $\dot{\gamma}_{0,fat}$ is modified in a stepwise manner: for the virgin microstructure the initial value ($\dot{\gamma}_{0,fat}$) is used, and a reduced value ($\dot{\gamma}_{0,fat}^*$) is used from the moment that the material is fully rafted.

5.5 Application

The formulations proposed in the previous section are implemented in the crystal plasticity framework and simulations are performed to determine the values of the complementary model parameters, as summarized in Table 5-1. Further, to validate the proposed formulations, the simulation results are compared to experimental results for tensile and cyclic tests at different load conditions.

Note that Table 5-1 only contains the complementary parameters related to the microstructure degradation and the damage model parameter $\dot{\gamma}_{0,fat}$. The other parameters for the constitutive model are taken from [132] (chapter 3) and the damage model parameters can be obtained from [77] (chapter 4), except for the value of $\dot{\gamma}_{0,fat}$. The latter value is different from [77], since an improved version of the constitutive

model was used here, which required an update of the value for $\dot{\gamma}_{0,fat}$. A complete overview of all parameter values used in the constitutive model and damage rule is provided in Appendix B.

Table 5-1 Model parameter values for CMSX-4.

parameter	value	unit	used in eq.
A	$2.59 \cdot 10^{-5}$	$m s^{-1}$	(5.1), (5.5)
Q	221780	$J mol^{-1}$	(5.1), (5.5)
L	500	nm	(5.5)
U_T	0.19	$J (mol \cdot MPa \cdot K^n)^{-1}$	(5.2)
T_0	1100	K	(5.2)
n	1.294	-	(5.2)
C_1	$1.25 \cdot 10^8$	nm^3	(5.4)
f_c	0.70	-	(5.10)
h_r	161	nm	(5.13)
λ_r	560	nm	(5.13)
C_{raft}	20	-	(5.20)
h_f	107	nm	(5.21)
C_β	0.39	-	(5.21)
$\dot{\gamma}_{0,fat}$	$6.28 \cdot 10^{-3}$	s^{-1}	(5.22)
$\dot{\gamma}_{0,fat}^*$	$2.31 \cdot 10^{-4}$	s^{-1}	(5.22)

5.5.1 Tensile response

To demonstrate the ability of the model to predict the effect of microstructure degradation on the material tensile response, tensile tests will be simulated with both virgin and degraded microstructures. The effect of microstructure degradation can be incorporated in the simulations in two ways: modifying the geometry by changing the values of L and h instantaneously or simulating a complete degradation test prior to the tensile test simulation until the required channel width is reached. In the latter case all internal variables, the plastic strain and the dislocation densities (SSD and GND), evolve during the degradation period. At the start of the tensile test, these internal variables will therefore take different values.

However, typical degradation conditions (e.g. creep for 2500 hrs at 1050 °C and 150 MPa) only yield small plastic strains in the order of 0.1 – 0.5 %. Moreover, the values of the SSD densities do not change significantly and the internal back stresses caused by the GNDs are also relatively small. Therefore, for short degradation periods,

a tensile test simulation on degraded material can be approximated quite well by performing a simulation with incorporation of an updated geometry only. For longer degradation periods, the degradation must be incorporated in a simulation in advance to obtain the proper values of the internal variables at the start of the tensile test. The difference between the two methods is shown in Figure 5-6 for a short degradation period (channel width of 91 nm) and a longer degradation period ($h = 173$ nm), respectively. For $h = 91$ nm there is no significant difference between the curves generated with the two methods, while for a fully rafted microstructure ($h = 173$ nm) simulation of the degradation process yields a tensile curve that is about 5 % lower. The latter effect is mainly due to lower strain gradients in the wide horizontal matrix channels, resulting in lower back stresses in those regions. The higher back stresses in the vertical channels play a marginal role, since the volume fraction of these regions becomes relatively small.

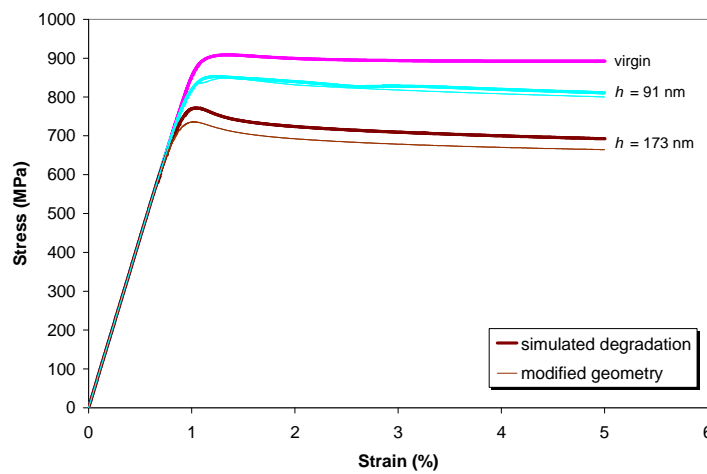


Figure 5-6 Simulated tensile curves at 950 °C and a strain rate of 10^{-3} s^{-1} for different degrees of degradation. Two methods to incorporate the degradation are compared: modification of the geometry only and simulation of the degradation process.

Next, the simulated tensile test results at 950 °C are compared to experimental results [136,137] in Figure 5-7 and Figure 5-8 for different degrees of degradation. These curves demonstrate that the effect of microstructure degradation can be simulated adequately, especially for the rafting part of the degradation (Figure 5-7). For the larger channel widths caused by coarsening (Figure 5-8), the deviation between simulation and experiment is somewhat larger. However, these simulations are performed at a lower strain rate, for which the deviation between simulation and experiment in the virgin

condition is also larger. A better understanding of the deviations requires much more experimental data for degraded material, which is not available yet. However, the overall effect of degradation is predicted reasonably well by the proposed model.

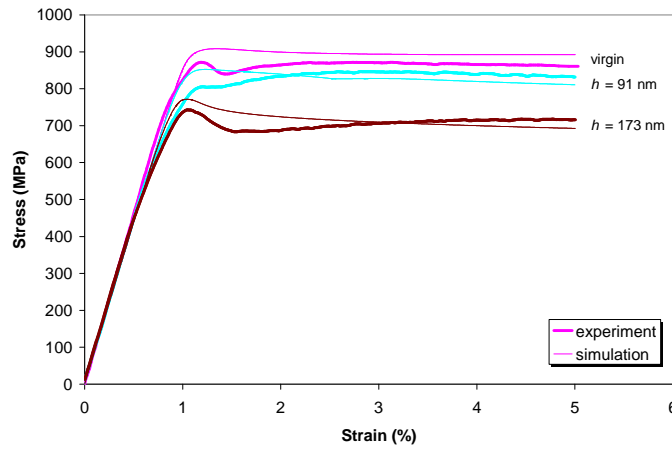


Figure 5-7 Simulated tensile tests at 950 °C and strain rate 10^{-3} s^{-1} compared to experimental results for virgin material and two degrees of degradation.

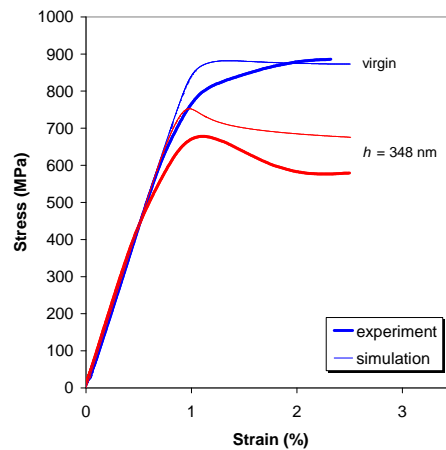


Figure 5-8 Simulated tensile tests at 950 °C and a strain rate of $0.6 \cdot 10^{-3} \text{ s}^{-1}$ compared to experimental results for virgin and degraded material.

5.5.2 Cyclic response

This section aims to demonstrate the capability of the model to simulate the effect of microstructure degradation on the cyclic response of the material. Therefore, simulations of strain controlled cyclic tests at 750 °C have been performed. As was

demonstrated in [77] (chapter 4), the cyclic stress-strain curve stabilizes within the first five cycles. Therefore, only five cycles have been simulated here and the response during the fifth cycle is considered to be representative for the remaining life. The simulated stress-strain loops for the virgin material are shown in Figure 5-9, where the simulated fifth cycle is compared to the tenth cycle in the experiment [137]. This figure illustrates that the simulation matches the experiment quite well. Both the calculated stress levels and the amount of plastic strain (i.e. width of the loop), which plays a major role in the cyclic damage accumulation, are predicted adequately.

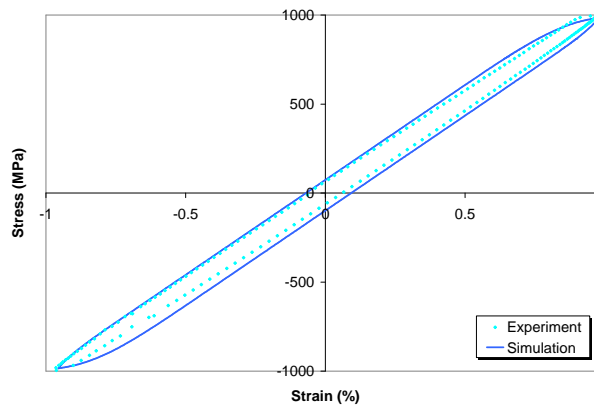


Figure 5-9 Simulated and experimentally determined cyclic test results for virgin material ($h = 60$ nm) at an applied strain range of 1.93%.

In addition to the test on the virgin material, a strain controlled low cycle fatigue (LCF) test on degraded material has been performed [137]. The experimentally determined channel width for the degraded specimen was 266 nm. The proposed degradation model is used to obtain this degraded microstructure, by simulating a creep test at 1050 °C and 68 MPa for 822 hours, which yields the required 266 nm channel width. The degraded microstructure is then used in a LCF test simulation. The result of the simulation (fifth cycle) is shown in Figure 5-10, together with the experimental stress-strain loop (tenth cycle).

Two relevant observations can be obtained from this figure: (i) the amount of plastic deformation, represented by the width of the loop, is remarkably similar in the simulated and experimental curves; (ii) the simulated and experimental loops have shifted to a non-zero mean stress level, but the shifts are in opposite directions. These shifts are caused by the difference between the minimum and maximum values of the applied strain (-0.98% and +0.90% respectively). The present model focused on the response in monotonic loading only (tensile and creep), and does not yet capture this

specific kinematic aspect of the cyclic response. However, the first observation demonstrates that the widening of the stress-strain loop caused by the microstructure degradation is predicted quite well, and particularly this aspect largely determines the cyclic damage accumulation. The effect of the microstructure degradation on the damage accumulation during cyclic tests will be addressed in more detail in the next subsection.

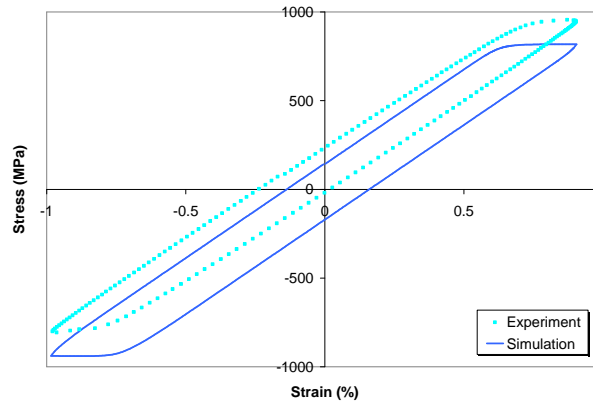


Figure 5-10 Simulated and experimentally determined cyclic test results for degraded material ($h = 266$ nm) at an applied strain range of 1.88%.

5.5.3 Damage accumulation

As was discussed in section 5.4, degradation of the material results in shorter fatigue life times. A method has been proposed to incorporate the effect of degradation into the damage model presented in [77] (chapter 4). This approach is used in the present section to determine the life times for a number of virgin and degraded specimens at different applied strain ranges and temperatures. The parameter set for the virgin material from [77] is used (note that the parameter $\dot{\gamma}_{0, fat}$ has been updated due to an improvement of the constitutive model, see Table 5-1). First, the calculated number of cycles to failure, with no additional damage mechanism for the degraded material included, is plotted versus the experimentally obtained life times in Figure 5-11. The 850 °C and 950 °C data points were already presented in [77], but due to the latest improvement of the constitutive model, also 750 °C tests could be simulated now. Although the life time at the highest applied strain range is overestimated, the remaining 750 °C tests on virgin material are well inside the factor 2 scatter band.

For the tests on the degraded material, however, the life time is seriously overestimated by the original model, which ignores the fact that degradation of the microstructure yields a decrease of the fatigue life time (see section 5.4). As proposed in

5.4.2, the parameter $\dot{\gamma}_{0,fat}$ in the damage model is reduced to $\dot{\gamma}_{0,fat}^*$, as the result of the degradation process. The value of $\dot{\gamma}_{0,fat}^*$ is determined by fitting the 950 °C simulations to the experiments at 950 °C. The results are shown in Figure 5-12, where the data points for the degraded 950 °C specimens are obviously all within the scatter band.

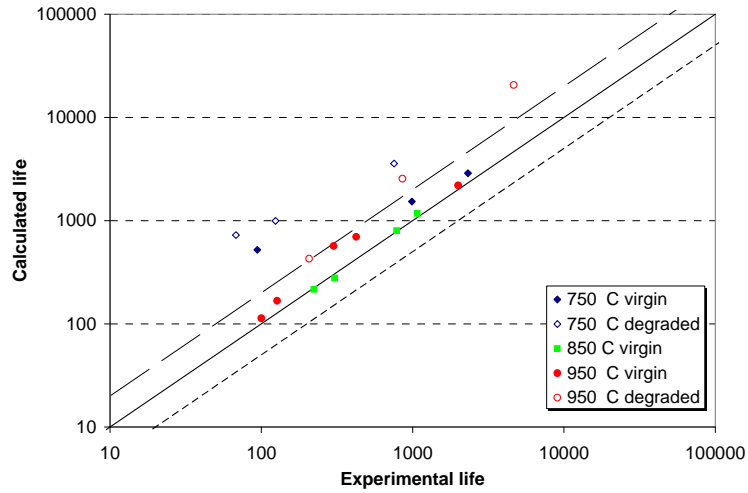


Figure 5-11 Calculated versus experimental fatigue life times using the original damage model [77].

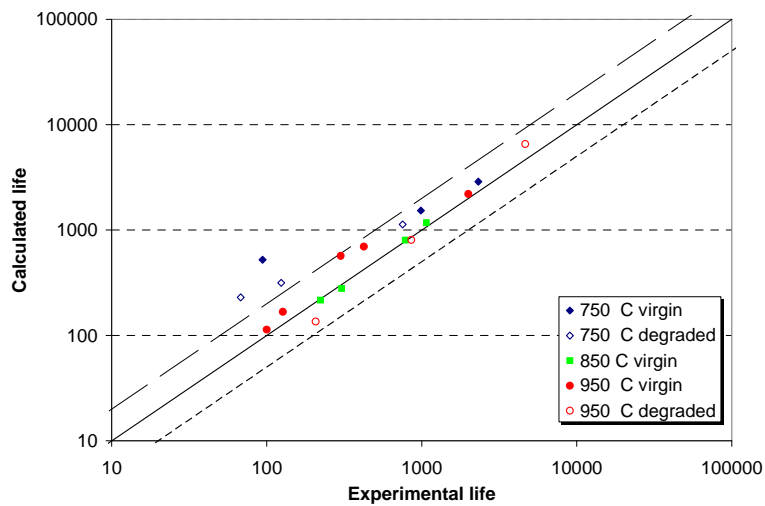


Figure 5-12 Calculated versus experimental life times using the damage model including the degradation mechanism.

Additionally, as a validation of the method, the life times for the degraded 750 °C specimens are calculated, using the value of $\gamma_{0,fat}^*$ as determined from the 950 °C specimens.

Figure 5-12 reveals that, although the 750 °C results on degraded specimens are not all within the scatter band, they show the correct tendency compared to the results for the virgin specimens at this temperature. This illustrates that the proposed model quite adequately simulates the effect of microstructure degradation on the cyclic damage accumulation.

Finally, the practical relevance of the presented model will be discussed. Under normal operating conditions, the microstructure of gas turbine parts quickly degrades. Typically, the hot regions of the components are fully rafted within only a few percent of their total service life time, which means that the structural integrity is largely determined by the mechanical properties of the degraded material. Nevertheless, experiments on virgin material are performed to quantify the mechanical response of the alloy. Moreover, due to the limited duration of tensile tests and low cycle fatigue tests, no significant degradation occurs during these experiments. However, the resulting data is used to assess the life time of the parts in the design process. Obviously, this leads to a discrepancy between the calculated life times and the life times observed in practice. The present model assists in solving this discrepancy, since it enables the quantification of the effects of degradation. The experimental results on the virgin material can be used to calibrate the constitutive model and the method presented in this chapter then enables the incorporation of degradation effects.

5.6 Summary and conclusions

In the present chapter, the kinetics of the microstructure degradation in Ni-base superalloys has been discussed, as well as the effect of this degradation on the material mechanical response and damage accumulation. The following original contributions are thereby achieved:

- a new phenomenological formulation is proposed to describe the kinetics of rafting for a general load condition (not limited to the commonly treated uniaxial stress case);
- a formulation for the coarsening process, acting simultaneously with the rafting process, is incorporated in the kinetics description;
- incorporation of the effect of the microstructure degradation in a recently proposed constitutive framework [62,132];

- incorporation of the effect of the degradation on the damage accumulation during cyclic deformation in a recent damage model for Ni-base superalloys [77].

Although the kinetics of degradation has been studied extensively and the mechanisms are now rather well understood, the amount of published experimental data on the mechanical properties of degraded microstructures is remarkably limited. Moreover, the mechanisms that are responsible for the observed mechanical effects are not fully clear yet. More experimental work in this field will enable the further development of the numerical methods, to which this chapter contributes.

Chapter 6

Application to gas turbine parts

Abstract – *A dedicatedly developed multiscale model for Ni-base superalloys is applied in finite element analyses on a real gas turbine component. Using representative load conditions in terms of temperature and centrifugal forces, the degradation of the microstructure is simulated, revealing a complex distribution of different morphologies in the turbine blade. The mechanical response of the blade, as well as the damage evolution, for a virgin and a degraded material are compared. The model is shown to enable the analysis of real components in a computationally efficient manner, whereby the benefit of including the effect of microstructure degradation is demonstrated.*

6.1 Introduction

The constitutive framework for Ni-base superalloys presented in this thesis has been developed specifically to enable multiscale analyses on real components. This chapter will demonstrate that feature by incorporating the framework in a finite element (FE) model of a gas turbine blade. The model and the analysis procedures are described in section 6.2. The benefits of a model accounting for the effects of microstructure degradation will be demonstrated. Section 6.3 presents the results of the simulated degradation. In section 6.4 creep analyses are performed on both virgin and degraded blades, whereas the damage accumulation is analyzed in section 6.5. Finally, section 6.6 discusses the adopted multiscale approach in comparison with other ways to include degradation effects and forwards some conclusions.

6.2 Finite Element model

The initial FE model for a first stage high pressure turbine blade from an aero engine, taken as the point of departure in this thesis, was created at the National Aerospace Laboratory NLR. The model has been used to predict the loads and life consumption of the blade using a classical macroscopic material descriptions [138]. In the present work, the classical constitutive description is replaced by the developed multiscale model, thus enabling the incorporation of the effects of microstructure degradation.

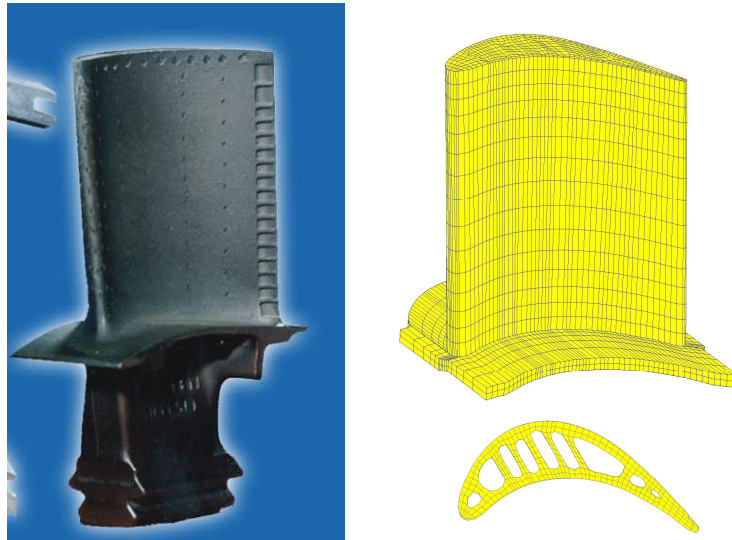


Figure 6-1 High pressure turbine blade and the corresponding finite element mesh. The cross section shows the shape and position of the cooling channels inside the blade.

The turbine blade and the corresponding FE model are shown in Figure 6-1. The blade contains internal cooling channels and a large number of film cooling holes. These holes inject cool air into the boundary layer along the blade surface, thereby creating a cooling film covering the blade airfoil. The internal cooling channels have been modelled geometrically, whereas the film cooling holes are not incorporated in the model due to their small size. Including the holes, which may act as stress concentrations, would require a significant refinement of the FE mesh.

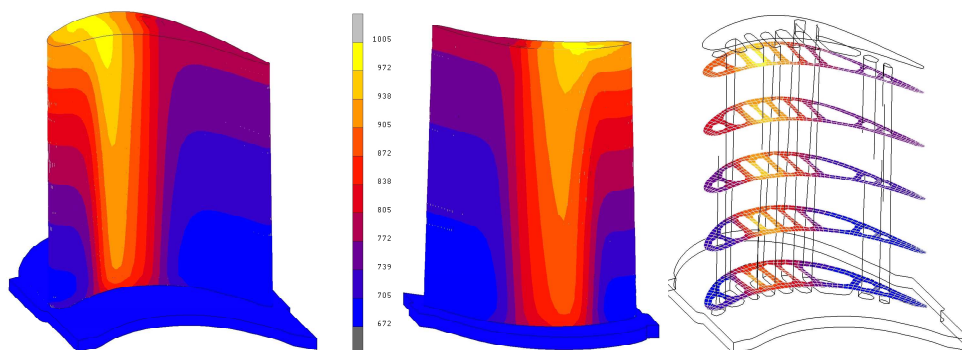


Figure 6-2 Calculated temperature ($^{\circ}\text{C}$) distribution in the turbine blade.

The FE discretization consists of 6201 isoparametric 8-node hexagonal elements and 9150 nodal points. The temperature distribution in the blade, see Figure 6-2, has been determined in a thermal FE analysis, including the effect of film cooling [139]. In this thermal analysis, the temperatures of the primary gas flow and the secondary cooling flow have been specified.

The blade is fixed in space at one of the corners of the blade platform and a centrifugal force corresponding to a rotational speed of 14,000 revolutions per minute (rpm) is applied to the entire geometry. The resulting distribution of the Von Mises equivalent stress at the start of the analysis (no plastic strain yet) is shown in Figure 6-3.

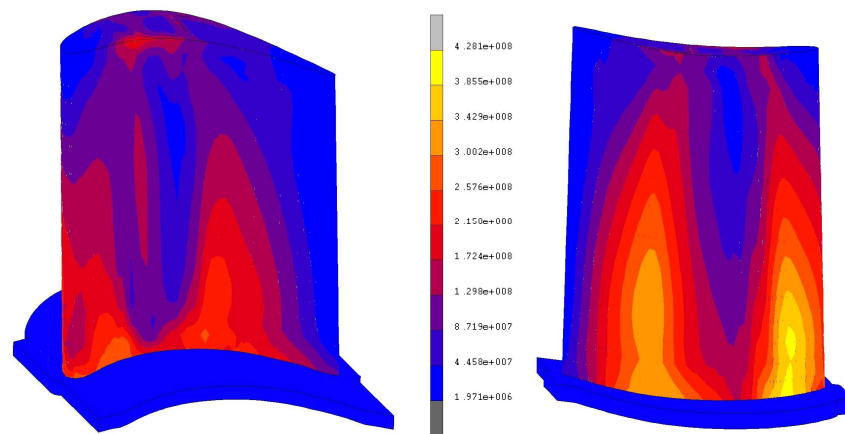


Figure 6-3 Von Mises equivalent stress (Pa) distribution in the turbine blade.

For all analyses in the next sections, the computation times will be mentioned in terms of CPU time. The wall time, which represents the total duration of the analysis, largely depends on the performance of the PC used and is therefore not reported. Due to the large number of internal variables (373 for each integration point, see Appendix A), in combination with the numbers of degrees of freedom in the model, the memory requirements for the analysis are quite demanding.

6.3 Rafting simulation

As a first case study, the microstructure degradation in the turbine blade is simulated. A creep analysis for 1000 hours is performed with the proposed model, using the load conditions as specified in the previous section. To minimize the computational effort,

only the rafting part of the multiscale model is invoked, while the creep strain analysis is omitted. This analysis takes a CPU time of 0.15 hours.

As was described in chapter 5, the kinetics of the microstructure degradation depends on both the temperature and the stress state. Obviously, in a real component, the precise combination of temperature and stress state is different in almost every material point, resulting in a large variety of degraded microstructures over the turbine blade. The whole range of revealed microstructures can be sorted into four classes, as shown in Figure 6-4:

- **non-degraded:** for the material points whose temperature is below the threshold temperature for rafting (828 °C), no degradation has occurred. In these points, the dimensions of the microstructure equal those of the virgin state ($h = 60$ nm, $L = 500$ nm, $\lambda = 560$ nm);
- **partially rafted:** in the material points at moderate temperatures ($T \sim 830$ – 925 °C), the degradation process is rather slow, resulting in partly rafted microstructures after 1000 hours. This means that none of the matrix channels has disappeared completely. Depending on the relative size of the different stress components, one or two channels have widened while the width(s) of the remaining channel(s) is/are reduced. At these conditions, also the coarsening process proceeds slowly, so the typical value of λ ranges from 585 to 610 nm;
- **fully rafted:** the material points at high temperatures ($T > 925$ °C) show a much faster degradation process. As a result, the microstructure is fully rafted and considerably coarsened. Two of the three matrix channels have disappeared and the remaining channel width ranges from 220 nm to even 572 nm at very high temperatures ($T \sim 980$ – 1000 °C). The microstructure periodicity also depends strongly on the temperature, showing values from 750–1450 nm.
- **isotropically coarsened:** the material points experiencing high temperatures, but low stresses, show a more or less isotropic coarsening pattern. This means that the three matrix channels have similar widths, but the microstructure periodicity has increased to values up to 660 nm.

These observations can be compared to the results presented by Epishin et al. [1]. They experimentally examined the microstructure at three different locations in an ex-service CMSX-4 (uncooled) turbine blade. The almost virgin microstructure at the blade platform and the varying orientation of the rafts at the tip region nicely correspond to the results shown in Figure 6-4. The fully rafted microstructure at the blade centre was not observed in the simulation for two reasons: the simulated duration of 1000 hours is much shorter than the 12.700 hours in [1], and the internal blade cooling yields much

lower temperatures in the centre region of the blade, which reduces the degradation rate there.

The results in this section clearly demonstrate that the typical case of a material loaded uniaxially in radial direction, which is mostly supposed as an adequate characterization in literature, is not representative for most of the locations in a real component. That is essentially due to the fact that the present blade is internally cooled, resulting in thermal stresses that cause the stress state to be multiaxial.

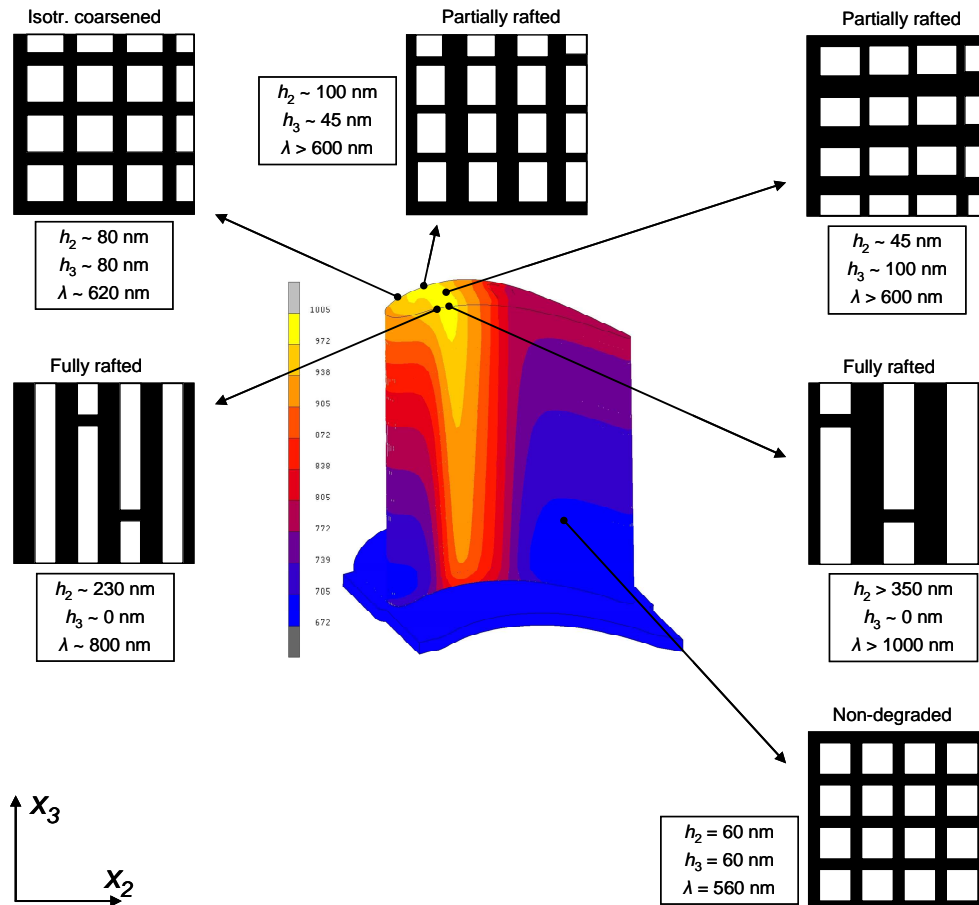


Figure 6-4 Overview of degraded microstructures resulting from a simulation of the degradation process in a turbine blade under service conditions for 1000 hours.

The observation that a large variety of multiaxial stress states occurs in the blade has two important consequences for the incorporation of the degradation in the modelling.

Firstly, only a multiaxial degradation model, like the model developed in chapter 5, is able to correctly simulate the changes in size and shape of the precipitates in the blade. Secondly, the mechanical response of the degraded blade depends on the microstructure morphology in each individual material point. The response of the present blade, with the observed complex variation of the morphology across the component, can only be predicted using a real multiscale approach, as will be discussed in section 6.6.

6.4 Effect of degradation on creep deformation

In this section the effect of the microstructure degradation on the creep deformation in the blade is analyzed. To this purpose, a creep analysis is performed for a period of 100 hours using the load conditions as specified in section 6.2. The analysis results for a blade with a virgin microstructure are then compared to the results of the analysis starting from a degraded microstructure taken from the previous section.

Normally, in the multiscale approach, the unit cell routine is called twice for each integration point in the FE model during each time step. For the present model, this means that the routine would be called almost 100.000 times for each time step, which requires a considerable computational effort. However, in a large number of elements, the stress and/or temperature are not critical at all, i.e. no significant creep strains develop here. To reduce the computational effort, only integration points for which the equivalent stress exceeds a threshold value invoke the unit cell procedure. For all other integration points, the creep strain increment is not resolved and remains zero. The threshold value used for the equivalent stress, σ_{th} , is temperature dependent and defined as:

$$\sigma_{th} = A(1025 - T) \quad (5.23)$$

where T is the integration point temperature in °C and $A = 10^6$ Pa/°C is a constant. This restriction reduces the number of integration points for which the unit cell routine is called by almost 90%. The resulting CPU time for the creep analysis equals 4.81 hours.

The same procedure is used to analyze the creep behaviour for the degraded turbine blade, but in this case the creep analysis is preceded by the degradation analysis as described in the previous section. The total analysis now takes a CPU time of 4.96 hours.

To show the differences in creep response between the virgin and the degraded blade, the creep strain distributions are shown in Figure 6-5 and Figure 6-6, respectively.

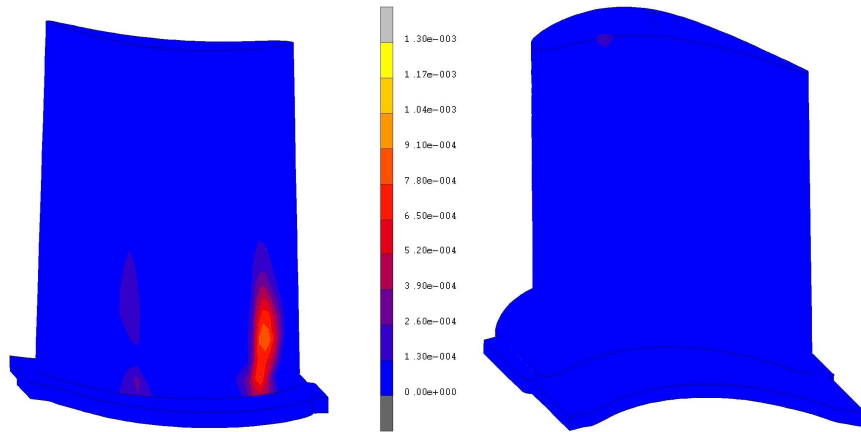


Figure 6-5 Equivalent creep strain distribution in the turbine blade with a virgin microstructure, showing the suction side (left) and pressure side (right) of the blade.

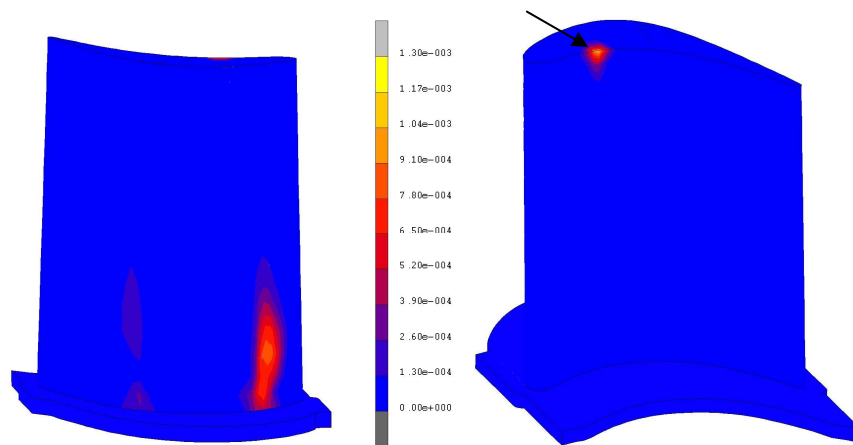


Figure 6-6 Equivalent creep strain distribution in the turbine blade with a degraded microstructure, showing the suction side (left) and pressure side (right) of the blade. The arrow indicates the position of the node, for which the evolution of the creep strain is plotted in Figure 6-7.

These plots illustrate that specifically the high creep strain regions at the suction side of the blade are hardly affected by the degradation. Moreover, the maximum value of the creep strain, located at the inner surface of the blade in one of the cooling channels, has decreased slightly from $1.30 \cdot 10^{-3}$ in the virgin blade to $1.27 \cdot 10^{-3}$ in the degraded blade. However, the equivalent creep strain near the tip at the pressure side is considerably higher in the degraded blade than in the virgin blade. The evolution of the creep strain at this location is plotted in Figure 6-7 for both the virgin and the degraded blade,

showing a significant increase in the creep rate and a corresponding higher creep strain.

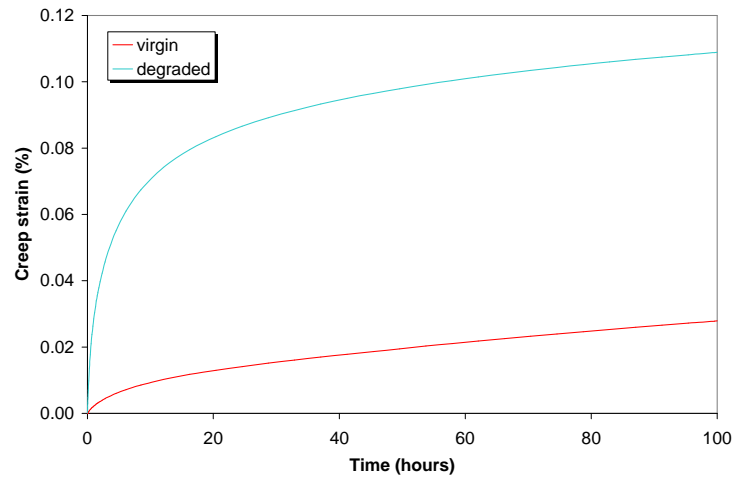


Figure 6-7 Comparison of the equivalent creep strain evolution in a virgin and a degraded blade. The values are plotted for the edge node indicated by the arrow in Figure 6-6.

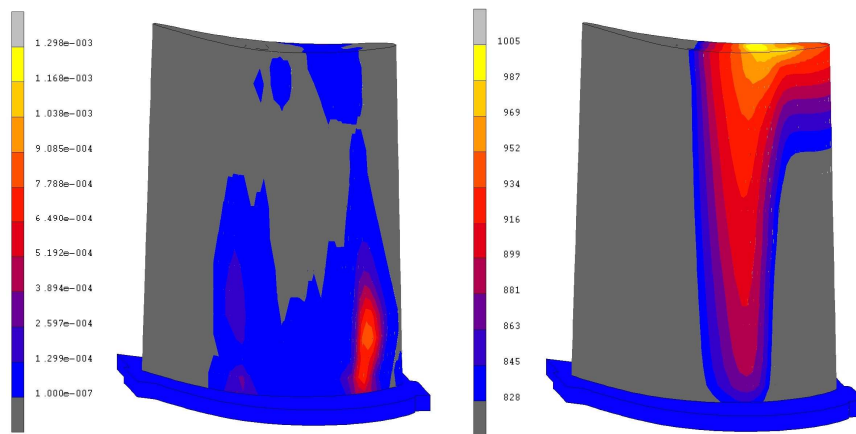


Figure 6-8 Distribution of the creep strain (left) and temperature (right, in °C) in the turbine blade. In the dark grey regions in the temperature plot ($T < 828$ °C) no microstructure degradation occurs.

The rather small degradation in large regions of the blade can be attributed to the fact that the temperature is relatively low in those regions. This is illustrated in Figure 6-8, where the creep strain distribution and the temperature distribution are compared. The grey regions in the temperature plot remain below the threshold temperature ($T = 828$

°C) for microstructure degradation and there relatively high creep strains can typically be observed. On the other hand, the temperature at the blade tip is remarkably high, which means that the degradation is relatively severe in this region. This yields the observed increase in the creep strain rate at the blade tip in Figure 6-7.

The creep life time of a turbine blade is determined by two factors. Firstly, the elongation of the blade during service must be limited to prevent the blade from touching the casing. Secondly, local creep strain values must be limited to prevent the initiation of cracks. The results in this section demonstrate that the effect of degradation on the overall creep deformation is rather limited for this specific component. The blade elongation is therefore hardly affected by the degradation. However, local creep strains, especially in the hot regions of the blade, considerably increase after degradation. Neglecting the effects of rafting and coarsening in the numerical analysis would thus lead to unconservative life predictions. This clearly demonstrates the benefit of the adopted model, which includes the effects of degradation.

6.5 Effect of degradation on the damage accumulation

In this section the effect of the microstructure degradation on the accumulation of cyclic and time-dependent damage is discussed. The turbine blade FE model is used to simulate the behaviour for a transient loading during operation of the gas turbine. The rotational speed is increased from 1.000 rpm to 14.000 rpm and back to 1.000 rpm in a total time period of 200 minutes. The temperature distribution in the blade is not varied in time. Consequently, the thermal stresses are independent and the centrifugal stresses are dependent on time. This simulation characterizes a cycle that represents one flight of an aero-engine. It is performed for both a virgin and a degraded blade and the corresponding CPU times are 0.60 and 0.70 hours, respectively.

Including the damage calculation in the analysis increases the number of state variables per integration point from 295 to 373. In the damage model proposed in chapter 4 the cyclic damage is based on the maximum values of the slip rates and resolved shear stresses during a cycle. This requires the storage of those values during the analysis, which justifies the significant increase in the number of state variables. To limit the analysis times, the multiscale model is invoked only in 40 highly stressed elements (320 integration points) in the blade model, located in the wall between the second and third cooling channel from the leading edge. The use of a fixed stress threshold as the one defined in (5.23) is not appropriate here, since the centrifugal load changes in time.

The calculated total damage values for the virgin and the degraded blade are presented in Figure 6-9. This plot shows that on average the amount of damage in the degraded blade is about 30% larger than in the virgin blade. However, the difference in accumulated damage between the virgin and degraded material varies considerably, and for some points the damage in the degraded blade is even lower than in the virgin blade.

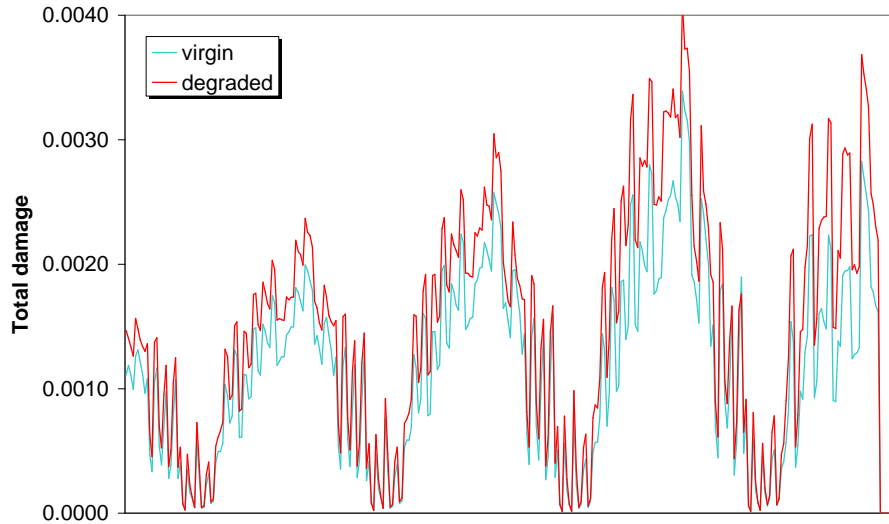


Figure 6-9 Variation of the calculated damage in 320 integration points (40 elements) in the turbine blade FE model. The results for the virgin and degraded blade are compared.

The average amount of damage accumulated during the simulated cycle is $1.5 \cdot 10^{-3}$, which would correspond to a life of 667 of these cycles, provided that each cycle produces the same amount of damage. However, the creep deformation during the initial cycles locally relaxes the high stresses, which yields a decrease of the slip rates and an associated decrease of the damage accumulation. The predicted life will therefore be considerably larger than the rather short life of 667 cycles. For the same reason, the life predictions in chapter 4 have been based on the damage accumulation during the fifth cycle. The faster relaxation of the stress in the degraded material, due to the higher creep strain rates (see Figure 6-7), also explains the observation that for some points the amount of damage in the degraded material is lower than in the virgin material.

Note that in most of the elements in the virgin blade no cyclic damage has accumulated, since the resolved shear stresses do not exceed the Orowan stress. In the

degraded blade, the widening of the matrix channels has decreased the Orowan threshold considerably. Therefore, in the degraded blade, the cyclic damage contributes to the total damage

The results in this section emphasize that including the effects of microstructure degradation in the structural analysis of real components is feasible and desirable, since the damage accumulation in the degraded material may be significantly different from the process in the virgin material.

6.6 Discussion and conclusions

The results in this chapter have demonstrated the added value of incorporating the constitutive framework presented in the previous chapters can be incorporated in engineering finite element analyses on real gas turbine parts in an efficient way. However, validation of the obtained results remains logically difficult, since experimental data on real components is hardly available in the open literature. This problem has been recognized before during other studies on gas turbine components [138,140,141]. As a result, the quantitative reliability of most predictions (e.g. creep strains or fatigue life times) remains questionable, even though the model has been validated on the material point level (see chapters 2 to 5). Nevertheless, the model is certainly well suited to perform sensitivity analyses, in which only relative changes of the results are used instead of absolute values.

This chapter also highlights the benefit of using a multiscale framework in the analysis of real gas turbine components under complex load conditions. To predict the effect of the microstructure degradation on the mechanical response, several approaches can be adopted. Ideally, a multiscale approach is followed, but in some cases also traditional constitutive models only acting on the macroscopic level may be applicable, which are computationally much more efficient. There are three ways to include the effects of degradation in traditional macroscopic constitutive models. The suitability of each approach depends on the complexity of the considered problem:

- **application of a scale factor:** in some cases, the effect of degradation on the mechanical response can be incorporated by the modification of one relevant mechanical property (e.g. yield strength or creep rate). The modification is expressed by a scale factor, which could be derived from experiments. In the numerical analysis, a standard constitutive model can then be used to predict the mechanical response and the effect of degradation is incorporated by scaling the appropriate quantity by the specified factor. This method is obviously computationally efficient, but can only be applied in cases where the degradation is

uniform across the analyzed object, since only one scale factor can be specified for the complete model. Moreover, the loading of the object should also be uniform, since the value of the scale factor normally varies when the load changes. For example, at a higher applied stress, the creep rate will be affected more by the microstructure degradation than at a lower stress.

- **global constitutive relation:** when the loading of the considered object is non-uniform, a constitutive relation is required that describes the effect of degradation. For a specified degree of degradation, the constitutive relation must be able to provide the mechanical response of the material. Since the degree of degradation is still a global parameter, representing the complete object, this method is only applicable for uniformly degraded components only.
- **local constitutive relation:** when the constitutive relation from the previous method is applied at the level of a local integration point level, a non-uniformly degraded component can be analyzed. In that case, the degree of degradation must be specified in each integration point and the constitutive relation should calculate the response on the basis of these defined degrees of degradation.

In the order as presented here, these methods show an increasing complexity and computation time but also a widening application range. The ability of the constitutive relation to describe the effect of degradation largely depends on the complexity of the model. If the degradation is only specified by one parameter representing the 'degree of rafting' (see e.g. [125]), a correlation with the mechanical response can be established rather easily. However, when a more detailed description of the microstructure morphology is required and more parameters are used to describe it (e.g. precipitate size and matrix channel widths in three directions), the derivation of a functional relation between the morphology and the mechanical response is almost impossible. In those situations, a multiscale approach is the only viable option.

Such an approach provides two major advantages: (i) the direct coupling between the macroscopic and microscopic length scales enables the prediction of the mechanical response for any microstructure morphology; (ii) a model describing the temporal evolution of the microstructure in time can rather easily be incorporated, since the microstructure dimensions are already available in the model. This incorporation of the kinetics of degradation enables the simulation of the rafting process and the corresponding effect on the mechanical response.

Finally, from the results in this chapter it can be concluded that:

- the multiscale constitutive framework presented in this thesis can be efficiently applied in FE analyses on real gas turbine components;

-
- for the complex analyses on real components, where the microstructure *and* load conditions vary considerably in time and from point to point across the turbine blade, the presented multiscale approach is the appropriate way to solve the problem.

Chapter 7

Conclusions & recommendations

In the previous chapters, an extensive constitutive framework for Ni-base superalloys has been developed to meet the objective as set in the introduction of this thesis. Elaborating a material model requires, by definition, a simplification of the real material. Consequently, in the present work, several assumptions have been made underpinning the formulations adopted. All separate assumptions and formulations have been motivated thoroughly in the respective sections, however, in general they all satisfy three restrictive requirements. Firstly, the developed model should be computationally efficient, to enable the analysis of real gas turbine components. Secondly, for the same reason, the model should be applicable to a wide range of load conditions. And finally, the formulations in the model should be based on the underlying physical mechanisms. This final criterion ensures that the model not only enables proper simulation of the material behaviour, but also provides more understanding of the experimentally observed material response.

In several cases, the assumptions made in this work are not the only valid choices and alternatives are available. However, based on the three requirements mentioned above, a well motivated compromise has been made.

The multiscale constitutive framework is presented here as a sequence of several modules. In chapter 2, the basic multiscale model is proposed, applying a crystal plasticity approach to the matrix phase and treating the precipitate as an elastic medium. Chapter 3 extends this formulation with a detailed precipitate constitutive model and a matrix cube slip mechanism. In chapter 4 a damage model is proposed and finally chapter 5 treats the degradation of the microstructure and its effect on the mechanical behaviour.

All these aspects are integrated in one framework and a complete set of model parameters has been determined for the widely-used commercial alloy CMSX-4, covering a broad range of load conditions. The model can be applied to other Ni-base superalloys in a straightforward manner, since the modelled mechanisms are generic, however, a material specific parameter set has to be determined.

Due to the modular character of the model, irrelevant mechanisms can be turned off rather easily for a specific application, thereby enhancing the computational efficiency. Also, the required number of model parameters and associated experimental results can be reduced in that way. In the following, the application range of the different modules is described.

The basic implementation with an elastic precipitate phase (Ch. 2) is valid for a material loaded in $\langle 001 \rangle$ direction and for small deformations ($< 5\%$). For orientations other than $\langle 001 \rangle$, the matrix cube slip mechanism (Ch. 3) has to be included, whereas for larger deformations the precipitate deformation mechanisms (Ch. 3) should be used. The simulations on the original microstructure assume that the microstructure does not degrade. This is only the case at lower temperatures (< 900 °C) and limited creep times (depending on the temperature). For higher temperatures and longer times the degradation kinetics (Ch. 5) should be employed or the morphology of the degraded microstructure should be defined manually. In both cases, the mechanisms describing the effect of degradation on the mechanical response (Ch. 5) are activated. Finally, the damage model (Ch. 4) can be used when the creep or fatigue life must be assessed.

Finally, the benefit of the present work for practical applications should be emphasized. In traditional methods, the effects of (changes in) the microstructure morphology on the mechanical behaviour are mostly neglected. However, the results in chapter 5 and 6 clearly demonstrate that these effects are significant, both in terms of deformation and low cycle fatigue life. Therefore, the present model, which is capable of simulating the effects of microstructure degradation, has the potential to improve these analyses considerably.

Moreover, the multiscale character of the model enables the finite element analysis of real components, directly including the effects of microstructure degradation, as is demonstrated in chapter 6. For a component that has degraded uniformly, a standard finite element analysis using a modified plasticity model would be able to perform the analysis. But in real components the degradation is proportional to the non-uniform temperature distribution in the component. These types of problems can only be analyzed using e.g. the proposed multiscale framework.

Although a rather complete constitutive framework has been presented in this thesis, there are still a number of aspects that can be further approved upon. Moreover, several useful extensions of the model are within reach. Therefore, the following recommendations can be made for future research on this subject:

- The set of model parameters presented in this work has been obtained by fitting the simulations to experimental data, as was described in the chapters 2 to 5. To

determine the parameters within acceptable computation times, the different mechanisms in the model are calibrated separately with experiments at conditions that typically activate those mechanisms. For example, the cube slip parameters in chapter 3 are determined from experiments at non- $\langle 001 \rangle$ orientations only. The parameter set may be optimized further by fitting all parameters simultaneously to the complete set of experimental data. This is computationally infeasible using classical optimization techniques (least squares method), but may be possible with more sophisticated methods like neural networks.

- Acquisition of more experimental data could further improve the parameter set or could be used to recognize possibly neglected mechanisms in the model.
- Application of the model to alloys other than CMSX-4 (which initially requires the determination of a new parameter set) might demonstrate the generality of the method and validate the model in a general sense. If the latter would be accomplished, the framework could be applied to perform virtual testing. That would enable the generation of material data for numerous load conditions and degrees of degradation for various alloys, without the need for expensive and time consuming experimental programmes.
- The present model is specifically developed for single crystal materials, which means that for each material point the crystal orientation is fully known. However, for directionally solidified (DS) materials, another technologically important class of turbine materials, this is not the case. DS materials contain elongated grains with identical primary crystal orientations (typically in radial direction), but a randomly varying secondary orientation (in transverse direction). The present model can rather easily be adapted for application to DS materials. By the implementation of an additional length scale in between the macro and meso level, where averaging over several unit cells with different secondary orientations is performed, the behaviour of DS materials can be captured.
- Experimental work by Epishin et al. [1] has shown that the γ/γ' -microstructure is not completely homogeneous, as assumed in this work. During solidification, dendrites develop in the material, causing slight differences in alloy composition between dendritic and interdendritic regions. Apart from small variations in material properties, the dendrite formation also introduces internal stresses in the material, which appear to play a role in the rafting process. Analogous to the previous recommendation, the model could be extended to include these effects by incorporating an additional length scale. In this case only two unit cells are required: one for the dendrites and one for the interdendritic regions.

- The multiscale approach followed in this work enables the analysis of real components. Although a few analyses on a gas turbine blade are shown in chapter 6, validation of these results has not been possible yet, since experimental data for those components is not available. The generation of deformation and degradation data for a real gas turbine component under well-defined load conditions would make this possible.
- The kinetics of rafting and coarsening has been treated in a phenomenological way in chapter 5, since a quantitative description of the process in CMSX-4 was available in literature. This description was based on an extensive experimental programme. However, for a different alloy the same amount of testing must be performed to obtain the degradation characteristics for that material. Moreover, the coarsening model was based on the experimental results at only one specific condition. Therefore, more research should be done on modelling the mechanisms and their driving forces to develop a generally applicable degradation model.

Finally, to conclude this chapter, it can be stated that the present work has been innovative in a number of ways by providing:

- insight in and understanding of the physical mechanisms governing the deformation, damage evolution and microstructure degradation of nickel-base superalloys;
- numerical formulations describing these mechanisms;
- a numerical procedure that combines these mechanisms to describe the mechanical behaviour on the material point level for a wide range of load conditions;
- a computationally efficient material model that can be used in multiscale finite element analyses on real gas turbine components.

Appendix A

Finite Element implementation

A.1 Introduction

The multiscale constitutive framework developed in this thesis has been implemented in the commercial finite element (FE) code *MSC.Marc* [142]. This appendix provides a flow diagram of the multiscale model calculations, showing the consecutive steps followed during a finite element analysis. Further, it describes how the different modules of the model have been implemented in *MSC.Marc* user subroutines and finally the adopted time integration procedure is explained.

A.2 Flow diagram

Figure A-1 shows the flow diagram for solving the multiscale model in time increment $n+1$. The diagram starts with the call from the FE code and proceeds up to the return of the relevant variables back to the FE program. The complete model is defined in a fully explicit way, which means that the increments of all quantities during a time step only depend on the values at the end of the previous time increment. The following steps can be identified in the analysis (the numbers refer to the numbers in Figure A-1):

1. The mesoscopic model is solved to obtain the local stress and strain values for the different unit cell regions (i). This analysis is based on the values of the stress and strain at the end of the previous time increment (denoted n), as provided by the FE code.
2. The misfit stress is calculated from the incompatibility between the regions, quantified by the initial lattice misfit and the present amount of plastic deformation in the different regions.

The steps 3 – 9 are executed for each unit cell region i :

3. The resolved shear stress is calculated for each slip system (α).
4. The lattice resistance for each slip system is calculated from the SSD and GND densities.

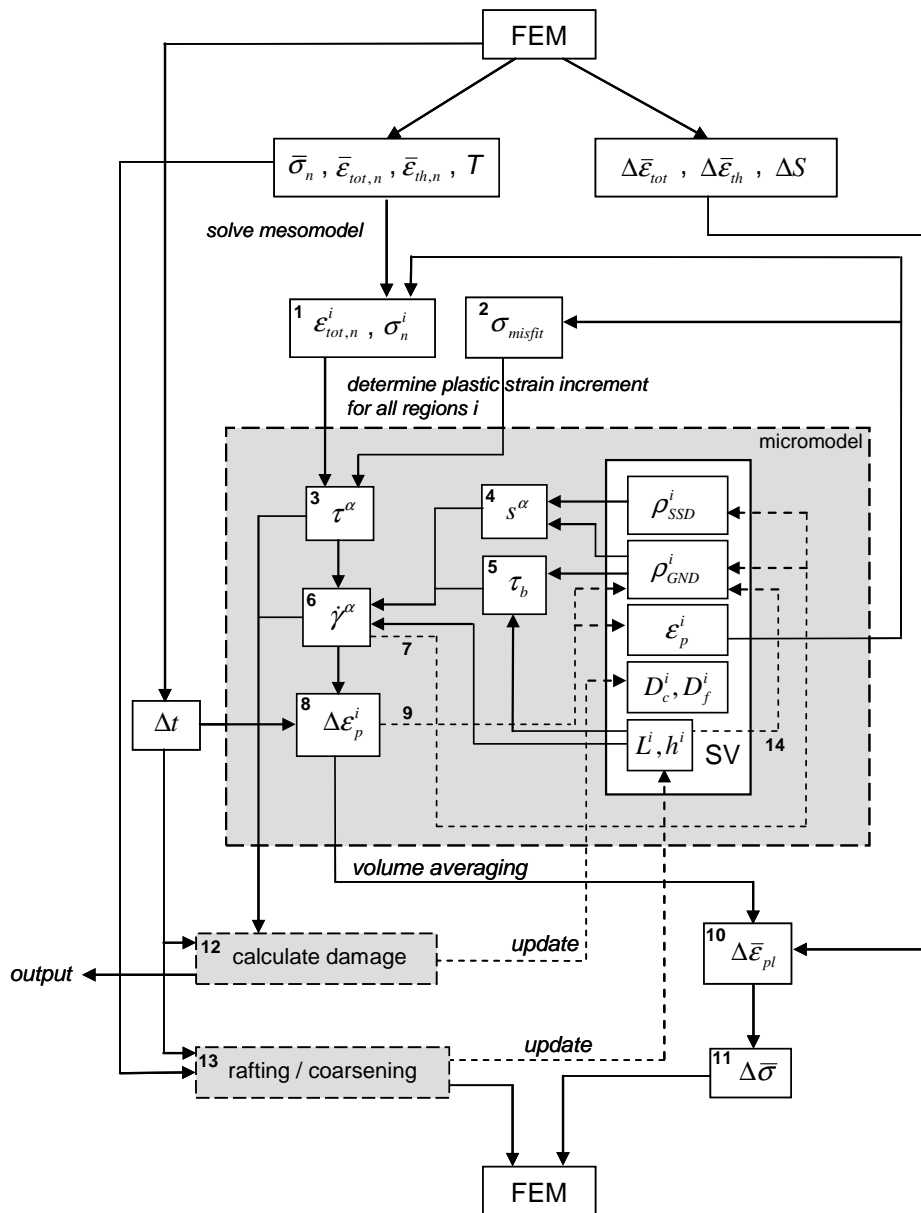


Figure A-1 Flow diagram for solving the multiscale model at time increment $n+1$, starting with the input from the FE code and ending with the return of relevant variables to the FE code. The subscripts n and i refer to the previous time increment and unit cell regions, respectively. The large white block inside the micromodel, denoted by SV, represents the storage of the different state variables.

5. The back stress tensor is calculated from the GND densities (*only for the interface regions*).
6. The slip rate is calculated for each slip system by applying either the matrix or precipitate crystal plasticity model. The slip resistance, back stress and matrix channel width (Orowan stress) are used as input.
7. The SSD densities are updated, using the calculated slip rates.
8. The plastic strain increment for each region is calculated by summation of the slip system slip rates.
9. The stored value of the plastic strain is updated and the GND densities are updated using the strain gradients between the regions (*only for the interface regions*).

The steps 10 – 14 are executed after finishing the loop over all unit cell regions:

10. The mesoscopic plastic strain increment is calculated by volume averaging of the contributions from all regions.
11. The mesoscopic stress increment is calculated from the mesoscopic total and thermal strain increments (provided by the FE code) and the calculated mesoscopic plastic strain increment, as will be explained in section A.4.
12. The cyclic and time-dependent damage increments are calculated from the values of the resolved shear stress and the slip rates. The damage state variables are updated. Since the damage calculation is only a post-processing task, no values are returned to the FE code.
13. The degradation of the microstructure is calculated from the macroscopic (equivalent) stress and temperature values. The microstructure dimensions, that are stored as state variables, are updated.
14. The GND densities are modified according to the changes in microstructural dimensions.

A.3 Multiscale model implementation in MSC.Marc

The multiscale model has been implemented in the user-subroutine *uscvpl*, which can be used within *MSC.Marc* as a user-defined viscoplastic material model. During one time increment in the analysis, this routine is called twice for every integration point, as will be explained in section A.4. The different modules of the model have been coded in 10 separate FORTRAN routines and all model parameters and constants have been collected in another file. The complete model therefore consists of the following routines:

- macro.f: *uscvpl* routine that is called by *MSC.Marc*, acting as the main routine;

- meso.f: defines the set of 120 equations that is solved numerically by the NAG routine to obtain the stresses (60 values) and strains (60 values) in the 10 unit cell regions;
- micro.f: contains the constitutive model, calls the crystal plasticity routines for the two phases (matrix and precipitate);
- crys_plas.f: contains the crystal plasticity model for the matrix phase;
- crys_plas_gp.f: contains the crystal plasticity model for the precipitate phase;
- int_stresses.f: calculates the internal stresses: back stress and misfit stress;
- rafting.f: calculates the evolution of the microstructural dimensions h and L ;
- corr_disloc.f: determines the changes of the GND densities due to changes in microstructure morphology;
- calc_dam.f: calculates the cyclic and time dependent damage accumulation;
- rss.f: function that calculates the resolved shear stress for a given applied stress and slip system;
- constants.f: contains all the model parameters and other constants.

Running an *MSC.Marc* analysis with this model requires one subroutine file, containing a routine called *uvscpl()*. This routine is implemented in *macro.f*, which calls all other routines. To integrate all 11 routines described above in one file, an include file is used with the following content:

```

c -----
c  MSC.Marc user subroutine to apply multiscale model
c -----
      include 'D:\FEMtools\matmodels\macro.f'
      include 'D:\FEMtools\matmodels\meso.f'
      include 'D:\FEMtools\matmodels\micro.f'
      include 'D:\FEMtools\matmodels\crys_plas.f'
      include 'D:\FEMtools\matmodels\crys_plas_gp.f'
      include 'D:\FEMtools\matmodels\rss.f'
      include 'D:\FEMtools\matmodels\int_stress.f'
      include 'D:\FEMtools\matmodels\calc_dam.f'
      include 'D:\FEMtools\matmodels\rafting.f'
      include 'D:\FEMtools\matmodels\corr_disloc.f'

```

Finally, the *MSC.Marc* input deck (.dat file) should contain a number of specific cards to activate the use of the model in the subroutine. These cards are described next.

Parameter section

STATE VARS 373

This specifies that 373 state variables are used in the model (if all modules are active). The state variables are stored for each integration point and keep their value in between separate calls to the subroutine.

CREEP, 0, 0, 1, 1,

This induces the viscoplastic material model to be used

Model definition section

ORTHOTROPIC

I

\$Orthotropic from material named "CMSX-4"

I, **VISCO PLAS**

127.7E+09, 127.7E+09, 127.7E+09, 0.4000000, 0.4000000, 0.4000000, 4000.

123.7E+09, 123.7E+09, 123.7E+09, 1.00E+20, 1.00E+20,

I TO 4700

The VISCO PLAS option should be used in the ISOTROPIC or ORTHOTROPIC card, to specify that the viscoplastic material model should be used, as defined in the *uvscpl* subroutine.

A.4 Solution procedures for non-linear systems

MSC.Marc is an implicit FE code, so the standard procedure to solve a non-linear system of equations is the Newton-Raphson method. This method requires a tangent stiffness to do a prediction for the incremental displacements (strains) at a given force (stress) increment. However, the developed multiscale model is fully explicit, which means that no iterations are required to solve the system, but only limited time steps can be taken. This subsection will describe how the implicit FE code is used to solve the explicit model.

The multiscale model is implemented in the user subroutine *uvscpl*, which is called twice during each iteration. The first time is during *stiffness formation* (LOVL = 4), where the proper stiffness must be supplied by the subroutine. Using this stiffness, the incremental displacements are determined and then the subroutine is called for the second time during *residual calculation* (LOVL = 6) to check the convergence (see next

subsection). By default, the elastic stiffness matrix is used in *uvscpl* and *MSC.Marc* then calculates the tangent stiffness in the following way. At $LOVL = 4$, during the first iteration, the total strain increment is still unknown and is therefore set to zero by *MSC.Marc*. Given the values of stress, strain and temperature at the beginning of the increment, the inelastic deformation in the multiscale model can be calculated, resulting in a mesoscopic plastic strain increment. Then, using $\Delta \bar{\epsilon}_{tot} = 0$ and $\Delta \bar{\epsilon}_{th} = 0$ and the elastic stiffness tensor \mathbf{B} in the following equation

$$\Delta \bar{\sigma} = \mathbf{B} \left(\Delta \bar{\epsilon}_{tot} - \Delta \bar{\epsilon}_{pl} - \Delta \bar{\epsilon}_{th} \right) \quad (\text{A.1})$$

yields a (artificial) mesoscopic stress increment tensor

$$\Delta \bar{\sigma} = \mathbf{B} \left(-\Delta \bar{\epsilon}_{pl} \right) \quad (\text{A.2})$$

Based on this tensor, *MSC.Marc* determines the tangent stiffness and calculates the incremental displacements and actual total strain increment. In the second call to *uvscpl* the residuals are calculated and convergence is checked.

For a fully explicit formulation of the plasticity model, as is the case for the present multiscale model, the calculated plastic strain increment is equal for $LOVL = 4$ and $LOVL = 6$. This is because the calculation of plastic strain is fully based on the stress values at the start of the increment, which do not change anymore during the increment. Therefore, the tangent stiffness calculated after $LOVL = 4$ yields the required displacements directly, which means that immediately a converged solution is obtained at $LOVL = 6$, and no additional iterations are required.

For an implicit formulation this would be different, because the calculated plastic strain increments at $LOVL = 4$ and $LOVL = 6$ are not equal. In that case several iterations would be required to obtain a converged solution.

A.4.1 Convergence control

The default convergence criterion is the ratio of the maximum residual load and the maximum reaction force. If this ratio is below the defined tolerance, the solution has converged; otherwise an additional iteration is required. For the present explicit formulation, convergence is obtained within the first iteration and the convergence criterion has no relevance.

A.4.2 Time step control

During a transient analysis, the time step can be controlled automatically by *MSC.Marc*. A total transient time and a suggested initial time step are supplied by the user and

MSC.Marc then selects the largest time step that satisfies the tolerance set on stress and strain increments. The algorithm is as follows.

For a given time step a solution is obtained and *MSC.Marc* then finds the largest values of stress change per stress, $\frac{\Delta\sigma}{\sigma}$, and plastic strain change per elastic strain, $\frac{\Delta\varepsilon_p}{\varepsilon_d}$. These values are compared to the respective tolerances T_s and T_e and the value p is calculated as the larger of $\frac{\Delta\sigma}{\sigma} / T_s$ and $\frac{\Delta\varepsilon_p}{\varepsilon_d} / T_e$. Depending on the value of p , the program resets the time step according to

- $p > 1$ $\Delta t_{\text{new}} = 0.8 \Delta t_{\text{old}}$
- $0.80 < p < 1$ $\Delta t_{\text{new}} = \Delta t_{\text{old}}$
- $0.65 < p < 0.80$ $\Delta t_{\text{new}} = 1.25 \Delta t_{\text{old}}$
- $p < 0.65$ $\Delta t_{\text{new}} = 1.5 \Delta t_{\text{old}}$

The user specifies the initial value of the time increment (used at the start of the analysis) and may also specify a maximum allowable time step.

Appendix B

Overview of model parameters

B.1 Introduction

The different models developed in this thesis contain a large number of model parameters. These parameters are either quantities with a clear physical meaning, like the lattice parameter δ , or adjustable parameters. For the former set of parameters numerical values are readily obtained, while the latter parameters must be determined by fitting the simulations to experimental results.

The values of the parameters have been defined in the chapter where the specific part of the model is proposed. For example, the constitutive model parameters are all defined in chapter 3. However, the different models are applied again in succeeding chapters, where in some cases the parameter values have been updated to incorporate the most recent model improvements.

To facilitate the reproduction of all presented results, an overview of all parameter values used in the different chapters is provided in this appendix. In Table B-1 the constitutive model parameter values are given. This model is defined in chapter 3 and applied in chapters 4 to 6, so the values are specified for each of these chapters separately. Table B-2 presents the values for the damage model parameters in chapters 4 to 6 and in Table B-3 the degradation model parameters used in chapters 5 and 6 are specified. In these tables, values that deviate from the values as defined in the chapter where the model is presented are printed bold. In Table B-1 the deviations (in the chapter 4 column) originate from a recent model improvement and associated parameter value update. The values used in chapter 3, 5 and 6 are the final values, whereas in chapter 4 the previous values were used. This constitutive model improvement also required an update of the damage model parameters, which explains the deviations in Table B-2.

Finally, the constitutive model with an elastically deforming precipitate is only used in chapter 2, so the parameter values can be obtained directly from that chapter and no additional table is given here.

B.2 Parameter values

Table B-1 Overview of constitutive model parameter values used in the chapters 3 to 6.

Model parameter	Unit	Chapter 3	Chapter 4	Chapter 5	Chapter 6
δ		$-1.1 \cdot 10^{-3}$	$-1.1 \cdot 10^{-3}$	$-1.1 \cdot 10^{-3}$	$-1.1 \cdot 10^{-3}$
λ_{γ}	K ⁻¹	$1.48 \cdot 10^{-5}$	$1.48 \cdot 10^{-5}$	$1.48 \cdot 10^{-5}$	$1.48 \cdot 10^{-5}$
$\lambda_{\gamma'}$	K ⁻¹	$1.32 \cdot 10^{-5}$	$1.32 \cdot 10^{-5}$	$1.32 \cdot 10^{-5}$	$1.32 \cdot 10^{-5}$
$\dot{\gamma}_0$	s ⁻¹	$2.5 \cdot 10^{-11}$	$2.5 \cdot 10^{-11}$	$2.5 \cdot 10^{-11}$	$2.5 \cdot 10^{-11}$
n		2	2	2	2
m		13.8	13.8	13.8	13.8
Q	J	$3.62 \cdot 10^{-20}$	$3.62 \cdot 10^{-20}$	$3.62 \cdot 10^{-20}$	$3.62 \cdot 10^{-20}$
c		0.0415	0.0415	0.0415	0.0415
μ	GPa	100.2	100.2	100.2	100.2
b	nm	0.254	0.254	0.254	0.254
b_1	-	0.98275	0	0.98275	0.98275
b_2	K ⁻¹	$3.636 \cdot 10^{-3}$	0	$3.636 \cdot 10^{-3}$	$3.636 \cdot 10^{-3}$
α		0.85	0.85	0.85	0.85
γ_c	nm	13.5	17.0	13.5	13.5
$\rho_{SSD,0}$	m ⁻²	$1.2 \cdot 10^{14}$	$1.2 \cdot 10^{14}$	$1.2 \cdot 10^{14}$	$1.2 \cdot 10^{14}$
K		3.5	3.5	3.5	3.5
R	nm	20	20	20	20
C_{cs}		2.4	2.4	2.4	2.4
A_{cs}		404	404	404	404
B_{cs}		6.6	6.6	6.6	6.6
τ_{cs}	MPa	122	122	122	122
s_{0,T_p}^{α}	MPa	120	120	120	120
p		4	4	4	4
f_0	Hz	10 ⁴	10 ⁴	10 ⁴	10 ⁴
β		$3.0 \cdot 10^{-3}$	$3.0 \cdot 10^{-3}$	$3.0 \cdot 10^{-3}$	$3.0 \cdot 10^{-3}$
b_{sisf}	nm	0.293	0.293	0.293	0.293
μ_p	GPa	105.2	105.2	105.2	105.2
$\tau_{c,0}$	MPa	330	330	330	330
$T_0 = T_p$	°C	750	750	750	750
a_1	MPa	2.96	2.96	2.96	2.96
a_2		0.0157	0.0157	0.0157	0.0157
A		0.3	0.3	0.3	0.3
B		0.1	0.1	0.1	0.1
κ		0.4	0.4	0.4	0.4
D	J	∞	∞	∞	∞
Q_c^c	kJ mol ⁻¹	85	85	85	85
C	m ² s kg ⁻¹	$3.0 \cdot 10^{-17}$	$8.9 \cdot 10^{-18}$	$3.0 \cdot 10^{-17}$	$3.0 \cdot 10^{-17}$

Table B-2 Overview of damage model parameter values used in the chapters 4 to 6.

Model parameter	Unit	Chapter 4	Chapter 5	Chapter 6
m_{fat}	-	1	1	1
m_c	-	2	2	2
n_{fat}	-	0.4	0.4	0.4
n_c	-	0.3	0.3	0.3
$\dot{\gamma}_{0,fat}$	s ⁻¹	$2.33 \cdot 10^{-2}$	$6.28 \cdot 10^3$	$6.28 \cdot 10^3$
$\dot{\gamma}_{0,c}$	s ⁻¹	$3.11 \cdot 10^5$	$3.11 \cdot 10^5$	$3.11 \cdot 10^5$
Q^c	kJ mol ⁻¹	85	85	85
A_{int}	-	3.5	3.5	3.5

Table B-3 Overview of degradation model parameter values used in the chapters 5 and 6.

Model parameter	Unit	Chapter 5	Chapter 6
A	m s ⁻¹	$2.59 \cdot 10^{-5}$	$2.59 \cdot 10^{-5}$
Q	J mol ⁻¹	221780	221780
L	nm	500	500
U_T	J (mol · MPa · K ⁿ) ⁻¹	0.19	0.19
T_0	K	1100.7	1100.7
n	-	1.294	1.294
C_1	nm ³	$1.25 \cdot 10^8$	$1.25 \cdot 10^8$
f_c	-	0.70	0.70
h_g	nm	161	161
λ_g	nm	560	560
C_{raft}	-	20	20
h_f	nm	107	107
C_β	-	0.39	0.39
$\dot{\gamma}_{0,fat}^*$	s ⁻¹	$2.31 \cdot 10^{-4}$	$2.31 \cdot 10^{-4}$

Bibliography

- [1] Epishin, A., Link, T., Nazmy, M., Staubli, M., Klingelhoffer, H. and Nolze, G.; *Microstructural degradation of CMSX-4: kinetics and effect on mechanical properties*; Superalloys 2008, The Minerals, Metals and Materials Society, Champion, Pennsylvania, USA, 2008.
- [2] Ghosh, R. N., Curtis, R. V. and McLean, M.; *Creep deformation of single crystal superalloys - modelling the crystallographic anisotropy*; Acta Metallurgica et Materialia, 38 (1990), 1977-1992.
- [3] Hanriot, F., Cailletaud, G. and Remy, L.; *Mechanical behaviour of a nickel-base superalloy single crystal*; in High Temperature Constitutive Modeling - Theory and application; ASME, 1991.
- [4] Jordan, E. H., Shi, S. and Walker, K. P.; *The viscoplastic behavior of Hastelloy-X single crystal*; International Journal of Plasticity, 9 (1993), 119-139.
- [5] Yue, Z. F., Lu, Z. Z. and Zheng, C. Q.; *Evaluation of creep damage behavior of nickel-base directionally solidified superalloys with different crystallographic orientations*; Theoretical and Applied Fracture Mechanics, 25 (1996), 127-138.
- [6] Pan, L.-M., Shollock, B. A. and McLean, M.; *Modelling of high-temperature mechanical behaviour of a single crystal superalloy*; Proceedings of the Royal Society London A, 453 (1997), 1689-1715.
- [7] Yue, Z. and Lu, Z.; *Self-consistent constitutive modeling of the creep behaviour of nickel-base directionally solidified superalloys with different grain orientations*; Journal of Material Science and Technology, 14 (1998), 15-19.
- [8] Busso, E. P., O'Dowd, N. P. and Dennis, R. J.; *A rate dependent formulation for void growth in single crystal materials*; Murakami, S. and Ohno, N. (Eds.); 5th IUTAM symposium on creep in structures, Kluwer Academic, Japan, 2000.
- [9] Rist, M. A., Oddy, A. S. and Reed, R. C.; *Three-dimensional simulation of inhomogeneous tertiary creep in single-crystal superalloy test pieces*; Scripta Materialia, 43 (2000), 719-725.
- [10] Daniel, R., Tinga, T. and Henderson, M. B.; *Deformation modelling of the single crystal superalloy CM186LC*; Lecomte-Beckers, J., Carton, M., Schubert, F., and Ennis, P. J. (Eds.); Materials for Advanced Power Engineering, Forschungszentrum Jülich, Jülich, Germany, 2002.
- [11] MacLachlan, D. W., Gunturi, G. S. K. and Knowles, D. M.; *Modelling the uniaxial creep anisotropy of nickel base single crystal superalloys CMSX-4*; Computational Materials Science, 25 (2002), 129-141.
- [12] Cailletaud, G., Chaboche, J. L., Forest, S. and Remy, L.; *On the design of single crystal turbine blades*; La Revue de Metallurgie, 100 (2003), 165-172.
- [13] Eshelby, J. D.; *The determination of the elastic field of an ellipsoidal inclusion, and related problems*; Proceedings of the Royal Society London A, 241 (1957), 376-396.
- [14] Willis, J. R.; *Variational and related methods for the overall properties of composites*; Advances in Applied Mechanics, 21 (1981), 1-78.
- [15] Ponte Castañeda, P. and Suquet, P.; *Nonlinear composites*; Advances in Applied Mechanics, 34 (1998), 171-302.
- [16] Bensoussan, A., Lionis, J. L. and Papanicolaou, G.; *Asymptotic analysis for periodic structures*; North-Holland, Amsterdam, 1978.
- [17] Sanchez-Palencia, E.; *Non-homogeneous media and vibration theory, Lecture notes in physics 127*; Springer, Berlin, 1980.
- [18] Miehe, C., Schröder, J. and Schotte, J.; *Computational homogenization analysis in finite plasticity. Simulation of texture development in polychrystalline materials*; Computer Methods in Applied Mechanics and Engineering, 171 (1999), 387-418.

- [19] Michel, J. C., Moulinec, H. and Suquet, P.; *Effective properties of composite materials with periodic microstructure: a computational approach*; Computer Methods in Applied Mechanics and Engineering, 172 (1999), 109-143.
- [20] Kouznetsova, V. G., Geers, M. G. D. and Brekelmans, W. A. M.; *Multi-scale constitutive modelling of heterogeneous materials with a gradient-enhanced computational homogenization scheme*; International Journal of Numerical Methods in Engineering, 54 (2002), 1235-1260.
- [21] Evers, L. P., Parks, D. M., Brekelmans, W. A. M. and Geers, M. G. D.; *Crystal plasticity model with enhanced hardening by geometrically necessary dislocation accumulation*; Journal of the Mechanics and Physics of Solids, 50 (2002), 2403-2424.
- [22] Fedelich, B.; *A microstructure based constitutive model for the mechanical behavior at high temperatures of nickel-base single crystal superalloys*; Computational Materials Science, 16 (1999), 248-258.
- [23] Fedelich, B.; *A microstructural model for the monotonic and the cyclic mechanical behavior of single crystals of superalloys at high temperatures*; International Journal of Plasticity, 18 (2002), 1-49.
- [24] Busso, E. P., Meissonnier, F. T. and O'Dowd, N. P.; *Gradient-dependent visco-plastic deformation of two-phase single crystals*; Journal of the Mechanics and Physics of Solids, 48 (2000), 2333-2361.
- [25] Meissonnier, F. T., Busso, E. P. and O'Dowd, N. P.; *Finite element implementation of a generalised non-local rate-dependent crystallographic formulation for finite strains*; International Journal of Plasticity, 17 (2001), 601-640.
- [26] Choi, Y. S., Parthasarathy, T. A. and Dimiduk, D. M.; *Numerical study of the flow responses and the geometric constraint effects in Ni-base two-phase single crystals using strain gradient plasticity*; Materials Science and Engineering A, 397 (2005), 69-83.
- [27] Busso, E. P. and McClintock, F. A.; *A dislocation mechanics-based crystallographic model of a B2-type intermetallic alloy*; International Journal of Plasticity, 12 (1996), 1-28.
- [28] Svoboda, J. and Lukas, P.; *Modelling of recovery controlled creep in nickel-base superalloy single crystals*; Acta Materialia, 45 (1997), 125-135.
- [29] Kuttner, T. and Wahi, R. P.; *Modelling of internal stress distribution and deformation behaviour in the precipitation hardened superalloy SC16*; Materials Science and Engineering A, 242 (1998), 259-267.
- [30] Svoboda, J. and Lukas, P.; *Creep deformation modelling of superalloy single crystals*; Acta Materialia, 48 (2000), 2519-2528.
- [31] Hutchinson, J. W.; *Plasticity at the micron scale*; International Journal of Solids and Structures, 37 (2000), 225-238.
- [32] Gurtin, M. E.; *A gradient theory of single-crystal viscoplasticity that accounts for geometrically necessary dislocations*; Journal of the Mechanics and Physics of Solids, 50 (2002), 5-32.
- [33] Cermelli, P. and Gurtin, M. E.; *Geometrically necessary dislocations in viscoplastic single crystals and bicrystals undergoing small deformations*; International Journal of Solids and Structures, 39 (2002), 6281-6309.
- [34] Gurtin, M. E. and Anand, L.; *A theory of strain-gradient plasticity for isotropic, plastically irrotational materials. Part II: Finite deformations*; International Journal of Plasticity, 21 (2005), 2297-2318.
- [35] Gurtin, M. E., Anand, L. and Lele, S. P.; *Gradient single-crystal plasticity with free energy dependent on dislocation densities*; Journal of the Mechanics and Physics of Solids, 55 (2007), 1853-1878.
- [36] Moss, S. J., Webster, G. A. and Fleury, E.; *Creep deformation and crack growth behavior of a single crystal nickel-base superalloy*; Metallurgical and Materials Transactions A, 27A (1996), 829-837.
- [37] Evers, L. P., Brekelmans, W. A. M. and Geers, M. G. D.; *Non-local crystal plasticity model with intrinsic SSD and GND effects*; Journal of the Mechanics and Physics of Solids, 52 (2004), 2379-2401.

- [38] Evers, L. P., Brekelmans, W. A. M. and Geers, M. G. D.; *Scale dependent crystal plasticity framework with dislocation density and grain boundary effects*; International Journal of Solids and Structures, 41 (2004), 5209-5230.
- [39] Pollock, T. M. and Argon, A. S.; *Directional coarsening in nickel-base single crystals with high volume fractions of coherent precipitates*; Acta Metallurgica et Materialia, 42 (1994), 1859-1874.
- [40] Sass, V. and Feller-Kniepmeier, M.; *Orientation dependence of dislocation structures and deformation mechanisms in creep deformed CMSX-4 single crystals*; Materials Science and Engineering A, 245 (1998), 19-28.
- [41] Gunturi, S. S. K., MacLachlan, D. W. and Knowles, D. M.; *Anisotropic creep in CMSX-4 in orientations distant from <001>*; Materials Science and Engineering A, 289 (2000), 289-298.
- [42] Link, T., Epishin, A., Brückner, U. and Portella, P.; *Increase of misfit during creep of superalloys and its correlation with deformation*; Acta Materialia, 48 (2000), 1981-1994.
- [43] Miura, N., Kondo, Y. and Ohi, N.; *The influence of dislocation substructure on creep rate during accelerating creep stage of single crystal nickel-based superalloy CMSX-4*; Pollock, T. M., Kissinger, R. D., and Bowman, R. R. (Eds.); Superalloys 2000, The Minerals, Metals & Materials Society 2000.
- [44] Srinivasan, R., Eggeler, G. and Mills, M. J.; *γ' -cutting as rate-controlling recovery process during high-temperature and low-stress creep of superalloy single crystals*; Acta Materialia, 48 (2000), 4867-4878.
- [45] MacLachlan, D. W., Wright, L. W., Gunturi, G. S. K. and Knowles, D. M.; *Constitutive modelling of anisotropic creep deformation in single crystal blade alloys SRR99 and CMSX-4*; International Journal of Plasticity, 17 (2001), 441-467.
- [46] Rae, C. M. F., Matan, N. and Reed, R. C.; *The role of stacking fault shear in the primary creep of [001]-oriented single crystal superalloys at 750 C and 750 MPa*; Materials Science and Engineering A, 300 (2001), 125-134.
- [47] Chen, Q. Z. and Knowles, D. M.; *Mechanism of <112>/3 slip initiation and anisotropy of γ' phase in CMSX-4 during creep at 750 C and 750 MPa*; Materials Science and Engineering A, 356 (2003), 352-367.
- [48] Prasad, S. C., Rao, I. J. and Rajagopal, K. R.; *A continuum model for the creep of single crystal nickel-base superalloys*; Acta Materialia, 53 (2005), 669-679.
- [49] Dommelen, J. A. W. van, Parks, D. M., Boyce, M. C., Brekelmans, W. A. M. and Baaijens, F. P. T.; *Micromechanical modeling of the elasto-viscoplastic behavior of semi-crystalline polymers*; Journal of the Mechanics and Physics of Solids, 51 (2003), 519-541.
- [50] Ashby, M. F.; *The deformation of plastically non-homogeneous materials*; Philosophical Magazine, 21 (1970), 399-424.
- [51] Kubin, L. P., Canova, G., Condat, M., Devincre, B., Pontikis, V. and Brechet, Y.; *Dislocation microstructures and plastic flow: a 3D simulation*; Solid State Phenomena, 23 & 24 (1992), 455-472.
- [52] Yuan, C., Guo, J. T. and Yang, H. C.; *Deformation mechanism for high temperature creep of a directionally solidified nickel-base superalloy*; Scripta Materialia, 39 (1998), 991-997.
- [53] Busso, E. P., Meissonnier, F. T., O'Dowd, N. P. and Nouaillhas, D.; *Length scale effects on the geometric softening of precipitated single crystals*; Journal de Physique IV France, 8 (1998), 55-61.
- [54] Porter, D. A. and Easterling, K. E.; *Phase transformations in metals and alloys*; Chapman & Hall, London, UK, 1992.
- [55] Bayley, C. J., Brekelmans, W. A. M. and Geers, M. G. D.; *A comparison of dislocation induced back stress formulations in strain gradient crystal plasticity*; International Journal of Solids and Structures, 43 (2006), 7268-7286.
- [56] Lecomte-Beckers, J., Carton, M., Schubert, F. and Ennis, P. J.; *Materials for advanced power engineering 2002*; Forschungszentrum Jülich, Jülich, Germany, 2002.

- [57] Groma, I., Csikor, F. F. and Zaiser, M.; *Spatial correlations and higher-order gradient terms in a continuum description of dislocation dynamics*; Acta Materialia, 51 (2003), 1271-1281.
- [58] Geers, M. G. D., Brekelmans, W. A. M. and Bayley, C. J.; *Second-order crystal plasticity: internal stress effects and cyclic loading*; Modelling and Simulation in Materials Science and Engineering, 15 (2007), S133-S145.
- [59] Roy, A., Peerlings, R. H. J., Geers, M. G. D. and Kasyanyuk, Y.; *Continuum modeling of dislocation interactions: Why discreteness matters ?*; Materials Science and Engineering A, in press (2007), 1-9.
- [60] Duhl, D. N.; *Directionally solidified superalloys*; in Superalloys II: High temperature materials for aerospace and industrial power; Sims, C. T., Stoloff, N. S., and Hagel, W. C.; John Wiley and Sons Ltd, New York, 1987.
- [61] Shenoy, M. M., Gordon, A. P., McDowell, D. L. and Neu, R. W.; *Thermomechanical fatigue behavior of a directionally solidified Ni-base superalloy*; Journal of Engineering Materials and Technology, 127 (2005), 325-336.
- [62] Tinga, T., Brekelmans, W. A. M. and Geers, M. G. D.; *Incorporating strain-gradient effects in a multi-scale constitutive framework for nickel-based superalloys*; Philosophical Magazine, 88 (2008), 3793-3825.
- [63] Méric, L., Poubanne, P. and Cailletaud, G.; *Single crystal modeling for structural calculations: part 1 - model presentation*; Journal of Engineering Materials and Technology, 113 (1991), 162-170.
- [64] Bettge, D. and Österle, W.; *"Cube slip" in near-[111] oriented specimens of a single-crystal nickel-base superalloy*; Scripta Materialia, 40 (1999), 389-395.
- [65] Österle, W., Bettge, D., Fedelich, B. and Klingelhoffner, H.; *Modelling of the orientation and direction dependence of the critical resolved shear stress of nickel-base superalloy single crystals*; Acta Materialia, 48 (2000), 689-700.
- [66] Lall, C., Chin, S. and Pope, D. P.; *The orientation and temperature dependence of the yield stress of Ni₃(Al,Nb) single crystals*; Metallurgical Transactions A, 10A (1979), 1323-1332.
- [67] Qin, Q. and Bassani, J. L.; *Non-Schmid yield behavior in single crystals*; Journal of the Mechanics and Physics of Solids, 40 (1992), 813-833.
- [68] Vitek, V., Pope, D. P. and Bassani, J. L.; *Anomalous yield behaviour of compounds with L₁₂ structure*; in Dislocations in solids. Volume 10: L₁₂ ordered alloys; Nabarro, F. R. N. and Duesbery, M. S.; Elsevier, Amsterdam, 1996.
- [69] Choi, Y. S., Dimiduk, D. M., Uchic, M. D. and Parthasarathy, T. A.; *Modelling plasticity of Ni₃Al-based L₁₂ intermetallic single crystals. I. Anomalous temperature dependence of the flow behaviour*; Philosophical Magazine, 87 (2007), 1939-1965.
- [70] Allan, C. D.; *Plasticity of nickel base single crystal superalloys*; Ph.D.-thesis, Massachusetts Institute of Technology, 1995.
- [71] Westbrook, J. H.; *Superalloys (Ni-base) and dislocations - An introduction*; in Dislocations in solids. Volume 10: L₁₂ ordered alloys; Nabarro, F. R. N. and Duesbery, M. S.; Elsevier, Amsterdam, 1996.
- [72] Brown, L. M. and Ham, R. K.; in Strengthening Methods in Crystals; Kelly, A. and Nicholson, R. B.; Elsevier, Amsterdam, 1971.
- [73] Picu, R. C. and Zhang, D.; *Atomistic study of pipe diffusion in AlMg alloys*; Acta Materialia, 52 (2004), 161-171.
- [74] Reed, R. C., Matan, N., Cox, D. C., Rist, M. A. and Rae, C. M. F.; *Creep of CMSX-4 superalloy single crystals: effects of rafting at high temperature*; Acta Materialia, 47 (1999), 3367-3381.
- [75] Schubert, F., Fleury, G. and Steinhaus, T.; *Modelling of the mechanical behaviour of the single-crystal turbine alloy CMSX-4 during thermomechanical loading*; Modelling and Simulation in Materials Science and Engineering, 8 (2000), 947-957.
- [76] Knowles, D. M. and Gunturi, S. S. K.; *The role of <112>{111} slip in the asymmetric nature of creep of single crystal superalloy CMSX-4*; Materials Science and Engineering A, 328 (2002), 223-237.

- [77] Tinga, T., Brekelmans, W. A. M. and Geers, M. G. D.; *Time-incremental creep-fatigue damage rule for single crystal Ni-base superalloys*; Materials Science and Engineering A, available online (2009), 1-9.
- [78] Ezz, S. S., Pope, D. P. and Paidar, V.; *The tension/compression flow stress asymmetry in Ni₃(Al,Nb) single crystals*; Acta Materialia, 30 (1982), 921-926.
- [79] Choi, Y. S., Parthasarathy, T. A., Dimiduk, D. M. and Uchic, M. D.; *Microstructural effects in modeling the flow behavior of single-crystal superalloys*; Metallurgical and Materials Transactions A, 37A (2006), 545-550.
- [80] Gallerneau, F. and Chaboche, J. L.; *Fatigue life prediction of single crystals for turbine blade applications*; International Journal of Damage Mechanics, 8 (1999), 404-427.
- [81] Zhao, L. G., O'Dowd, N. P. and Busso, E. P.; *A coupled kinetic-constitutive approach to the study of high temperature crack initiation in single crystal nickel-base superalloys*; Journal of the Mechanics and Physics of Solids, 2006), 288-309.
- [82] Dumoulin, S., Busso, E. P. and O'Dowd, N. P.; *A multiscale approach for coupled phenomena in fcc materials at high temperatures*; Philosophical Magazine, 83 (2003), 3895-1916.
- [83] MacLachlan, D. W. and Knowles, D. M.; *Fatigue behaviour and lifing of two single crystal superalloys*; Fatigue and Fracture in Engineering Materials and Structures, 24 (2001), 503-521.
- [84] Lecomte-Beckers, J., Schubert, F., and Ennis, P. J. (Eds.); *Materials for advanced power engineering 1998*, Forschungszentrum Jülich, Jülich, Germany, 1998.
- [85] Basquin, O. H.; *The exponential law of endurance test*; Proceedings of the ASTM, 10 (1910), 625-630.
- [86] Manson, S. S.; *Behaviour of materials under conditions of thermal stress*; NACA TN-2933; National Advisory Committee for Aeronautics, 1954.
- [87] Coffin, L. F.; *A study of the effects of cyclic thermal stresses on a ductile metal*; Transactions of the ASME, 76 (1954), 931-950.
- [88] Li, S. X. and Smith, D. J.; *High temperature fatigue-creep behaviour of single crystal SRR99 nickel base superalloys: part II - fatigue-creep life behaviour*; Fatigue and Fracture in Engineering Materials and Structures, 18 (1995), 631-643.
- [89] Chen, L., Liu, Y. and Xie, L.; *Power-exponent function model for low cycle fatigue life prediction and its applications - Part II: Life prediction of turbine blades under creep-fatigue interaction*; International Journal of Fatigue, 29 (2007), 10-19.
- [90] Palmgren, A.; *Durability of Ball Bearings*; Zeitschrift des Vereins Deutscher Ingenieure, 68 (1924), 339-341.
- [91] Miner, M. A.; *Cumulative Damage in Fatigue*; Journal of Applied Mechanics, 12 (1954), A159-A164.
- [92] Robinson, E. L.; *Effect of Temperature Variation on the Long-Time Rupture Strength of Steels*; Transactions of the ASME, 74 (1952), 777-781.
- [93] Majumdar, S. and Maiya, P. S.; *A mechanistic model for time-dependent fatigue*; Journal of Engineering Materials and Technology, 102 (1980), 159-167.
- [94] Satoh, M. and Krempl, E.; *An incremental life prediction law for creep-fatigue interaction*; in Material behaviour at elevated temperatures and components analysis; American Society of Mechanical Engineers,
- [95] Arakere, N. K. and Swanson, G.; *Effect of crystal orientation on fatigue failure of single crystal nickel base turbine blade superalloys*; ASME Turbo Expo 2000, Munich, Germany,
- [96] Brown, M. W. and Miller, K. J.; *A theory for fatigue failure under multiaxial stress-strain conditions*; Proceedings of the Institution of Mechanical Engineers, 187 (1973), 745-755.
- [97] Yeh, N. and Krempl, E.; *An incremental life prediction law for multiaxial creep-fatigue interaction and thermomechanical loading*; in Advances in multiaxial fatigue, ASTM STP 1191; McDowell, D. L. and Ellis, R.; American Society for Testing and Materials, Philadelphia,

- [98] Arakere, N. K.; *High-temperature fatigue properties of single crystal superalloys in air and hydrogen*; Journal of Engineering for Gas Turbines and Power, 126 (2004), 590-603.
- [99] Levkovitch, V., Sievert, R. and Svendsen, B.; *Simulation of deformation and lifetime behavior of a fcc single crystal superalloy at high temperature under low-cycle fatigue loading*; International Journal of Fatigue, 28 (2006), 1791-1802.
- [100] Levkovitch, V., Sievert, R. and Svendsen, B.; *Simulation of low cycle fatigue failure of FCC single crystals*; Portella, P. D. (Eds.); Fifth International Conference on Low Cycle Fatigue, Deutscher Verband für Materialforschung und -prüfung e.V., Berlin, 2003.
- [101] Desmorat, R., Kane, A., Seyed, M. and Sermage, J. P.; *Two scale damage model and related numerical issues for thermo-mechanical high cycle fatigue*; European Journal of Mechanics - A/Solids, 26 (2007), 909-935.
- [102] Reed, R. C., Cox, D. C. and Rae, C. M. F.; *Damage accumulation during creep deformation of a single crystal superalloy at 1150 °C*; Materials Science and Engineering A, 448 (2007), 88-96.
- [103] Epishin, A., Link, T., Brückner, U. and Portella, P. D.; *Kinetics of the topological inversion of the γ/γ' -microstructure during creep of a nickel-based superalloy*; Acta Materialia, 49 (2001), 4017-4023.
- [104] Serin, K., Gobenli, G. and Eggeler, G.; *On the influence of stress state, stress level and temperature on γ channel widening in the single crystal superalloy CMSX-4*; Materials Science and Engineering A, 387-389 (2004), 133-137.
- [105] Carry, C. and Strudel, J. L.; *Apparent and effective creep parameters in single crystals of a nickel base superalloy - II. secondary creep*; Acta Metallurgica, 26 (1978), 859-870.
- [106] Shyam, A. and Milligan, W. W.; *A model for slip irreversibility, and its effect on the fatigue crack propagation threshold in a nickel-base superalloy*; Acta Materialia, 53 (2005), 835-844.
- [107] Lukas, P. and Kunz, L.; *Cyclic slip localisation and fatigue crack initiation in fcc single crystals*; Materials Science and Engineering A, 314 (2001), 75-80.
- [108] Lukas, P. and Kunz, L.; *Small cracks - nucleation, growth and implication to fatigue life*; International Journal of Fatigue, 25 (2003), 855-862.
- [109] Lukas, P., Kunz, L. and Svoboda, M.; *High-temperature ultra-high cycle fatigue damage of notched single crystal superalloys at high mean stresses*; International Journal of Fatigue, 27 (2005), 1535-1540.
- [110] Chataigner, E. and Remy, L.; *Thermomechanical fatigue behaviour of coated and bare nickel-base superalloy single crystals*; in Thermomechanical fatigue behaviour of Materials. ASTM STP 1263; Verrilli, M. J. and Castelli, M. G.; American Society for Testing and Materials,
- [111] Westbrooke, E. F., Forero, L. E. and Ebrahimi, F.; *Slip analysis in a Ni-base superalloy*; Acta Materialia, 53 (2005), 2137-2147.
- [112] Kamaraj, M.; *Rafting in single crystal nickel-base superalloys - An overview*; Sadhana, 28 (2003), 115-128.
- [113] Matan, N., Cox, D. C., Rae, C. M. F. and Reed, R. C.; *On the kinetics of rafting in CMSX-4 superalloy single crystals*; Acta Materialia, 47 (1999), 2031-2045.
- [114] Véron, M., Brechet, Y. and Louchet, F.; *Directional coarsening of Ni-based superalloys: computer simulation at the mesoscopic level*; Acta Materialia, 44 (1996), 3633-3641.
- [115] Socrate, S. and Parks, D. M.; *Numerical determination of the elastic driving force for directional coarsening in Ni-superalloys*; Acta Metallurgica et Materialia, 41 (1993), 2185-2209.
- [116] Keller, R. R., Maier, H. J. and Mughrabi, H.; *Characterization of interfacial dislocation networks in a creep-deformed nickel-base superalloy*; Scripta Metallurgica et Materialia, 28 (1993), 23-28.
- [117] Sugui, T., Zhang, J., Zhou, H. and Yang, H.; *Aspects of primary creep of a single crystal nickel-base superalloy*; Materials Science and Engineering A, 262 (1999), 271-278.
- [118] Svoboda, J. and Lukas, P.; *Modelling of kinetics of directional coarsening in Ni-superalloys*; Acta Materialia, 44 (1996), 2557-2565.

- [119] Henderson, P., Berglin, L. and Jansson, C.; *On rafting in a single crystal nickel-base superalloy after high and low temperature creep*; Scripta Materialia, 40 (1999), 229-234.
- [120] Véron, M., Brechet, Y. and Louchet, F.; *Strain induced directional coarsening in Ni based superalloys*; Scripta Materialia, 34 (1996), 1883-1886.
- [121] Kamaraj, M., Serin, K., Kolbe, M. and Eggeler, G.; *Influence of stress state on the kinetics of γ channel widening during high temperature and low stress creep of the single crystal superalloy CMSX-4*; Materials Science and Engineering A, 319 (2001), 796-799.
- [122] Epishin, A., Link, T., Klingelhoffer, H., Fedelich, B., Brückner, U. and Portella, P. D.; *New technique for characterization of microstructural degradation under creep: application to the nickel-base superalloy CMSX-4*; Creep 2008, Bayreuth, Germany, 2008.
- [123] Buffiere, J. Y. and Ignat, M.; *A dislocation based criterion for the raft formation in nickel-based superalloys single crystals*; Acta Metallurgica et Materialia, 43 (1995), 1791-1797.
- [124] Nabarro, F. R. N., Cress, C. M. and Kotschy, P.; *The thermodynamic driving force for rafting in superalloys*; Acta Materialia, 44 (1996), 3189-3198.
- [125] Fedelich, B., Künecke, G., Epishin, A., Link, T. and Portella, P. D.; *Constitutive modelling of creep degradation due to rafting in single crystal Ni-base superalloys*; Creep 2008, Bayreuth, Germany, 2008.
- [126] Ratel, N., Bruno, G., Bastie, P. and Mori, T.; *Plastic strain induced rafting of γ precipitates in Ni superalloys: Elasticity analysis*; Acta Materialia, 54 (2006), 5087-5093.
- [127] Svoboda, J. and Lukas, P.; *Model of creep in <001>-oriented superalloy single crystals*; Acta Materialia, 46 (1998), 3421-3431.
- [128] Shui, L., Tao, J., Sugui, T. and Zhuangqi, H.; *Influence of precipitate morphology on tensile creep of a single crystal nickel-base superalloy*; Materials Science and Engineering A, 454-455 (2007), 461-466.
- [129] Shui, L., Tian, S. and Hu, Z. Q.; *Influence of pre-compression on microstructure and creep characteristic of a single crystal nickel-base superalloy*; Materials Science and Engineering A, 418 (2006), 229-235.
- [130] Ott, M. and Mughrabi, H.; *Dependence of the high-temperature low-cycle fatigue behaviour of the monocrystalline nickel-base superalloys CMSX-4 and CMSX-6 on the γ/γ' -morphology*; Materials Science and Engineering A, 272 (1999), 24-30.
- [131] Zhou, H., Ro, Y., Harada, H. and Aoki, Y.; *Deformation microstructures after low-cycle fatigue in a fourth-generation Ni-base SC superalloy TMS-138*; Materials Science and Engineering A, 381 (2004), 20-27.
- [132] Tinga, T., Brekelmans, W. A. M. and Geers, M. G. D.; *Cube slip and non-Schmid effects in single crystal nickel-base superalloys*; Modelling and Simulation in Materials Science and Engineering, submitted (2009), 1-30.
- [133] Fedelich, B., Epishin, A., Nazmy, M., Tinga, T., Lapin, J. and Künecke, G.; *Case study: degradation of SX alloy*; Final Report WP 5; COST 538, Berlin, Germany, 2008.
- [134] Jinjiang, Y., Xiaofeng, S., Nairen, Z., Tao, J., Hengrong, G. and Zhuangqi, H.; *Effect of heat treatment on microstructure and stress rupture life of DD32 single crystal Ni-base superalloy*; Materials Science and Engineering A, 460-461 (2007), 420-427.
- [135] Ai, S. H., Lupinc, V. and Onofrio, G.; *Influence of precipitate morphology on high temperature fatigue crack growth of a single crystal nickel base superalloy*; Scripta Metallurgica et Materialia, 29 (1993), 1385-1390.
- [136] Fedelich, B. and Künecke, G.; *COST 538 program; Final report work package 4: Microstructural Modelling*; Bundesanstalt für Materialforschung und -prüfung, Berlin, Germany, 2008.
- [137] Nazmy, M., Staubli, M. and Kuenzler, A.; *Evaluation of microstructural and properties changes of Ni-base superalloys after high temperature creep loading and its rejuvenation*; COST 538 final report; Alstom Ltd., Baden, Switzerland, 2008.
- [138] Tinga, T., De Wolf, W. B., Visser, W. P. J. and Woldendorp, S.; *Integrated lifing analysis of a film-cooled turbine blade*; RTO-AVT Symposium on Monitoring and Management of Gas

- Turbine Fleets for Extended Life and Reduced Costs, NATO Research and Technology Organisation, Manchester, UK, 2001.
- [139] De Wolf, W. B., Woldendorp, S. and Tinga, T.; *Analysis of combined convective and film cooling on an existing turbine blade*; RTO-AVT Symposium Heat Transfer and Cooling in Propulsion and Power Systems, NATO Research and Technology Organisation, Loen, Norway, 2001.
- [140] Tinga, T., Kampen, J. F. van, Jager, B. de and Kok, J. B. W.; *Gas turbine combustor liner life assessment using a combined fluid / structural approach*; Journal of Engineering for Gas Turbines and Power, 129 (2007), 69-79.
- [141] Tinga, T., Visser, W. P. J., De Wolf, W. B. and Broomhead, M.; *Integrated life analysis tool for gas turbine components*; International Gas Turbine & Aeroengine Congress, ASME paper 2000-GT-646, Munich, Germany, 2000.
- [142] *MSC.Marc version 2005 r2*; MSC.Software Corporation, Santa Ana, California, USA, 2004.

Samenvatting

Gasturbines worden op grote schaal gebruikt voor het opwekken van elektriciteit en de voortstuwing van vliegtuigen en schepen. De zwaarst belaste onderdelen in deze motoren, de turbine rotor bladen, worden gemaakt van éénkristallijne nikkel superlegeringen. Het superieure hoge temperatuur gedrag van deze materialen wordt toegeschreven aan de speciale microstructuur, bestaande uit twee fasen: een γ -matrix (Ni) met daarin een grote volume fractie γ' -deeltjes (Ni_3Al). Tijdens het gebruik van de gasturbine veranderen de oorspronkelijk kubische precipitaten in het materiaal via een diffusieproces in langgerekte platen. Dit degradatieproces wordt 'rafting' genoemd.

In dit onderzoek is een micromechanisch materiaalmodel ontwikkeld dat specifiek rekening houdt met de morfologie van de microstructuur en de veranderingen die daarin optreden. Daarbij wordt het materiaal op meerdere niveaus of lengteschalen gemodelleerd, een zogenaamde multiscale aanpak. Op de macroscopische schaal wordt het engineering niveau beschreven waarop een eindige elementen berekening wordt uitgevoerd. De mesoscopische schaal representeert de microstructuur in een macroscopisch materiaalpunt. Op dit niveau wordt het materiaal beschouwd als een mengsel van twee verschillende fasen, die samen een hier specifiek voor dit materiaal ontwikkelde eenheidscel vormen. De microscopische schaal bevindt zich op het niveau van het kristalrooster van de individuele fasen. Op dit niveau wordt het materiaalgedrag van de twee fasen beschreven.

De gepresenteerde eenheidscel bevat speciale grensvlak regio's, die de gradiënten in plastische rek herbergen. In deze grensvlakregio's ontwikkelen zich interne spanningen, enerzijds onder invloed van de rekgradiënten en anderzijds ten gevolge van de kleine afwijking in roosterafstand tussen beide fasen. De beperkte omvang van de eenheidscel en de micromechanische vereenvoudigingen zorgen er voor dat het model vooral in een multiscale aanpak efficiënt werkt. De respons van de eenheidscel wordt in een eindige elementen analyse op het niveau van een materiaalpunt numeriek opgelost. Deze aanpak is qua rekentijd veel efficiënter dan een eenheidscel die met behulp van eindige elementen in detail is gediscrètiseerd.

Het gedrag van de matrix fase wordt gesimuleerd met een kristal-plasticiteitsmodel dat rekgradiënten in rekening brengt. In dit model beïnvloeden niet-uniform verdeelde geometrisch noodzakelijke dislocaties (GNDs), die het gevolg zijn van rekgradiënten in de grensvlakregio's, het verstevigingsgedrag van het materiaal. Verder is in de verstevigingswet speciaal voor dit twee-fasen materiaal een drempelterm

toegevoegd die gerelateerd is aan de Orowan spanning. Voor de precipitaatfase zijn de dislocatiemechanismen die het doorsnijden en het omklimmen van de precipitaten beschrijven in het model meegenomen. Bovendien zijn het typische anomale vloeigedrag van Ni₃Al-intermetallische verbindingen en andere non-Schmid effecten geïmplementeerd en wordt hun effect op het mechanisch gedrag van de superlegering gedemonstreerd.

Vervolgens wordt er een schademodel gepresenteerd dat tijdsafhankelijke en cyclische schade integreert in één schaderegel. Er wordt een criterium op basis van de Orowan spanning geïntroduceerd om het omkeren van de sliprichting op microniveau te detecteren. De cyclische schadeopbouw wordt vervolgens gekwantificeerd met behulp van het dislocatie immobilisatie mechanisme. Verder wordt de interactie tussen tijdsafhankelijke en cyclische schadeopbouw in het model meegenomen. Simulaties voor een groot aantal belastingscondities laten vervolgens zien dat de resultaten goed overeenkomen met experimentele resultaten.

De degradatie van de microstructuur ten gevolge van rafting en vergroving wordt gemodelleerd door het definiëren van evolutievergelijkingen voor een aantal microstructurele afmetingen. Deze vergelijkingen zijn consistent met een reductie van de interne energie, die vaak wordt gezien als de drijvende kracht achter het degradatieproces. De mechanische respons van het gedegradeerde materiaal wordt gesimuleerd en er wordt aangetoond dat er overeenstemming is tussen de simulaties en de trends die in experimenten worden waargenomen.

Tenslotte wordt gedemonstreerd dat het model geschikt is voor multiscale analyses door toepassing van de methode in eindige elementen analyses op een gasturbine blad. Dit toont aan dat veranderingen in de microstructuur het mechanisch gedrag van gasturbine componenten aanzienlijk beïnvloeden.

Dankwoord

Nu dit proefschrift gereed is, wordt het tijd om wat mensen te bedanken voor hun rol in de totstandkoming ervan. Ten eerste wil ik mijn promotor Marc Geers en co-promotor Marcel Brekelmans hartelijk bedanken voor hun niet aflatende stroom van kritische vragen en nuttige suggesties. Ik ben af en toe met de nodige twijfels naar Eindhoven afgereisd, maar na de inhoudelijke discussies op de TU/e zat ik altijd weer gemotiveerd en vol nieuwe ideeën in de trein terug naar huis.

Daarnaast wil ik het Nationaal Lucht- en Ruimtevaartlaboratorium NLR in het algemeen en Henk-Jan ten Hoeve in het bijzonder bedanken. Zij hebben de mogelijkheid gecreëerd voor het opstarten en uitvoeren van dit onderzoek bij het NLR en constructief meegewerkt aan de formaliteiten die mijn overstap naar de Nederlandse Defensie Academie (NLDA) met zich meebrachten. Ook Douwe Stapersma, mijn sectiehoofd bij de NLDA, wil ik bedanken voor het faciliteren van de afronding van mijn onderzoek.

Verder gaat mijn dank uit naar mijn ex-collega's bij het NLR. Met name met mijn kamergenoot Frank Grooteman heb ik vele discussies gevoerd over het nut van micro-mechanische modellen. Ook Rob Huls heeft me met zijn kritische vragen, vooral tijdens de reizen naar de COST meetings, meerdere malen aan het denken gezet. Hetzelfde geldt voor Henk Kolkman, die als commissielid op (de van hem bekende) grondige wijze mijn proefschrift kritisch heeft doorgenomen. Van mijn huidige collega's bij de NLDA wil ik vooral Theo Popma bedanken voor de ondersteuning op onderwijsgebied gedurende het afgelopen jaar, waardoor ik mij wat meer kon richten op het afronden van dit proefschrift.

Maar verreweg de meeste dank ben ik verschuldigd aan Yvonna en onze kinderen Jasper en Nynke. Yvonna heeft me altijd volledig gesteund en relativerende opmerkingen gemaakt in de periodes waarin het even tegenzat. En de kinderen hebben zonder morren geaccepteerd dat ik regelmatig een avond, weekend of zelfs een hele kerstvakantie achter de computer zat te werken. Dank daarvoor !

Curriculum Vitae

Tiedo Tinga, born on 6th March 1973 in Lemmer

- | | |
|------------------------|----------------------------------------------------------------------------------------------------------------------------------------|
| Sept. 1985 – June 1991 | VWO, CSG Emmeloord |
| Sept. 1991 – Nov. 1995 | MSc Applied Physics, University of Groningen, graduated at Materials Science Department |
| Feb. 1996 – Feb. 1998 | Engineering Design Traineeship (PDEng) at University of Groningen and Delft University of Technology |
| Mar. 1998 – Aug. 2007 | Senior Scientist at the National Aerospace Laboratory NLR (Marknesse) in the field of structural integrity and computational mechanics |
| since Sept. 2007 | Associate Professor in Maintenance Technology, Netherlands Defence Academy NLDA (Den Helder) |